

Graphene Electronics: Device Fabrication and Electronic Transport

Dissertation

zur Erlangung des akademischen Grades
Doktor der Naturwissenschaften
(Dr. rer. nat.)

der Technischen Fakultät
der Christian-Albrechts-Universität zu Kiel

vorgelegt von

M. Sc.

Shu Xu

aus China

Stuttgart & Kiel 2012

- | | |
|--------------|------------------------------|
| 1. Gutachter | Prof. Dr. Klaus von Klitzing |
| 2. Gutachter | Prof. Dr. Franz Faupel |
| 3. Gutachter | Prof. Dr. Helmut Föll |
| 4. Gutachter | Prof. Dr. Michael Bauer |

Datum der mündlichen Prüfung 17.01.2012

Graphene Electronics: Device Fabrication and Electronic Transport

Shu Xu

Abstract

Graphene, the novel two-dimensional system that is composed of one-atom-thick carbon honeycombs, has emerged in the past few years as a promising material for both fundamental research and applications. In this dissertation, we develop reliably working fabrication techniques for high-electronic-quality single- and dual-gated graphene devices. We investigate various electronic transport phenomena in graphene field-effect-transistors and bipolar junctions by means of multi-terminal measurements, and explore graphene's potential applications in the fields of quantum resistance metrology and Landau emitters.

Through careful substrate-cleaning/lift-off, a high Drude mobility (e.g. >10000 cm^2/Vs at a carrier density of $4 \times 10^{12} \text{ cm}^{-2}$ at room temperature) can be achieved in our field effect devices, where graphene sheets are supported by oxidized Si wafers. The charge neutrality point can be shifted close to 0 V by an *in situ* vacuum annealing. A self-consistent Boltzmann formalism within the random phase approximation is found to give an adequate description to the zero-field diffusive transport in our devices.

A quantum Hall state at filling factor $\nu = 0$ is observed in high-quality samples under very low excitation currents. Owing to the large energy spacing (~ 149 meV in a magnetic field $B = 14$ T) between the zeroth and first Landau levels, a large critical current (~ 11 A/m) associated with the breakdown of the $\nu = 2$ quantum Hall state is measured in our graphene sample at a temperature of 10 K and $B = 14$ T. We also report our preliminary

attempts in designing and optimizing a compact system for the detection of the inter-Landau-level radiative transitions (i.e. Landau emission) in graphene devices.

We carry out a systematic evaluation for various techniques used to prepare the top-gate dielectric for a dual-gated graphene device. We introduce a thin-film transfer technique, with which we are able to place ultra-thin insulating sheets precisely on top of graphene. A hybrid top-gate dielectric comprised of naturally oxidized Al and thermally evaporated SiO₂ offers high-quality p - n junctions with high yield. In such a bipolar graphene device, electric fields applied by a global back-gate and a local top-gate enable independent control over the carrier type and density in two adjacent regions of the graphene sheet. It is possible to form p - n (or n - p), p - p and n - n junctions at the interface. Under quantum Hall conditions, the Hall and longitudinal resistances measured by multiple voltage contacts on the two sides of the junction show plateaux that agree quantitatively with the Landauer-Büttiker formula and the edge-mode mixing model. Local potentials probed before and after mode mixing provide direct evidence for a complete equilibration of edge states at the p - n interface.

This dissertation is dedicated to my family, especially to my wonderful wife for her sweet love, care, trust and advice throughout my doctoral program; to my beloved parents and sister for their endless love, unconditional support and constant encouragement.

Contents

Acknowledgments	iii
List of Figures	vi
Symbols and Abbreviations	xi
Chapter 1 Introduction	1
1.1 Massless Dirac fermions in a monolayer of carbon honeycomb lattice	1
1.2 Motivation	10
References	19
Chapter 2 Graphene-Based Device Fabrication	27
2.1 Mechanical exfoliation and optical identification of atomically thin films.....	27
2.2 Definition and deposition of metal contacts	39
2.3 Preparation of top-gate dielectric	43
2.3.1 Thermal evaporation of SiO _x	43
2.3.2 Metallic air bridge	45
2.3.3 Atomic layer deposition	47
2.3.4 Hybrid top-gate dielectric.....	51
2.3.5 Precise transfer of ultra-thin boron nitride films	52
References	55
Chapter 3 Electronic Transport in Graphene	59
3.1 Sample preparation and measurement methods	60
3.2 “Charge-neutrality-point” engineering via <i>in situ</i> annealing.....	62
References	73

Chapter 4 Magneto-Transport in Graphene	77
4.1 Experimental methods and measurement setup.....	78
4.2 Quantum Hall effect and Shubnikov-de Haas oscillations in graphene	82
4.3 The robust $\nu = 2$ quantum Hall state.....	89
References	93
Chapter 5 Transport in Gate-Controlled Graphene <i>p-n</i> Junctions	97
5.1 Sample preparation and measurement setup	98
5.2 Four-terminal transport at zero magnetic field.....	99
5.3 Four-terminal transport in the quantum Hall regime.....	104
5.4 Graphene <i>p-n-p</i> devices with boron nitride as the top-gate dielectric.....	114
5.4.1 Transferred BN films as the top-gate dielectric	114
5.4.2 Electrical characterizations	115
References	119
Chapter 6 Detection of Landau Emission from Graphene: System Design and	
Preliminary Optimizations	121
6.1 Inter-Landau-level transitions in graphene.....	122
6.2 System design and experimental methods.....	125
6.3 Some preliminary measurements.....	136
References	140
Summary	143
Curriculum Vitae	149

Acknowledgments

First and foremost, I would like to express my deep appreciation to my advisor, Prof. Klaus von Klitzing, for his constant support, insightful guidance and unceasing interest in the progress of my work. Working in his department has indeed been a great experience filled with challenging while exciting experiments and stimulating discussions. I have been so much amazed by Prof. von Klitzing's unrivaled expertise in grasping the essence of a complicated problem/phenomenon with a simple yet clear physics picture. His dedication and passion toward science have been a constant source of inspiration to us, and will continue driving me forward for the years to come.

I am greatly indebted to Prof. Franz Faupel, who is my “doctor father” and has co-advised my thesis. In my eyes, Prof. Faupel is not only a top-notch physicist and materials scientist, but also a fabulous mentor and teacher. Listening to his lectures has always been a great enjoyment. The amazing clarity in his guidance has made the course of tackling a difficult problem really joyful.

I am particularly grateful to Dr. Jurgen Smet, who has kindly allowed me to work in his group, proofread the manuscript of this thesis and consistently provided me all kinds of help whenever I need. Jurgen is a great person to work with and learn from. He has taught me so much in science as well as every aspect of life. Jurgen is not only a consummate experimentalist, but also a programming expert. Measurement programs composed by him are the paradigm of clarity, functionality and conciseness. I strived to implement his style when I wrote instrument drivers.

I would like to thank Dr. Thomas Keller for being my “external” advisor and for his constant interest in my work. I have benefited a lot from his patient, inspirational and

illuminating guidance. He taught me how to achieve inner tranquility and how to focus on the crucial part(s) of a difficult problem in order to solve it in an efficient way.

I owe much gratitude to Dr. Dong-Hun Chae, who is a dedicated scientist and has constantly helped me throughout my doctoral studies. We shared both the lab and office for years. In the early days of my PhD studies, Hun taught me a lot of experimental techniques concerning low temperature measurements. He generously shared with me all his recipes for sample preparation. He showed me step by step how to carry out electron beam lithography. He gave me much helpful advice on the development of communication skills, ranging from presentations to writing. I have been enjoying so much the enlightening discussions with him on scientific as well as cultural topics. I am always amazed by his insights.

I am very thankful to the magnificent technical support from Steffen Wahl, Manfred Schmid and Ingo Hagel, whose world-class expertise has helped solve so many tricky problems in the lab. I am much grateful to Dr. Jürgen Weis, Prof. Werner Dietsche, Thomas Reindl, Achim Güth and Ulrike Waizmann for their terrific support and kind help in the cleanroom. I appreciate very much the expert bonding support from Benjamin Stuhlhofer and Marion Hagel. I would like to acknowledge the nice collaborations with Peter Gorzelli and Joerg Lampart in building a variety of home-made electronics. Many thanks to Dr. Hagen Klauk and Dr. Ute Zschieschang for kindly sharing with me the magic of dissolving gold and gold-palladium-alloy with the combination of a few common chemicals.

My fellow group members and collaborators, Thomas Beringer, Benjamin Krauss, Dr. Dong-Su Lee, Benedikt Friess, Daniel Kärcher, Federico Paolucci, Ding Zhang, Johannes

Nübler, Dr. Frank Ospald and Dr. Denis Maryenko, have created a terrific environment around me. Working with them has been great fun. I have received tremendous help and learned a lot from them. I have enjoyed very much sharing opinions with Thomas on science, history, culture, IT, games, etc. I have been impressed by Frank and Daniel's sense of humor. I am thankful to Benjamin for telling me the difference between "Brezel" and "Berliner". I am grateful to Paul and Nina for their support in isolating graphene flakes. I would like to thank Hyeyeon Ryu and Frederik Ante for the stimulating discussions in the cleanroom and in the library.

I owe my sincere gratitude to Dr. Wing Fong Chu, Dr. Thomas Strunskus, Dr. Takayuki Iwasaki, Dr. Po-Wen Chiu, Dr. Yongqing Li and Dr. Burak Özdöl for all the kind help and inspirational discussions.

My cordial thanks also go to Ms. Ruth Jenz, Ms. Birgit King, Ms. Tanja Wengler, Ms. Sieglinde Kastaun and Ms. Claudia Martin for their administrative support and always friendly help.

List of Figures

Figure 1.1: Crystal and reciprocal lattice of graphene.....	2
Figure 1.2: Energy band structure of graphene.....	3
Figure 1.3: Pseudospin, motion direction and sublattices.	6
Figure 1.4: Tunneling through a potential step in a graphene <i>p-n</i> junction.....	8
Figure 1.5: Optical image showing graphene in pencil traces.....	11
Figure 1.6: Optical image of a graphene flake obtained by mechanical exfoliation.	12
Figure 2.1: Procedure of graphene preparation via mechanical exfoliation.....	27
Figure 2.2: Optical contrast comparison between single- and multi-layer graphite on an oxidized Si substrate.	30
Figure 2.3: Geometry of the trilayer system composed of graphene, SiO ₂ and Si.	30
Figure 2.4: Real and imaginary part of the complex index of refraction of Si and SiO ₂ in the visible range.....	32
Figure 2.5: Color plot of graphene's expected contrast as a function of wavelength and SiO ₂ thickness.	33
Figure 2.6: Schematic of an AA'-stacked hexagonal boron nitride (h-BN) crystal and optical image of a thin h-BN crystallite on an oxidized Si wafer.....	35
Figure 2.7: Calculated contrast of 2.5 nm thick h-BN as a function of wavelength and SiO ₂ thickness.	37
Figure 2.8: Expected contrast of h-BN on 300 nm thick SiO ₂ as a function of wavelength and h-BN thickness.	37

Figure 2.9: Contrast-enhanced optical images of a few h-BN crystallites with different thicknesses.	38
Figure 2.10: Schematic illustration of the fabrication procedure for electrical contacts.	39
Figure 2.11: Comparison between Au and AuPd microstructures.	42
Figure 2.12: Cross-section of a dual-gated graphene device with patterned or unpatterned SiO _x top-gate dielectric.....	44
Figure 2.13: Schematic illustration of the air-bridge fabrication process.....	46
Figure 2.14: SEM micrographs of suspended and collapsed air bridges after lift-off.	47
Figure 2.15: Four steps forming one reaction cycle in ALD (adapted from literature)...	48
Figure 2.16: AFM image of alumina on graphite and SiO ₂	50
Figure 2.17: Optical and SEM images of test structures with patterned ALD-grown dielectric.....	51
Figure 2.18: Cross-section and optical image of a bipolar graphene device featuring a patterned and hybrid top-gate dielectric..	52
Figure 2.19: Schematic representation outlining the transfer process used to fabricate BN-on-graphene devices and optical image of a finished sample.....	53
Figure 3.1: Schematic illustration of the “capacitor geometry” and a typical four-terminal measurement setup.....	61
Figure 3.2: Graphene resistivity and mobility as a function of back-gate voltage (carrier density) before and after annealing.....	63
Figure 3.3: Graphene conductivity versus applied back-gate voltage and a linear fit.....	66
Figure 3.4: Estimated carrier mean free path as a function of density at $T = 1.6$ K.	69
Figure 3.5: SEM image of a graphene sample after <i>in situ</i> vacuum annealing.	70

Figure 4.1: Four-terminal Hall-bar configuration for magneto-transport measurements and experimental setup for low-dissipation measurements.	81
Figure 4.2: Magneto-resistances showing unconventional quantum Hall effect in graphene.....	82
Figure 4.3: Magneto-conductivities develop with filling factor.	84
Figure 4.4: The $\nu = 0$ quantum Hall state probed with reduced excitation current.	86
Figure 4.5: Longitudinal and Hall resistivities as a function of magnetic field at a fixed carrier density of $\sim 2.2 \times 10^{12} \text{ cm}^{-2}$. Period of the Shubnikov-de Haas oscillations gives the carrier density in graphene.....	88
Figure 4.6: A large critical current density for the $\nu = 2$ quantum Hall state in graphene.	90
Figure 4.7: Quantum Hall effect in graphene under a high DC excitation current and at a high temperature.	91
Figure 5.1: Optical image of a double-gated graphene device and schematic of the four-terminal measurement setup.	98
Figure 5.2: Two-dimensional color plot of the longitudinal resistance in a dual-gated graphene device as a function of gate voltages at $B = 0 \text{ T}$ and $T = 1.5 \text{ K}$	100
Figure 5.3: I - V plots at various top- and back-gate voltages.	103
Figure 5.4: Expected Hall resistances in the non-top-gated and top-gated parts of a graphene layer as a function of gate voltages under quantum Hall conditions (at $B = 14 \text{ T}$).....	106
Figure 5.5: 2D color map of measured Hall resistance in the non-top-gated region at $B = 14 \text{ T}$	107

Figure 5.6: 2D color map of measured Hall resistance in the top-gated region at $B = 14$ T.	108
Figure 5.7: Schematic of quantum Hall edge modes in a double-gated graphene junction.	109
Figure 5.8: 2D color map of measured longitudinal resistances at $B = \pm 14$ T.	112
Figure 5.9: Optical images showing the transfer of an h-BN film onto a graphene sheet.	114
Figure 5.10: Optical image and cross-section view of a graphene $p-n-p$ device with transferred h-BN as the top-gate dielectric.	115
Figure 5.11: 2D color map of resistance across the top-gated region in a graphene $p-n-p$ device with transferred h-BN as the top-gate dielectric.....	116
Figure 5.12: SEM image of the top-gated area showing the presence of wrinkles in both h-BN and graphene sheets.	117
Figure 5.13: DC tunneling-like $I-V$ plots for thin h-BN layers with different thicknesses.	118
Figure 6.1: Calculated Landau level (LL) spectra of graphene as a function of magnetic field and schematic representation of a possible optical transition between the zeroth and first LL at $B = 14$ T.	124
Figure 6.2: Theoretically expected LL transition energies in graphene as a function of magnetic field.....	125
Figure 6.3: Optical image of the broadband Si:B photoconductive detector from IRLabs Inc.	126

Figure 6.4: Schematic and optical image of our sample holder assembly containing both the graphene emitter and the optics for mid-infrared radiation detection..... 127

Figure 6.5: Schematic of the circuit for the detection of inter-Landau-level radiative transitions in graphene. 129

Figure 6.6: Schematic diagram for the circuit inside a home-made detector bias-box. 130

Figure 6.7: Dark (leakage) current characteristic of our Si:B photodetector at various temperatures ($B = 0$ T). 131

Figure 6.8: Schematic diagram of a home-made high-impedance input buffer. 133

Figure 6.9: Schematic illustration of the edge states and “hot spots” in a graphene Hall-bar in the quantum Hall regime; concept and optical image of radiation-blocking structures. 134

Figure 6.10: Low temperature electrical characterization for the graphene emitter..... 136

Figure 6.11: Two-terminal source-drain resistance as a function of the back-gate voltage at $B = \pm 14$ T for the graphene emitter..... 137

Symbols & Abbreviations

Symbols

a	lattice constant (\AA)
\mathbf{a}	unit vector in crystal lattice
\mathbf{b}	basis vector in reciprocal lattice
B	magnetic field (T)
C	optical contrast; gate capacitance (nF/cm^2)
c	speed of light in vacuum
C^0	constant, $5 \times 10^{15} \text{V}^{-1} \text{s}^{-1}$
C_{bg}	back-gate capacitance (nF/cm^2)
C_{tg}	top-gate capacitance (nF/cm^2)
D	density of states
d	thickness (nm)
D^*	diffusion constant (m^2/s)
d_{bg}	thickness of back-gate dielectric (nm)
d_{tg}	thickness of top-gate dielectric (nm)
E	energy (eV or meV)
e	elementary charge
\bar{e}	electron(s)
E_F	Fermi energy (eV or meV)
f	frequency (Hz)
$h = 2\pi\hbar$	Planck constant
h^+	hole(s)
I	electric current (A)
I_C	QHE breakdown critical current (μA)
I_{sd}	source-drain excitation current (nA)
I_{tg}	top-gate leakage current (nA)
J	current density (A/m)
J_C	QHE breakdown critical current density (A/m)
\mathbf{k}	wavevector
k	Boltzmann constant
K, K'	corners of first Brillouin zone (FBZ)
\mathbf{K}, \mathbf{K}'	positions of FBZ corners in momentum space
k_F	Fermi wavevector

L	longitudinal separation (μm)
l_m	mean free path (nm)
M	high-symmetry point in FBZ
m_c	cyclotron mass (kg)
n	carrier density (cm^{-2}) in a two-dimensional (2D) layer
N	Landau level index
n_1	carrier density in non-top-gated region of a dual-gated device (cm^{-2})
n_2	carrier density in top-gated region of a dual-gated device (cm^{-2})
n_g	gate-induced carrier density (cm^{-2})
\tilde{n}_i	complex index of refraction, $i = 0, 1, 2, 3$
n_{im}	concentration of charged impurities (cm^{-2})
\mathbf{q}	wavevector
q_F	Fermi wavevector
R	resistance (Ω); total reflectance
$R_{contacts}$	sum of contact resistances (Ω)
R_H	Hall resistance in a dual-gated device (Ω)
r_i	relative index of refraction, $i = 1, 2, 3$
R_K	von Klitzing constant ($R_K = h/e^2 \approx 25812.81 \Omega$)
R_L	longitudinal resistance in a dual-gated device (Ω)
R_{wires}	sum of wire resistances (Ω)
R_{xx}	longitudinal resistance (Ω)
R_{xy}	Hall resistance (Ω)
s	proportionality factor, $s = [-0.01, -1.1]$
t	nearest-neighbor hopping energy (eV)
T	temperature (K)
T_F	Fermi temperature (K)
U_0	height of potential barrier (eV)
V	voltage (V)
V_{bg}	back-gate voltage
V_{bg}^0	back-gate voltage corresponding to global charge neutrality (V)
v_F	Fermi velocity
V_g^0	charge neutrality point (V)
V_H	Hall voltage in a dual-gated device (V)
V_L	longitudinal voltage in a dual-gated device (V)
V_{tg}	top-gate voltage

V_{ig}^0	top-gate voltage corresponding to global charge neutrality (V)
V_{xx}	longitudinal voltage (V)
V_{xy}	Hall voltage (V)
W	sample width (μm)
Z_{in}	input impedance ($\text{G}\Omega$)
α	fine structure constant
Γ	center of Brillouin zone
ΔN	difference between Landau level indices
$\Delta\rho_{xy}$	deviation of ρ_{xy} from ideally quantized value (Ω)
ϵ_0	permittivity of free space
ϵ_{bg}	(relative) dielectric constant of back-gate dielectric
ϵ_r	(relative) dielectric constant
ϵ_{ig}	(relative) dielectric constant of top-gate dielectric
η	ratio of gate coupling efficiencies
λ	wavelength (nm or μm)
μ	mobility (cm^2/Vs)
ρ	resistivity in 2D system (Ω or Ω/\square)
$\hat{\rho}$	2D resistivity tensor
ρ_{xx}	longitudinal resistivity in 2D system (Ω)
ρ_{xy}	Hall resistivity in 2D system (Ω)
σ	pseudospin (Pauli matrices)
σ	electrical conductivity in 2D system (Ω^{-1})
$\hat{\sigma}$	2D conductivity tensor
σ_{res}	residual conductivity (Ω^{-1})
σ_{xx}	longitudinal conductivity in 2D system (Ω^{-1})
σ_{xy}	Hall conductivity in 2D system (Ω^{-1})
τ	scattering time (s)
ν	filling factor
ν_1	filling factor in non-top-gated region of a dual-gated device
ν_2	filling factor in top-gated region of a dual-gated device
Φ_i	phase shift, $i = 1, 2$

Abbreviations

1D, 2D, 3D	one-, two-, three-dimensional
2DES	two-dimensional electron system
AC	alternating current
AFM	atomic force microscope
ALD	atomic layer deposition
CVD	chemical vapor deposition
DC	direct current
DOS	density of states
e-beam	electron beam
EBL	electron beam lithography
FBZ	first Brillouin zone
FWHM	full width at half maximum
GFET	graphene field effect transistor
GNR	graphene nanoribbon
h-BN	hexagonal boron nitride
HOPG	highly oriented pyrolytic graphite
HSQ	hydrogen silsesquioxane
IPA	Isopropanol
I-preamp	current preamplifier
LL	Landau level
MIBK	methyl isobutyl ketone
MIR	mid-infrared
MMA	methyl methacrylate
mw.	molecular weight
NMP	N-Methyl-2-pyrrolidone
PMMA	poly(methyl methacrylate)
PVD	physical vapor deposition
QED	quantum electrodynamics
QHE	quantum Hall effect
RGB	red-green-blue
SdHO	Shubnikov-de Haas oscillation
SEM	scanning electron microscope
TMA	trimethyl aluminum

V-preamp voltage preamplifier
VTI variable temperature insert

Chapter 1

Introduction

1.1 Massless Dirac fermions in a monolayer of carbon honeycomb lattice

Graphene is a one-atom-thick planar sheet of sp^2 -hybridized carbon atoms that are tightly packed into a two-dimensional (2D) honeycomb crystal lattice [1, 2]. It is a 2D allotrope of carbon, and can be regarded as the building block for graphitic materials of other dimensionalities, as long as they have the hexagonal arrangement of carbon atoms in common. For example, the graphene sheets can be stacked into 3D graphite or rolled into 1D single-wall nanotubes.

There are two types of C-C bonds (σ and π) in graphene. For each carbon atom in graphene, the sp^2 hybridization of $2s$, $2p_x$ and $2p_y$ valence orbitals leads to three inplane σ bonds and one π ($2p_z$) bond perpendicular to the graphene plane. Both the σ and the π bonds are accountable for the large binding energy as well as the elastic properties of the graphene sheet. Since the bonding and anti-bonding σ bands are separated by a large energy gap of >10 eV [3], they are often neglected in the calculations of the graphene band diagram in the low-energy regime.

Fig. 1.1(a) schematically illustrates the crystal lattice of graphene that contains two inequivalent (from a crystallographic point of view) sublattices labeled as A and B . This honeycomb structure can be viewed as a triangular Bravais lattice with a basis of two atoms (A and B) per unit cell. The unit vectors \mathbf{a}_1 and \mathbf{a}_2 are given by

$$\mathbf{a}_1 = \frac{a}{2}(3, \sqrt{3}), \quad \mathbf{a}_2 = \frac{a}{2}(3, -\sqrt{3}), \quad (1.1)$$

where $a \sim 1.42 \text{ \AA}$ [2] is the spacing between the nearest-neighbor carbon atoms. The basis vectors \mathbf{b}_1 and \mathbf{b}_2 in the reciprocal lattice can be readily obtained according to the relation $\mathbf{a}_i \cdot \mathbf{b}_j = 2\pi\delta_{ij}$, with $\delta_{ij} = 0$ when $i \neq j$ and $\delta_{ij} = 1$ when $i = j$. Thus we have

$$\mathbf{b}_1 = \frac{2\pi}{3a}(1, \sqrt{3}), \quad \mathbf{b}_2 = \frac{2\pi}{3a}(1, -\sqrt{3}), \quad (1.2)$$

as indicated in Fig. 1.1(b). The first Brillouin zone (FBZ) and its center Γ , together with the two inequivalent corners K and K' as well as the other crystallographic point M , are also shown in the same figure. The positions for K and K' in momentum space are given by

$$\mathbf{K} = \frac{2\pi}{3a}(1, \frac{1}{\sqrt{3}}), \quad \mathbf{K}' = \frac{2\pi}{3a}(1, -\frac{1}{\sqrt{3}}). \quad (1.3)$$

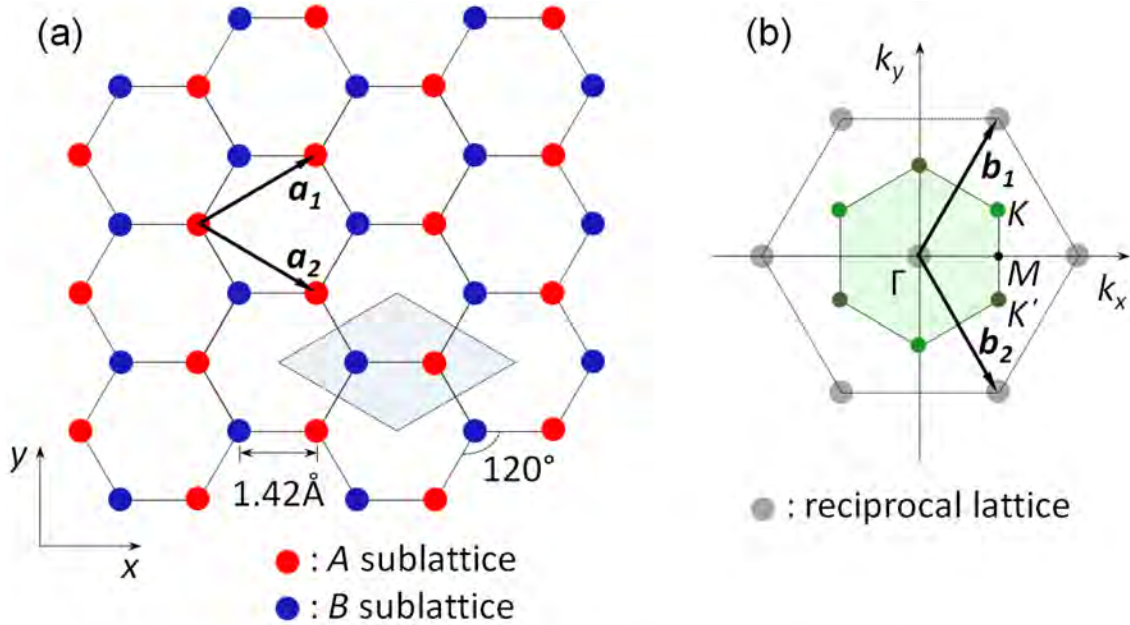


Figure 1.1: Honeycomb crystal lattice (a) and reciprocal lattice (b) of graphene. In (a), \mathbf{a}_1 and \mathbf{a}_2 are the lattice unit vectors and the shaded diamond indicates a unit cell that is comprised of two carbon atoms (blue and red). The base vectors \mathbf{b}_1 and \mathbf{b}_2 in (b) define the reciprocal lattice, and the shaded hexagon represents the first Brillouin zone (FBZ) with its center Γ and the two inequivalent corners K (green dots) and K' (olive green dots). The high-symmetry point M is also shown in (b).

The electronic spectrum near the K/K' points can be derived from a tight-binding Hamiltonian by considering only the nearest-neighbor interactions [4, 5]. The energy eigenstates of the Hamiltonian give the energy-momentum dispersion relation in the form [4]:

$$E_{\pm}(\mathbf{k}) = \pm t \sqrt{1 + 4 \cos \frac{3k_x a}{2} \cos \frac{\sqrt{3}k_y a}{2} + 4 \cos^2 \frac{\sqrt{3}k_y a}{2}}, \quad (1.4)$$

where $\mathbf{k} = (k_x, k_y)$ are the vectors that constitute the ensemble of the available electronic momenta (see Fig. 1.1(b)), and t is the transfer integral corresponding to the nearest-neighbor hopping energy with a magnitude of 2.9-3.1 eV [6].

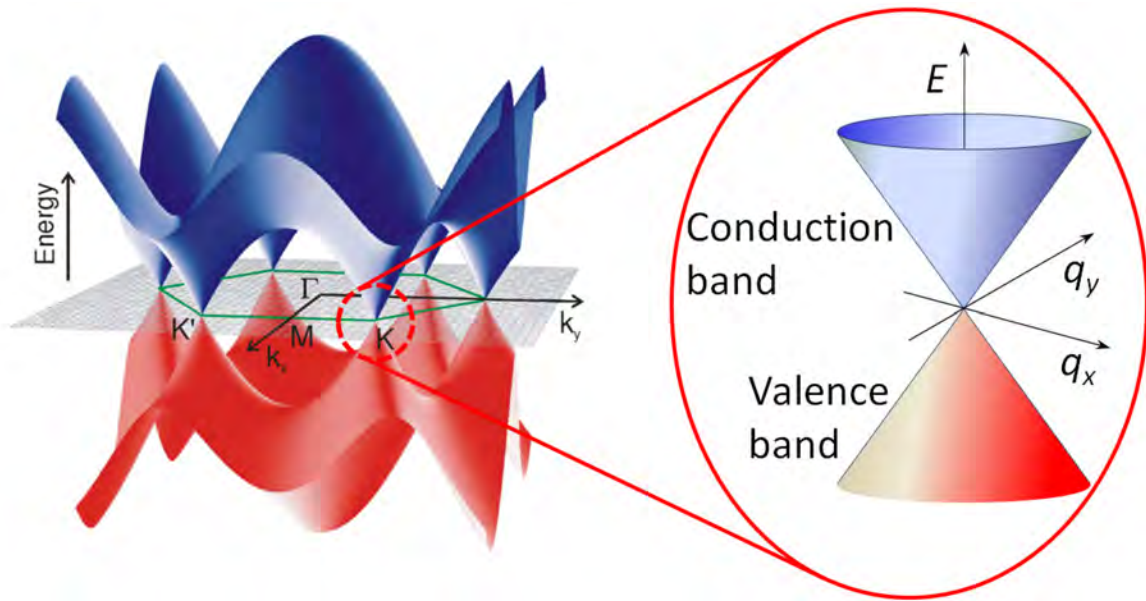


Figure 1.2: Energy band structure of graphene on the basis of Eq. 1.4. The π^* band (upper band) and the π band (lower band) touch at the six points located at the FBZ corners, where the Fermi level in neutral graphene is situated. In the vicinity of the zone corners, the dispersion relation is linear at low energies.

The band structure of graphene on the basis of Eq. 1.4 is plotted in Fig. 1.2. There are two bands in the diagram: the π^* band (i.e. the lowest conduction band) with energy $E > 0$ and the π band (i.e. the highest valence band) with $E < 0$. The two bands touch each other

(only) at the six K/K' points at the corners of the FBZ. Consequently, graphene can be considered as either a zero-gap semiconductor or a zero-overlap semimetal [1]. With one p_z electron per atom for the π - π^* bonding, in neutral (without any chemical or electrostatic doping) graphene at zero temperature ($T = 0$) the negative energy branch in Eq. 1.4 is fully occupied, while the positive energy branch is totally empty [3]. Hence, the zero energy here corresponds to the Fermi level E_F (or the charge neutrality point) in neutral graphene.

In the absence of disorder there are no free carriers in neutral graphene at zero temperature. At elevated temperatures, thermal excitations can promote electrons into the conduction band while leaving holes in the valence band. Alternatively, charge carriers can be put into the conduction or valence band by chemical doping or electrostatic doping (i.e. gating) [7, 8]. In this case, the Fermi level E_F (more precisely, chemical potential if $T > 0$) is shifted during the process. Graphene becomes n -doped (p -doped) if E_F eventually resides in the conduction band (valence band).

By expanding Eq. 1.4 near K/K' points in the low-energy regime (with $|E| < 1$ eV [1]), we obtain a linear dispersion relation [4]

$$E_{\pm}(\mathbf{q}) = \pm \hbar v_F |\mathbf{q}|, \quad (1.5)$$

where $\mathbf{q} = \mathbf{k} - \mathbf{K}$ (or $\mathbf{q} = \mathbf{k} - \mathbf{K}'$) is the wave vector relative to the K (or K') points, and v_F is the Fermi velocity given by $v_F = 3ta/2\hbar \approx 1 \times 10^6$ m/s. The conical low-energy spectrum $E(\mathbf{q})$ near the K/K' points is shown in the right inset of Fig. 1.2. Note that v_F in Eq. 1.5 is a constant independent of electron energy or momentum. The behavior of electrons (or holes) near the six corners of the graphene FBZ mimics that of relativistic particles with zero rest mass such as neutrinos [1]. In this regard, charge carriers in graphene can be

referred to as massless relativistic particles, with the Fermi velocity v_F substituting the speed of light. A linear electronic spectrum with zero bandgap as indicated by Eq. 1.5 renders a linear relation between the density of states (DOS) and energy near the zone corners. This is because $|\mathbf{q}|$ in Eq. 1.5 is proportional to the square root of the carrier density n (a positive and a negative n stand for electrons and holes, respectively) in two-dimensional graphene [9], and a linear dispersion yields

$$E \propto |\mathbf{q}| \propto \sqrt{|n|}. \quad (1.6)$$

The density of states D is then

$$D(E) = \frac{d|n|}{dE} \propto E, \quad (1.7)$$

where the proportionality factor is the same in magnitude and opposite in sign for electrons and holes. The linear relationship implies a vanishing DOS at the charge neutrality point ($E = 0$). This is in striking contrast to the DOS in conventional two-dimensional electron systems, where DOS is typically independent of the energy owing to the parabolic dispersion of the semiconductor hosting the 2D system [9].

In fact, the linear dispersion given by Eq. 1.5 depicts the energy eigenstates of the following 2D Dirac-like Hamiltonian for massless fermions near the K or K' point [2, 3, 10-12]:

$$\mathbf{H} = \hbar v_F \boldsymbol{\sigma} \cdot \hat{\mathbf{q}}, \quad (1.8)$$

where $\hat{\mathbf{q}}$ represents the operation $-i\nabla$ at \mathbf{q} , $\boldsymbol{\sigma}$'s are the pseudospin Pauli matrices, and v_F plays the role of the speed of light. For this reason, \mathbf{K} and \mathbf{K}' are given the name ‘‘Dirac points’’ and the conical band structures near the Dirac points are consequently called ‘‘Dirac Valleys’’. The low-energy charge carriers in graphene are regarded as ‘‘massless’’

Dirac fermions when they are not subject to an external magnetic field. Note that the pseudospin matrices at \mathbf{K}' are the complex conjugate of those at \mathbf{K} [2, 11].

When the Dirac-like Hamiltonian as shown in Eq. 1.8 is used to describe the quasiparticles in graphene, the pseudospin σ is essentially an index that defines the relative contributions of the A and B sublattices in the make-up of the quasiparticles [13]. The corresponding two-component description is very similar to the spinor wave functions in quantum electrodynamics (QED) and, therefore, is referred to as pseudospin [1, 13]. Simply put, the pseudo spin index in graphene indicates on which of the two sublattices a quasiparticle is located rather than the real spin of the electrons.

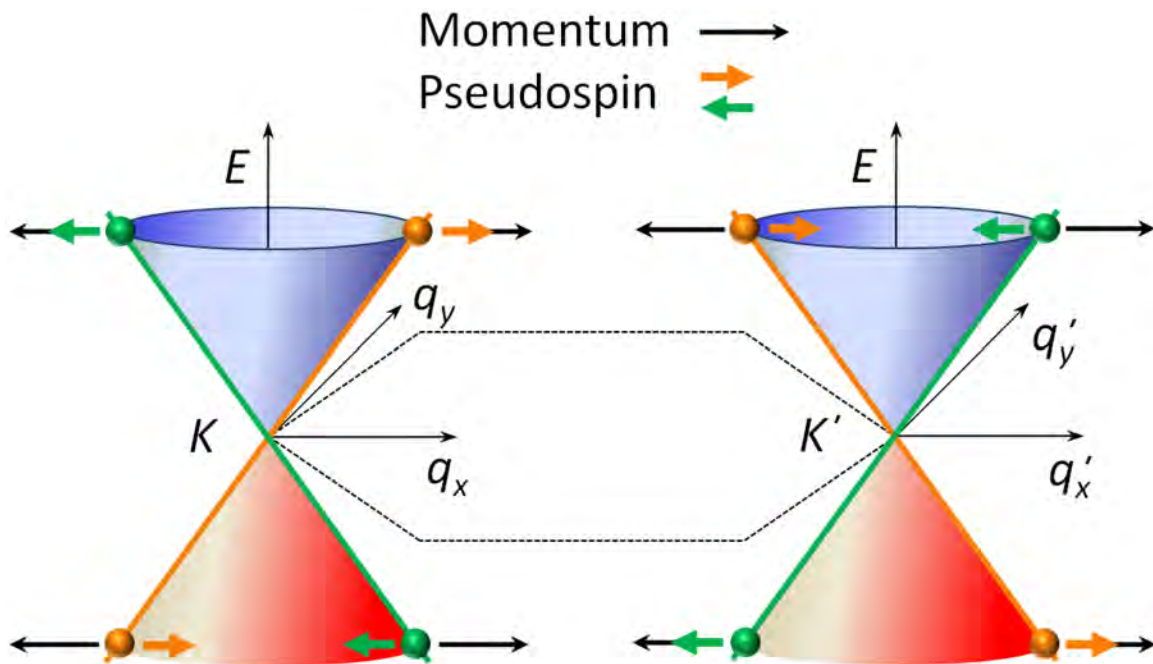


Figure 1.3: Relation between the pointing direction of pseudospin and the motion direction of Dirac quasiparticles in graphene. Pseudospin σ always aligns with the direction of momentum: near K point, σ is parallel to the motion direction of electrons and antiparallel to that of holes; whereas close to K' point, the relationship is reversed for both electrons and holes. The orange and green curves highlight the energy bands associated with the sublattices A and B , and the intersection of the curves indicates the origin of the linear spectrum near the Dirac points.

The conical spectrum of graphene near the zone corners can be considered as the result of crossing between the energy bands that are associated with sublattices A and B [13]. Electrons and holes belonging to the same branch of the linear spectrum (i.e. having the same sublattice origin) have pseudospin σ pointing in the same direction, as illustrated in Fig. 1.3. Near \mathbf{K} , σ is parallel to the direction of motion (as indicated by the direction of the corresponding wave vector \mathbf{q}) for electrons and antiparallel for holes [2, 13, 14]. A reverse relationship between the σ pointing and the motion direction of respective quasiparticles applies near \mathbf{K}' .

With the introduction of pseudospin, one may proceed to borrow from QED another important concept, “chirality” [12]. Chirality is defined as the projection of pseudospin σ on the direction of quasiparticle motion, and is positive (negative) for electrons (holes) close to \mathbf{K} [1, 2, 13]. This quantity is often used to describe the symmetry between the electron and hole parts of the low-energy spectrum of graphene [13].

Without an external magnetic field, conservation of pseudospin during intra-valley scattering in graphene leads to a suppression of backscattering in general [2, 13] (inter-valley scattering requires atomic-range external potentials in the graphene lattice and/or high temperatures [7] and is thus neglected here). The reason is as following. A backscattering process corresponds to a flip of the wave vector \mathbf{q} (i.e. $\mathbf{q} \rightarrow -\mathbf{q}$) and hence a reverse in the direction of pseudospin σ . This scenario violates the required conservation of pseudospin and is therefore forbidden.

Furthermore, pseudospin conservation can make a potential barrier in a relativistic electron’s propagation path appear transparent. In a graphene p - n junction with a sufficiently high [13] and infinitely steep potential step at the interface as shown in Fig.

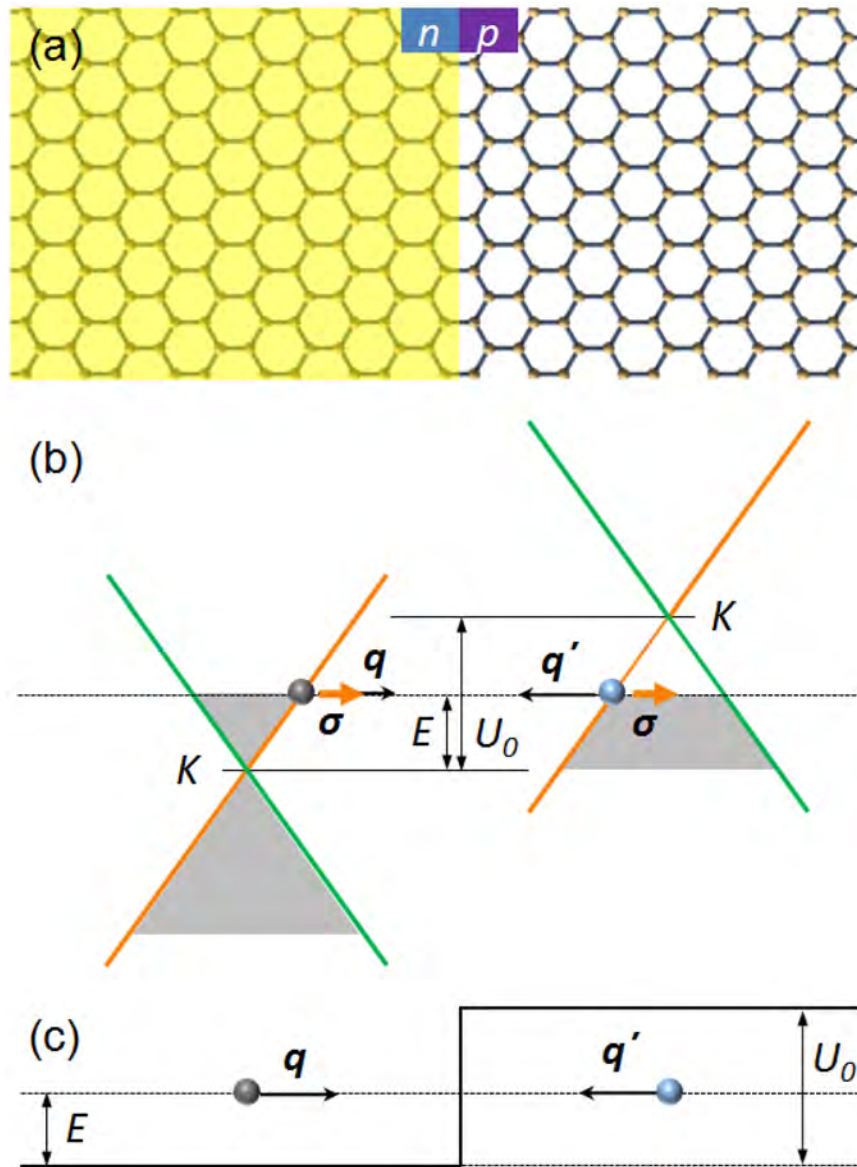


Figure 1.4: Tunneling through a potential step in a graphene p - n junction. The height of the potential step across the p - n interface illustrated in (a) is U_0 . It is larger than the electron energy E in the n region. The diagrams in (b) schematically show the band structure of a single K valley at the two sides of the potential step with the equilibrium Fermi level (dotted line in (b)) being the same at both sides. The Fermi level lies in the conduction band outside the potential barrier (left panel in (b)) and in the valence band inside the barrier (right panel in (b)). The gray filled areas in (b) indicate occupied states. Due to the conservation of pseudospin (indicated by the orange arrows in (b) that always point to the right), the motion of an electron propagating normally toward the barrier (left hand side in (c)) is continued by a hole moving in the opposite direction inside the barrier (right hand side in (c)). Thus, a transmission with 100% efficiency through the barrier is achieved.

1.4, a normally incident electron-like state from the left hand side can tunnel with 100%

probability into a hole-like state on the right hand side across the p - n interface [2, 13]. During the process, pseudospin is conserved within the Dirac valley and a back reflection of the electron is prevented. The propagation of the electron is continued by a hole that travels in the opposite direction on the other side of the junction, as illustrated in Fig. 1.4. The current flow through the graphene p - n junction should therefore be continuous without showing any common-diode-like behavior (some experimental evidence will be discussed in Chapter 5).

In a sufficiently strong magnetic field perpendicular to the graphene plane, the linear density of states (DOS) in graphene (Eq. 1.7) is quantized into a series of discrete energy levels, i.e. Landau levels (LLs). The unevenly spaced LLs in graphene have a square-root dependence on the magnetic field B with a peculiar LL at zero energy resulting from the particle-hole symmetry [15-17]. The existence of this unique zero-energy LL leads to an unconventional (integer) quantum Hall effect (QHE) with a half-integer shift in the quantization conditions (compared to the QHE in the conventional two-dimensional electron systems) [16, 18, 19].

The shift of $\frac{1}{2}$ in the QHE sequence can also be explained in terms of a Berry's phase of π in graphene [14, 18-20]. In a perpendicular magnetic field, orbital motion of the massless Dirac fermions in \mathbf{q} space leads to the rotation of pseudospin. A 2π pseudospin rotation in \mathbf{q} gives rise to a phase change of π ("Berry's phase") in the wave function that describes the electronic states near a Dirac point [14]. A Berry's phase of π leads to a π -shift (again, compared to the conventional two-dimensional electron systems) in the phase of magneto-oscillations in graphene and, in the extreme quantum limit, to an unconventional $\frac{1}{2}$ -shifted QHE [1].

Although graphene's neutrino-like linear dispersion at low energies implies "massless" particles, Dirac fermions moving in a magnetic field take on a finite cyclotron mass m_c . Experimentally, m_c is related to the carrier density n by $m_c = \hbar\sqrt{\pi|n|}/v_F$ [18, 19]. This immediately yields

$$m_c = \frac{\hbar q_F}{v_F} = \frac{\hbar v_F q_F}{v_F^2} = \frac{|E_F|}{v_F^2}, \quad (1.9)$$

where q_F is the Fermi wave vector given by the identity $q_F = \sqrt{\pi|n|}$ [9]. Eq. 1.9 provides evidence for the existence of massless Dirac quasiparticles in graphene and, accordingly, m_c can be taken as the "relativistic" mass of the Dirac fermions with v_F playing the role of speed of light.

1.2 Motivation

In principle, graphene has been in "production" ever since the invention of the pencil in the year 1564 [21]. Whenever one writes with a graphite pencil, due to the weak van der Waals coupling between graphite layers graphite traces are left on the surface of the material for writing upon (e.g. paper, wood, metal, glass, etc.). Among the produced graphene stacks, there may be monolayer graphene sheets somewhere (see Fig. 1.5). However, in history 2D crystals like graphene used to be presumed not to exist in the free state (i.e. it was assumed impossible to produce 2D crystals in a non-epitaxial way). It was argued that thermal fluctuations in a low-dimensional crystal lattice would destroy the long-range order of the crystal at any finite temperature [1, 22-25]. Then in 2004 Geim and his colleagues at the University of Manchester demonstrated that it IS possible to obtain 2D crystals [8]. For the first time they successfully isolated (micron-sized

monolayer) graphene flakes on top of oxidized silicon wafers with a carefully chosen thickness of SiO₂ (the optical effect that makes graphene visible on certain substrates in an optical microscope will be discussed in Chapter 2), and unambiguously showed that various atomically thin 2D crystals besides graphene remain stable even under ambient conditions [8, 26]. Later on, researchers discovered that graphene sheets up to tens of microns in size do not have to rest on supporting substrates but can be freely suspended from a scaffold structure (e.g. the support grid for a transmission electron microscope) [27, 28]. The mechanical stabilization of a graphene membrane on a substrate or scaffold is achieved by the formation of ripples with out-of-plane deformations up to 1 nm [27]. This gentle crumpling leads to a gain in elastic energy but suppresses thermal vibrations [29].

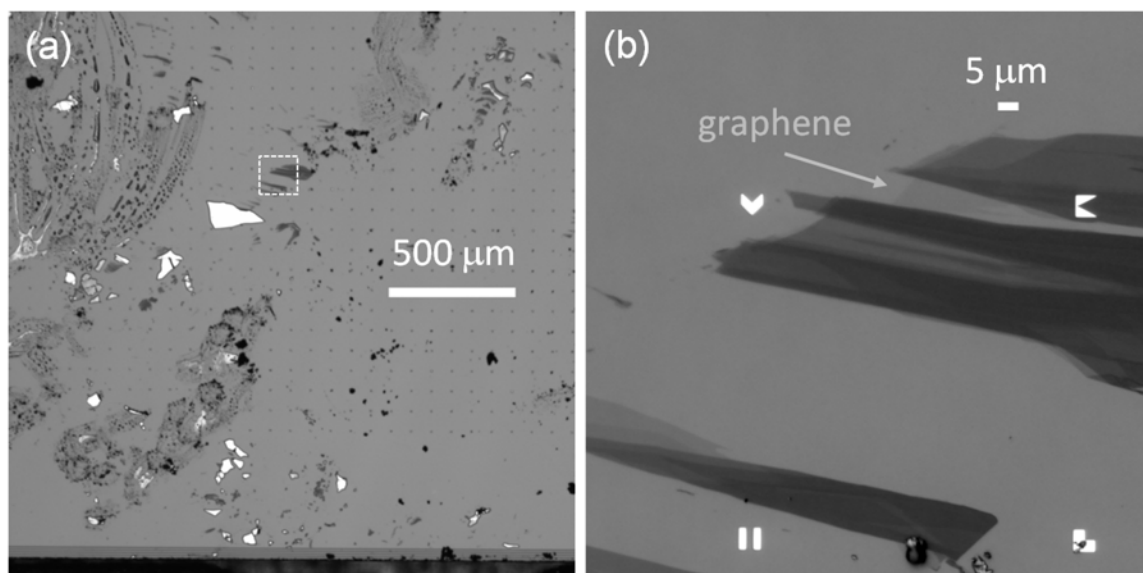


Figure 1.5: (a) Optical micrograph for the pencil traces on the surface of an oxidized silicon wafer. In the area of the dashed box in (a), (monolayer) graphene is spotted among the graphite debris and the corresponding zoomed-in image is shown in (b). The light-gray arrow in (b) indicates the location of the graphene sheet.

In their seminal experiments reported in 2004 [8], Geim and his colleagues introduced the so-called “micromechanical cleavage” method (a.k.a. “mechanical

exfoliation” or simply “Scotch® tape method”) to prepare the graphene flakes. With this technique, very thin graphitic sheets are essentially peeled off a graphite substrate (e.g. highly oriented pyrolytic graphite or natural graphite) by a moderately adhesive polymer tape and then pressed onto the surface of an oxidized silicon wafer. The isolated potential monolayers on top of SiO₂ are subsequently identified either by their optical contrast [30], their Raman fingerprints [31, 32], their thickness in AFM topography [8, 26], or their magneto-transport characteristics [18, 19]. To date, via mechanical exfoliation we are able to obtain high-electronic-quality single-crystalline (monolayer) graphene flakes from a few to tens of microns in size (see Fig. 1.6). In fact, we have used this technique to prepare all the (monolayer) graphene materials studied in this dissertation.

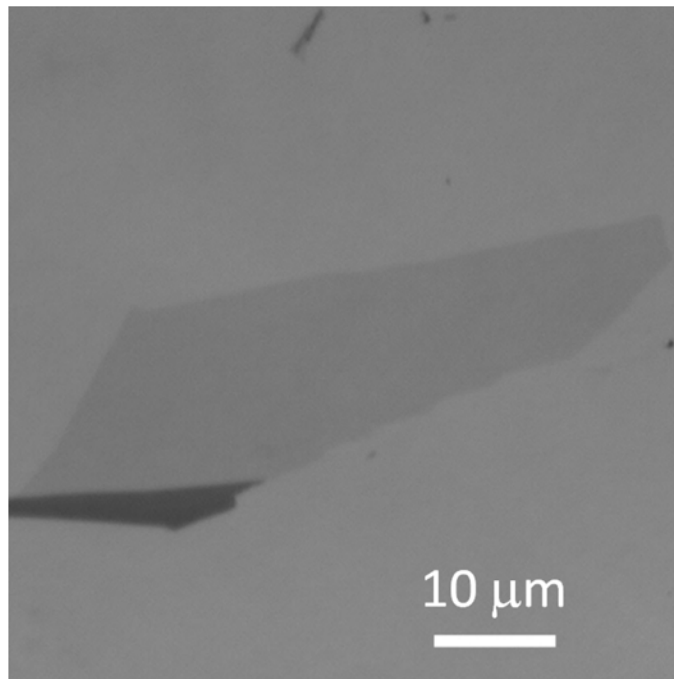


Figure 1.6: Optical image of a relatively large graphene flake obtained by mechanical exfoliation.

Although manually exfoliated graphene has met most of the requirements from research purposes, the low throughput resulting from the time-consuming cleavage-scan-

selection procedure is inadequate for mass production. Hence, finding alternative routes for an industrially scalable production has been the focus of a large amount of research activities shortly after the first isolation of graphene. A direct upgrade to manual exfoliation is the introduction of automated cleavage using ultrasonication [33]. This leads to submicron graphene crystallites in liquid suspension, which can subsequently be utilized to make polycrystalline films or composite materials. Another solution-based approach for the production of graphene is the exfoliation and reduction of graphite oxide (layered stacks of oxidized graphite with AB stacking) dispersed in various solvents [34-40]. The chemically derived graphene is then deposited onto appropriate substrates for device fabrication. Generally, graphene produced in solutions suffers from relatively small crystallites and a high density of defects [41]. To obtain high-quality graphene wafers, epitaxial growth on some specifically chosen platforms seems more desirable. Large-area graphene growth has been achieved on SiC wafer surfaces as a result of the thermal decomposition of SiC at high temperatures (>1300 °C) either in ultrahigh vacuum [42-44] or at atmospheric pressure [45]. Successful wafer-scale graphene growth on epitaxially matched surfaces of transition metals such as Ni has been reported [46, 47]. In this case, chemical vapor deposition (CVD) of graphene on Ni (111) surface is realized in a self-terminating manner with little lattice mismatch [48]. Graphene growth on Cu films is another exciting application of the CVD approach [49-51]. With this technique, graphene in principle can be deposited on flexible roll-type Cu foils with infinite length and/or width. The role-to-role production of 30-inch graphene films with an excellent electronic quality has already been demonstrated [52].

Graphene is considered as one of the candidate materials for post-silicon electronics [53], owing to its rich and fascinating electronic and optical properties. High-speed graphene field-effect-transistors (GFETs) operated at room temperature with a cut-off frequency of 155 GHz and a gate length of 40 nm has been fabricated [54], thanks to the extraordinarily high intrinsic mobility [55-57] and saturation velocity [58, 59] of the charge carriers in graphene. Combined with the fact that graphene has a fast photoresponse [60] and a high optical transparency [61] with a broadband photoabsorption [6] that can be controlled by electrical gating [62, 63], graphene is very promising for such integrated opto-electronic applications as transparent while flexible electrodes [47, 52], ultrafast photodetectors [60, 64] and broadband optical modulators [65]. In general, GFETs with channels made of large-area (monolayer) graphene have a low *on/off* ratio due to the lack of a bandgap in graphene. However, by constraining graphene in one dimension a bandgap that is approximately inversely proportional to the width of the graphene channel can be introduced in graphene nanoribbons (GNRs) [66, 67]. A bandgap above 200 meV has been observed in sub-20-nm GNRs [67, 68] and an *on/off* ratio in excess of 10^6 has been reported [68, 69]. To date, making very narrow GNRs with well-defined edges [70, 71] remains technically challenging and has motivated a lot of research efforts. Due to its large surface-area-to-weight ratio (a.k.a. specific surface area, $\sim 2630 \text{ m}^2/\text{g}$ [72]) and high electrical conductivity, graphene as well as its chemical modifications has tremendous potential for clean energy devices such as supercapacitors. Electrochemical double layer capacitor cells with large gravimetric capacitance and energy density have been successfully constructed [72-74]. A large specific surface area and a metal-like electrical conductivity that is extremely sensitive to

the adsorbed molecules [75] also make graphene a candidate for chemical sensors. The low Johnson noise level in graphene, which results from the high conductivity and a very low density of lattice defects, enables graphene to detect the adsorption and desorption of individual gas molecules [75].

To summarize, graphene is a marvelous material that has attracted tremendous interest. The remarkable electronic properties of graphene ensure its enormous potential in novel electron devices with exceptional performances. The present dissertation aims to contribute to the development of reliably working fabrication techniques for high-electronic-quality gated graphene devices, to the better understanding of the electronic properties of some graphene-based electron devices by means of multi-terminal transport measurements, as well as to the preliminary exploration of graphene's possible applications in quantum resistance metrology and Landau emitters.

The organization of this dissertation is as following:

In Chapter 2, we introduce our recipe for a quick estimation of the thickness of thin films exfoliated on top of SiO₂ substrates. This approach is based on the relationship between the optical contrast and thickness of the supported films. A description about our fabrication procedure for multi-terminal graphene devices follows. We then carry out a systematic evaluation on various techniques for the preparation of the top-gate dielectric for a bipolar graphene device. We find that a hybrid top-gate dielectric comprised of naturally oxidized Al and thermally evaporated SiO₂ provides us high-quality *p-n* junctions with a high yield. This chapter concludes with the introduction of a thin-film transfer technique, with which we are able to place ultra-thin insulating sheets precisely on top of graphene.

In Chapter 3, we demonstrate that careful substrate-cleaning and lift-off render a high Drude mobility in our graphene samples prior to any thermal treatment, and that an *in situ* vacuum annealing is capable of shifting the charge neutrality point of a graphene device to nearly 0 V with however limited improvement on carrier mobility. We show that a self-consistent Boltzmann formalism within the random phase approximation not only adequately describes the zero-field diffusive transport of our high-quality devices at reasonably large carrier densities, but also justifies the estimation for charged-impurity concentration based on the width of the resistance peak in the electric field effect. Our surface morphology investigations and the surface study reported by other research groups show that organic residues, ripples and wrinkles on the graphene sheet, dangling bonds on SiO₂ surface and trapped charges on (or near) the surface of SiO₂ may be the major sources of charged impurities in our graphene devices.

In Chapter 4, we probe the quantum Hall effect (QHE) in graphene using a four-terminal configuration in a magnetic field perpendicular to the graphene plane. Besides the unconventional $\frac{1}{2}$ -shifted integer QHE, we observe a quantum Hall state at filling factor $\nu = 0$ in high-quality samples under very low excitation currents. We demonstrate the extraction of the back-gate capacitance from the Shubnikov-de Haas (SdH) oscillations in graphene. The result justifies the simple parallel-plate capacitor model as introduced in Chapter 3. We proceed to measure a large critical current associated with the breakdown of the $\nu = 2$ quantum Hall state. The observed extraordinarily robust QHE at $\nu = 2$ shows that graphene is an excellent candidate material for the quantum resistance standard.

In Chapter 5, we report on four-terminal transport measurements in high-quality bipolar graphene devices featuring a hybrid top-gate dielectric. Electric fields applied by a global back-gate and a local top-gate enable independent control over the carrier type and density in two adjacent regions of the graphene sheet, allowing p - n (or n - p), p - p and n - n junctions to be formed at the interface. Under quantum Hall conditions, the Hall and longitudinal resistances probed by multiple voltage contacts on the two sides of the junction show plateaux which agree quantitatively with the Landauer-Büttiker formula [76] and the mode mixing model [77]. In this chapter, we also discuss the electrical characterizations on graphene p - n - p devices featuring an extremely thin (< 5 nm) h-BN (hexagonal boron nitride) top-gate dielectric that is prepared by a precise transfer of exfoliated h-BN films as introduced in Chapter 2. The top gate is found to possess a very high coupling efficiency and a rather low leakage current.

In Chapter 6, we report on our preliminary attempts in designing and optimizing a compact system for the detection of the inter-Landau-level radiative transitions (i.e. Landau emission) in graphene devices. The emission power is estimated to be extremely low ($< 10^{-11}$ W), and the photodetector has to be operated in a highly resistive state due to the lack of background radiation. Various efforts in improving the sensibility of the detection system and reducing the noise level in the circuit are discussed. We introduce a non-destructive deposition of radiation-blocking structures on top of the two “hot spots” (i.e. energy dissipation corners in the quantum Hall regime) along one diagonal of the graphene Hall-bar, such that the Landau radiation can be selectively blocked out depending on the direction of the magnetic field. Then even for the same amount of dissipated power in the graphene emitter, the Landau radiation that reaches the

photodetector differs. By this means, the graphene emitter itself provides a reference for the extraction of the radiation signal.

References

- [1] A. K. Geim and K. S. Novoselov, *The rise of graphene*, Nature Materials **6**, 183-191 (2007).
- [2] A. H. Castro Neto, F. Guinea, N. M. R. Peres, K. S. Novoselov, and A. K. Geim, *The electronic properties of graphene*, Reviews of Modern Physics **81**, 109-162 (2009).
- [3] J. C. Charlier, P. C. Eklund, J. Zhu, and A. C. Ferrari, *Electron and phonon properties of graphene: Their relationship with carbon nanotubes*, Topics in Applied Physics **111**, 673-709 (2008).
- [4] P. R. Wallace, *The band theory of graphite*, Physical Review **71**, 622 (1947).
- [5] J. C. Charlier, X. Blase, and S. Roche, *Electronic and transport properties of nanotubes*, Reviews of Modern Physics **79**, 677-732 (2007).
- [6] F. Bonaccorso, Z. Sun, T. Hasan, and A. C. Ferrari, *Graphene photonics and optoelectronics*, Nature Photonics **4**, 611-622 (2010).
- [7] S. Das Sarma, S. Adam, E. H. Hwang, and E. Rossi, *Electronic transport in two-dimensional graphene*, Reviews of Modern Physics **83**, 407 (2011).
- [8] K. S. Novoselov, A. K. Geim, S. V. Morozov, D. Jiang, Y. Zhang, S. V. Dubonos, I. V. Grigorieva, and A. A. Firsov, *Electric field effect in atomically thin carbon films*, Science **306**, 666-669 (2004).
- [9] C. W. J. Beenakker and H. van Houten, *Quantum transport in semiconductor nanostructures*, Solid State Physics **44**, 1-228 (1991).
- [10] J. C. Slonczewski and P. R. Weiss, *Band structure of graphite*, Physical Review **109**, 272 (1958).

- [11] G. W. Semenoff, *Condensed-matter simulation of a three-dimensional anomaly*, Physical Review Letters **53**, 2449-2452 (1984).
- [12] F. D. M. Haldane, *Model for a quantum Hall effect without Landau levels: Condensed-matter realization of the 'parity anomaly'*, Physical Review Letters **61**, 2015-2018 (1988).
- [13] M. Katsnelson, K. S. Novoselov, and A. K. Geim, *Chiral tunnelling and the Klein paradox in graphene*, Nature Physics **2**, 620-625 (2006).
- [14] T. Ando, T. Nakaishi, and R. Saito, *Berry's phase and absence of back scattering in carbon nanotubes*, Journal of the Physical Society of Japan **67**, 2857-2862 (1998).
- [15] Y. Zheng and T. Ando, *Hall conductivity of a two-dimensional graphite system*, Physical Review B **65**, 245420 (2002).
- [16] V. P. Gusynin and S. G. Sharapov, *Unconventional integer quantum Hall effect in graphene*, Physical Review Letters **95**, 146801 (2005).
- [17] N. M. R. Peres, F. Guinea, and A. H. Castro Neto, *Electronic properties of disordered two-dimensional carbon*, Physical Review B **73**, 125411 (2006).
- [18] K. S. Novoselov, A. K. Geim, S. V. Morozov, D. Jiang, M. I. Katsnelson, I. V. Grigorieva, S. V. Dubonos, and A. A. Firsov, *Two-dimensional gas of massless Dirac fermions in graphene*, Nature **438**, 197-200 (2005).
- [19] Y. Zhang, Y. W. Tan, H. L. Stormer, and P. Kim, *Experimental observation of the quantum Hall effect and Berry's phase in graphene*, Nature **438**, 201-204 (2005).
- [20] G. P. Mikitik and Y. V. Sharlai, *Manifestation of Berry's phase in metal physics*, Physical Review Letters **82**, 2147-2150 (1999).
- [21] H. Petroski, *The pencil: a history of design and circumstance* (Knopf, 1989).
- [22] R. E. Peierls, *Quelques proprietes typiques des corps solides*, Ann. I. H. Poincare **5**, 177-222 (1935).

- [23] L. D. Landau, *Zur Theorie der Phasenumwandlungen II*, Phys. Z. Sowjetunion **11**, 26-35 (1937).
- [24] L. D. Landau and E. M. Lifshitz, *Statistical physics, Part I* (Pergamon, 1980).
- [25] N. D. Mermin, *Crystalline order in two dimensions*, Physical Review **176**, 250-254 (1968).
- [26] K. S. Novoselov, D. Jiang, F. Schedin, T. J. Booth, V. V. Khotkevich, S. V. Morozov, and A. K. Geim, *Two-dimensional atomic crystals*, Proceedings of the National Academy of Sciences of the United States of America **102**, 10451-10453 (2005).
- [27] J. C. Meyer, A. K. Geim, M. I. Katsnelson, K. S. Novoselov, T. J. Booth, and S. Roth, *The structure of suspended graphene sheets*, Nature **446**, 60-63 (2007).
- [28] T. J. Booth, P. Blake, R. R. Nair, D. Jiang, E. W. Hill, U. Bangert, A. Bleloch, M. Gass, K. S. Novoselov, M. I. Katsnelson, and A. K. Geim, *Macroscopic graphene membranes and their extraordinary stiffness*, Nano Letters **8**, 2442-2446 (2008).
- [29] D. R. Nelson, T. Piran, and S. Weinberg, *Statistical mechanics of membranes and surfaces* (World Scientific, 2 ed., 2004).
- [30] P. Blake, E. W. Hill, A. H. C. Neto, K. S. Novoselov, D. Jiang, R. Yang, T. J. Booth, and A. K. Geim, *Making graphene visible*, Applied Physics Letters **91**, 063124 (2007).
- [31] A. C. Ferrari, J. C. Meyer, V. Scardaci, C. Casiraghi, M. Lazzeri, F. Mauri, S. Piscanec, D. Jiang, K. S. Novoselov, S. Roth, and A. K. Geim, *Raman spectrum of graphene and graphene layers*, Physical Review Letters **97**, 187401 (2006).
- [32] A. Gupta, G. Chen, P. Joshi, S. Tadigadapa, and P. C. Eklund, *Raman scattering from high-frequency phonons in supported n-graphene layer films*, Nano Letters **6**, 2667-2673 (2006).

- [33] Y. Hernandez, V. Nicolosi, M. Lotya, F. M. Blighe, Z. Sun, S. De, I. T. McGovern, B. Holland, M. Byrne, Y. K. Gun'ko, J. J. Boland, P. Niraj, G. Duesberg, S. Krishnamurthy, R. Goodhue, J. Hutchison, V. Scardaci, A. C. Ferrari, and J. N. Coleman, *High-yield production of graphene by liquid-phase exfoliation of graphite*, *Nature Nanotechnology* **3**, 563-568 (2008).
- [34] S. Stankovich, D. A. Dikin, G. H. B. Dommett, K. M. Kohlhaas, E. J. Zimney, E. A. Stach, R. D. Piner, S. T. Nguyen, and R. S. Ruoff, *Graphene-based composite materials*, *Nature* **442**, 282-286 (2006).
- [35] D. A. Dikin, S. Stankovich, E. J. Zimney, R. D. Piner, G. H. B. Dommett, G. Evmenenko, S. T. Nguyen, and R. S. Ruoff, *Preparation and characterization of graphene oxide paper*, *Nature* **448**, 457-460 (2007).
- [36] H.-K. Jeong, Y. P. Lee, R. J. W. E. Lahaye, M.-H. Park, K. H. An, I. J. Kim, C.-W. Yang, C. Y. Park, R. S. Ruoff, and Y. H. Lee, *Evidence of graphitic AB stacking order of graphite oxides*, *Journal of the American Chemical Society* **130**, 1362-1366 (2008).
- [37] D. Li, M. B. Muller, S. Gilje, R. B. Kaner, and G. G. Wallace, *Processable aqueous dispersions of graphene nanosheets*, *Nature Nanotechnology* **3**, 101-105 (2008).
- [38] X. Li, G. Zhang, X. Bai, X. Sun, X. Wang, E. Wang, and H. Dai, *Highly conducting graphene sheets and Langmuir-Blodgett films*, *Nature Nanotechnology* **3**, 538-542 (2008).
- [39] L. J. Cote, F. Kim, and J. Huang, *Langmuir-Blodgett assembly of graphite oxide single layers*, *Journal of the American Chemical Society* **131**, 1043-1049 (2008).
- [40] V. C. Tung, M. J. Allen, Y. Yang, and R. B. Kaner, *High-throughput solution processing of large-scale graphene*, *Nature nanotechnology* **4**, 25-29 (2009).
- [41] S. Stankovich, D. A. Dikin, R. D. Piner, K. A. Kohlhaas, A. Kleinhammes, Y. Jia, Y. Wu, S. T. Nguyen, and R. S. Ruoff, *Synthesis of graphene-based nanosheets via chemical reduction of exfoliated graphite oxide*, *Carbon* **45**, 1558-1565 (2007).

- [42] C. Berger, Z. Song, T. Li, X. Li, A. Y. Ogbazghi, R. Feng, Z. Dai, A. N. Marchenkov, E. H. Conrad, P. N. First, and W. A. de Heer, *Ultrathin epitaxial graphite: 2D electron gas properties and a route toward graphene-based nanoelectronics*, The Journal of Physical Chemistry B **108**, 19912-19916 (2004).
- [43] C. Berger, Z. Song, X. Li, X. Wu, N. Brown, C. Naud, D. Mayou, T. Li, J. Hass, A. N. Marchenkov, E. H. Conrad, P. N. First, and W. A. de Heer, *Electronic confinement and coherence in patterned epitaxial graphene*, Science **312**, 1191-1196 (2006).
- [44] W. A. de Heer, C. Berger, X. Wu, P. N. First, E. H. Conrad, X. Li, T. Li, M. Sprinkle, J. Hass, M. L. Sadowski, M. Potemski, and G. Martinez, *Epitaxial graphene*, Solid State Communications **143**, 92-100 (2007).
- [45] K. V. Emtsev, A. Bostwick, K. Horn, J. Jobst, G. L. Kellogg, L. Ley, J. L. McChesney, T. Ohta, S. A. Reshanov, J. Röhrl, E. Rotenberg, A. K. Schmid, D. Waldmann, H. B. Weber, and T. Seyller, *Towards wafer-size graphene layers by atmospheric pressure graphitization of silicon carbide*, Nature Materials **8**, 203-207 (2009).
- [46] A. Reina, X. Jia, J. Ho, D. Nezich, H. Son, V. Bulovic, M. S. Dresselhaus, and K. Jing, *Large area, few-layer graphene films on arbitrary substrates by chemical vapor deposition*, Nano Letters **9**, 30-35 (2009).
- [47] K. S. Kim, Y. Zhao, H. Jang, S. Y. Lee, J. M. Kim, J. H. Ahn, P. Kim, J. Y. Choi, and B. H. Hong, *Large-scale pattern growth of graphene films for stretchable transparent electrodes*, Nature **457**, 706-710 (2009).
- [48] A. Grueneis and D. V. Vyalikh, *Tunable hybridization between electronic states of graphene and a metal surface*, Physical Review B **77**, 193401 (2008).
- [49] X. Li, Y. Zhu, W. Cai, M. Borysiak, B. Han, D. Chen, R. D. Piner, L. Colombo, and R. S. Ruoff, *Transfer of large-area graphene films for high-performance transparent conductive electrodes*, Nano Letters **9**, 4359-4363 (2009).

- [50] X. Li, W. Cai, J. An, S. Kim, J. Nah, D. Yang, R. Piner, A. Velamakanni, I. Jung, E. Tutuc, S. K. Banerjee, L. Colombo, and R. S. Ruoff, *Large-area synthesis of high-quality and uniform graphene films on copper foils*, *Science* **324**, 1312-1314 (2009).
- [51] X. Li, W. Cai, L. Colombo, and R. S. Ruoff, *Evolution of graphene growth on Ni and Cu by carbon isotope labeling*, *Nano Letters* **9**, 4268-4272 (2009).
- [52] S. Bae, H. Kim, Y. Lee, X. Xu, J.-S. Park, Y. Zheng, J. Balakrishnan, T. Lei, H. Ri Kim, Y. I. Song, Y.-J. Kim, K. S. Kim, B. Ozyilmaz, J.-H. Ahn, B. H. Hong, and S. Iijima, *Roll-to-roll production of 30-inch graphene films for transparent electrodes*, *Nature Nanotechnology* **5**, 574-578 (2010).
- [53] F. Schwierz, *Graphene transistors*, *Nature Nanotechnology* **5**, 487-496 (2010).
- [54] Y. Wu, Y.-m. Lin, A. A. Bol, K. A. Jenkins, F. Xia, D. B. Farmer, Y. Zhu, and P. Avouris, *High-frequency, scaled graphene transistors on diamond-like carbon*, *Nature* **472**, 74-78 (2011).
- [55] S. V. Morozov, K. S. Novoselov, M. I. Katsnelson, F. Schedin, D. C. Elias, J. A. Jaszczak, and A. K. Geim, *Giant intrinsic carrier mobilities in graphene and its bilayer*, *Physical Review Letters* **100**, 016602 (2008).
- [56] K. I. Bolotin, K. J. Sikes, Z. Jiang, M. Klima, G. Fudenberg, J. Hone, P. Kim, and H. L. Stormer, *Ultrahigh electron mobility in suspended graphene*, *Solid State Communications* **146**, 351-355 (2008).
- [57] K. I. Bolotin, K. J. Sikes, J. Hone, H. L. Stormer, and P. Kim, *Temperature-dependent transport in suspended graphene*, *Physical Review Letters* **101**, 096802 (2008).
- [58] I. Meric, M. Y. Han, A. F. Young, B. Ozyilmaz, P. Kim, and K. L. Shepard, *Current saturation in zero-bandgap, top-gated graphene field-effect transistors*, *Nature Nanotechnology* **3**, 654-659 (2008).

- [59] R. S. Shishir and D. K. Ferry, *Velocity saturation in intrinsic graphene*, Journal of Physics Condensed Matter **21**, 344201 (2009).
- [60] F. Xia, T. Mueller, Y. M. Lin, A. Valdes-Garcia, and P. Avouris, *Ultrafast graphene photodetector*, Nature Nanotechnology **4**, 839-843 (2009).
- [61] R. R. Nair, P. Blake, A. N. Grigorenko, K. S. Novoselov, T. J. Booth, T. Stauber, N. M. R. Peres, and A. K. Geim, *Fine structure constant defines visual transparency of graphene*, Science **320**, 1308 (2008).
- [62] F. Wang, Y. Zhang, C. Tian, C. Girit, A. Zettl, M. Crommie, and Y. R. Shen, *Gate-variable optical transitions in graphene*, Science **320**, 206-209 (2008).
- [63] Z. Q. Li, E. A. Henriksen, Z. Jiang, Z. Hao, M. C. Martin, P. Kim, H. L. Stormer, and D. N. Basov, *Dirac charge dynamics in graphene by infrared spectroscopy*, Nature Nanotechnology **4**, 532 (2008).
- [64] T. Mueller, F. Xia, and P. Avouris, *Graphene photodetectors for high-speed optical communications*, Nature Photonics **4**, 297-301 (2010).
- [65] M. Liu, X. Yin, E. Ulin-Avila, B. Geng, T. Zentgraf, L. Ju, F. Wang, and X. Zhang, *A graphene-based broadband optical modulator*, Nature **474**, 64-67 (2011).
- [66] L. Yang, C.-H. Park, Y.-W. Son, M. L. Cohen, and S. G. Louie, *Quasiparticle energies and band gaps in graphene nanoribbons*, Physical Review Letters **99**, 186801 (2007).
- [67] M. Y. Han, Ouml, B. zyilmaz, Y. Zhang, and P. Kim, *Energy band-gap engineering of graphene nanoribbons*, Physical Review Letters **98**, 206805 (2007).
- [68] X. Li, X. Wang, L. Zhang, S. Lee, and H. Dai, *Chemically derived, ultrasmooth graphene nanoribbon semiconductors*, Science **319**, 1229-1232 (2008).

- [69] X. Wang, Y. Ouyang, X. Li, H. Wang, J. Guo, and H. Dai, *Room-temperature all-semiconducting sub-10-nm graphene nanoribbon field-effect transistors*, Physical Review Letters **100**, 206803 (2008).
- [70] L. Jiao, L. Zhang, X. Wang, G. Diankov, and H. Dai, *Narrow graphene nanoribbons from carbon nanotubes*, Nature **458**, 877-880 (2009).
- [71] L. Jiao, X. Wang, G. Diankov, H. Wang, and H. Dai, *Facile synthesis of high-quality graphene nanoribbons*, Nature Nanotechnology **5**, 321-325 (2010).
- [72] M. D. Stoller, S. Park, Y. Zhu, J. An, and R. S. Ruoff, *Graphene-based ultracapacitors*, Nano Letters **8**, 3498-3502 (2008).
- [73] C. Liu, Z. Yu, D. Neff, A. Zhamu, and B. Z. Jang, *Graphene-based supercapacitor with an ultrahigh energy density*, Nano Letters **10**, 4863-4868 (2010).
- [74] Y. Zhu, S. Murali, M. D. Stoller, K. J. Ganesh, W. Cai, P. J. Ferreira, A. Pirkle, R. M. Wallace, K. A. Cyhosh, M. Thommes, D. Su, E. A. Stach, and R. S. Ruoff, *Carbon-based supercapacitors produced by activation of graphene*, Science **332**, 1537-1541 (2011).
- [75] F. Schedin, A. K. Geim, S. V. Morozov, E. W. Hill, P. Blake, M. I. Katsnelson, and K. S. Novoselov, *Detection of individual gas molecules adsorbed on graphene*, Nature Materials **6**, 652-655 (2007).
- [76] M. Büttiker, *Absence of backscattering in the quantum Hall effect in multiprobe conductors*, Physical Review B **38**, 9375 (1988).
- [77] D. A. Abanin and L. S. Levitov, *Quantized transport in graphene p-n junctions in a magnetic field*, Science **317**, 641-643 (2007).

Chapter 2

Graphene-Based Device Fabrication

2.1 Mechanical exfoliation and optical identification of atomically thin films

All graphene pieces and thin hexagonal boron nitride (h-BN) flakes in this work were obtained via the “Scotch® tape method”, also known as “micromechanical cleavage” [1]. This technique is based on the fact that graphite layers are bonded to each other by weak Van der Waals forces, and hence such layers can be physically separated in a relatively easy way. The detailed steps of graphene exfoliation are illustrated in Fig. 2.1(a-d).

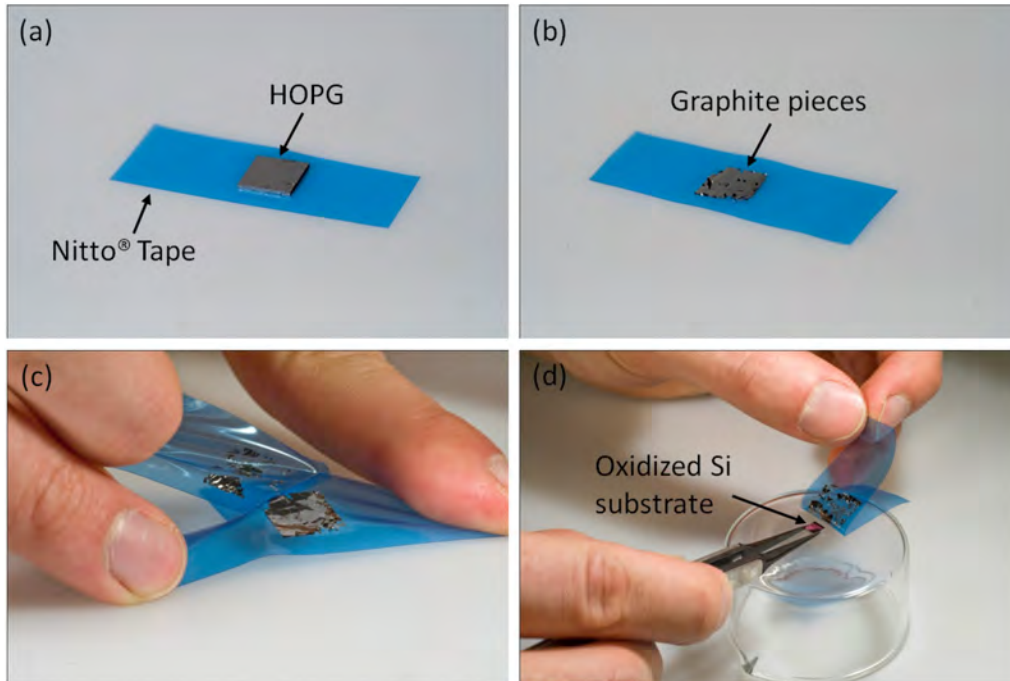


Figure 2.1: Procedure of graphene preparation via mechanical exfoliation. (a) Starting materials: highly oriented pyrolytic graphite (HOPG) (or natural graphite) and Nitto® tape. (b) Cleave the graphite crystal by pressing the tape on the graphite surface and then peeling the tape off, leaving relatively big and thick graphite pieces on the tape. (c) Fold and press the tape to make a tape-graphite-tape sandwich, and then peel apart the two ends of the tape; repeat this folding-pressing-peeling until thin shiny pieces of graphite nearly cover the tape. (d) An oxidized Si wafer with the oxide side down is placed on these graphite clusters. Press the Si chip with a finger or a soft rubber rod, and then peel the tape off with the help of tweezers.

The starting material for graphene deposition can be either highly oriented pyrolytic graphite (HOPG) or natural graphite. To ensure a high yield of graphene flakes with reasonable sizes (tens to hundreds of μm^2 , typically), the grain size of the source graphite has to be large enough (e.g. hundreds by hundreds of microns). Among many candidates, we found that grade “ZYA” HOPG from Advanced Ceramics and grade “extremely-large-flakes” natural graphite from NGS Naturgraphit GmbH consistently render the biggest as well as the cleanest graphene flakes.

The substrates for graphene deposition are oxidized silicon wafers. A 285-300 nm thick SiO_2 layer was grown on top of highly doped silicon by dry oxidation, which features a breakdown field of around 1 V/nm. The low-resistivity degenerate silicon substrate allows for global back-gating operation afterwards. We found it extremely important to make the substrates as clean as possible before graphene deposition. Our recipe involves soaking and rinsing (in organic solvents), sonication, as well as oxygen plasma treatment. We observed that warm NMP (N-Methyl-2-pyrrolidone, supplier: ALLRESIST GmbH) at a temperature between 55 and 60°C are very effective in removing photoresist/electron-beam resist or organic adhesive residues from the surface of silicon substrates. Compared with acetone, which is also widely used as a generic organic stripper, NMP bears such desirable properties as low volatility, low flammability, and relatively low toxicity. By ultrasonically cleaning the solvent, one may much more efficiently get rid of the hard-baked photoresist/electron-beam resist. However, sonication at excessively high power may result in the destruction of some fine metal structures defined on the substrate surface. Immediately prior to graphene deposition, already cleaned substrate chips are treated in an O_2 plasma chamber for a few minutes in

order to burn off the organic residue. To check the cleanliness of the substrates, we found the “dark-field” mode of an optical microscope useful.

The tape we have been employing to cleave the graphite crystal is type “SWT-10” from the company Nitto Denko (<http://www.nitto.com>). Compared with standard Scotch tape which is in use in some other research groups, the “Nitto tape” is found to leave minimal residue contamination on the surface of graphene or the silicon substrate, thanks to its adequate stiffness and adhesiveness.

After graphene deposition, the chips are cleaned in acetone and isopropanol at room temperature for 1-2 minute each, and then baked at 160°C on a hot plate for 4 minutes to drive off any solvent residue. At this point, these silicon substrates are ready for optical inspection.

With a commercial optical microscope (e.g. Nikon’s Eclipse®), single-layer graphene can be distinguished from bi- and multi-layer sheets based on thin film interference (see Fig. 2.2(a)). It is essential that these atomically thin graphite films are prepared on top of silicon wafers with a certain thickness of SiO₂. Thin graphene flakes are transparent enough (with an opacity $2.3 \pm 0.1\%$ when illuminated with visible light [2]) to add to an optical path, which alters their interference color with respect to an empty wafer. For a silicon wafer with 300 nm thick SiO₂ on top, single-layer graphene can already render sufficient optical contrast, making it possible for the human eye and brain to identify micron-sized graphene films among thicker graphite flakes scattered over the substrate surface (typically with an area of tens of mm²). It was found that the visibility of graphene depends strongly on both the thickness of the SiO₂ layer and the wavelength of the light source [3]. This observation can be explained by comparing the total reflectance

of the incident visible light in the presence and absence of a graphene film on the SiO₂/Si surface. This is illustrated in Fig. 2.3. For simplicity, we only consider the situation of normal incidence from air (with refractive index $\tilde{n}_0 = 1$) onto the trilayer structure. In most applications, this assumption is reasonable given the fact that the sum of the thickness of graphene film and SiO₂ layer (~ 300 nm in most cases) is far smaller than the depth of focus of the objective lenses (on the order of micrometer) of an optical microscope.

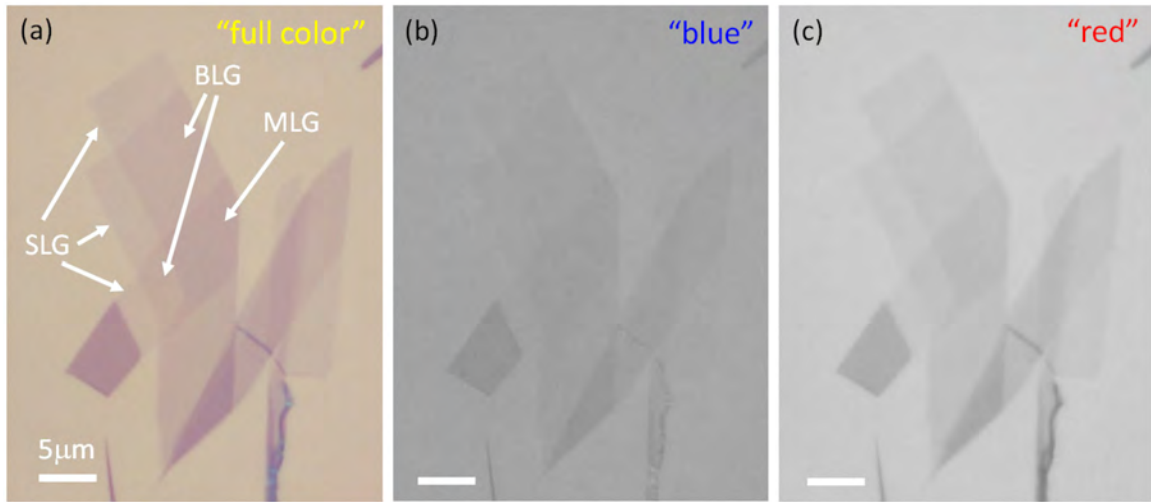


Figure 2.2: Full color optical image (a) of single-layer graphene (SLG), bi-layer “graphene” (BLG) and multi-layer graphite (MLG) flakes on ~ 300 nm thick SiO₂ illuminated with white light. Image (b) and (c) are obtained by extracting the “blue” and “red” components from the RGB indices array of pixels in (a), respectively.

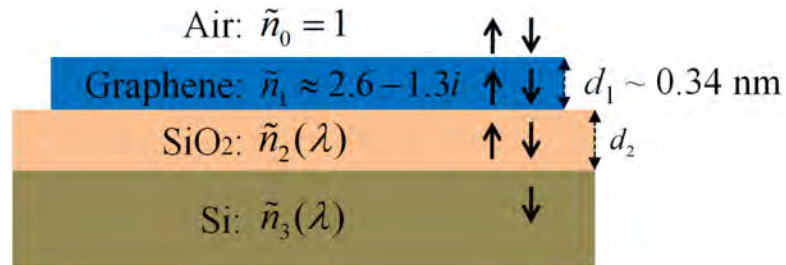


Figure 2.3: Geometry of the trilayer system composed of graphene, SiO₂ and Si.

We consider the limit of an infinitely thick silicon layer and assume that all media are homogeneous in the z -direction. As it has been reported in the literature [4], the complex index of refraction of silicon ($\tilde{n}_3 = n_3 - k_3i$) is a strong function of the wavelength λ in the visible range. The wavelength dependence of both the real part (refractive index, n_3) and the imaginary part (extinction coefficient, k_3) of \tilde{n}_3 are shown in Fig. 2.4(a). The imaginary part of the complex index of refraction of SiO₂ glass on top of Si vanishes within the visible spectrum, which implies that absorption is negligible when light travels perpendicularly through this layer. The real part of \tilde{n}_2 is precisely described by a multi-term Sellmeier equation [5], which is plotted as a function of wavelength λ in Fig. 2.4(b). It was already demonstrated that these $\tilde{n}_2(\lambda)$ and $\tilde{n}_3(\lambda)$ can accurately describe the interference colors seen on oxidized silicon wafers [6]. In our calculation, (single-layer) graphene with a thickness 0.34 nm [7] is assumed to have the same complex index of refraction as bulk graphite. This has proved to be a reasonable approximation [2] because the interlayer hopping energy in graphite is so low (~ 0.3 eV) that in a system of stacked graphene layers, the in-plane electromagnetic response dominates the optical transition process in the visible range, i.e. the optical response out of a graphene plane is negligible in this case. The complex index of refraction of bulk graphite (also graphene) was taken to be independent of λ ($\tilde{n}_1 \approx 2.6 - 1.3i$) [3] within the visible spectrum. This yields good agreement with our experimental observations, even although M. Bruna et al. [8] argued that the extinction coefficient of graphite should be treated as proportional to λ in the visible range for more precise predictions.

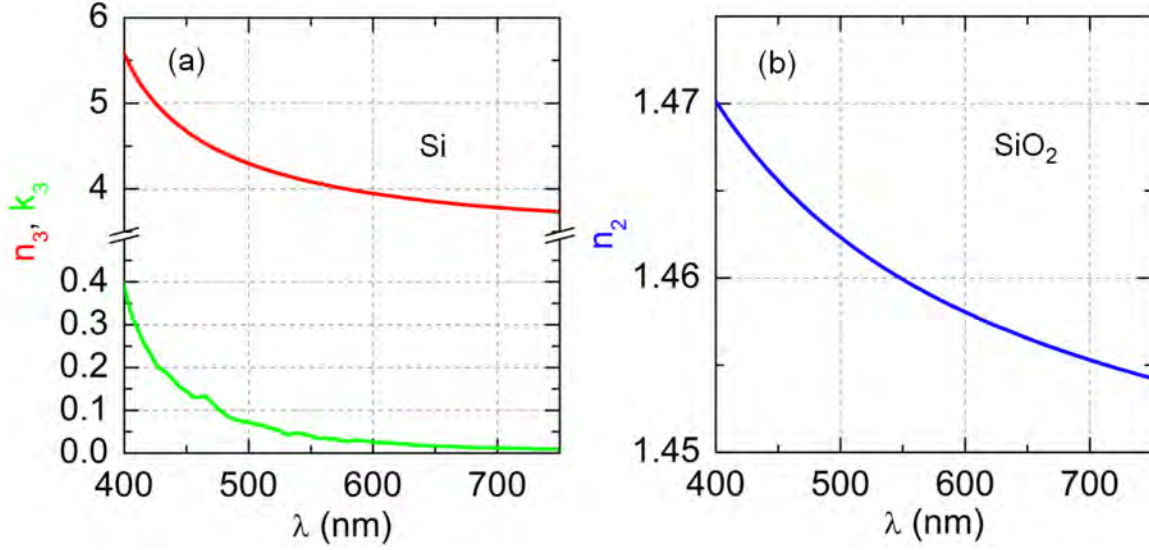


Figure 2.4: Real (refractive index, n) and imaginary (extinction coefficient, k) part of the complex index of refraction of Si (a) and SiO_2 (b) in the visible range. Here, $k_2 \equiv 0$ (interpolated from literature [4] and [5]).

On the basis of the Fresnel equations, we can define the relative indices of refraction for the three interfaces (air-graphene, graphene- SiO_2 , and SiO_2 -Si) in the system of Fig. 2.3:

$$r_1 = \frac{\tilde{n}_0 - \tilde{n}_1}{\tilde{n}_0 + \tilde{n}_1}, \quad r_2 = \frac{\tilde{n}_1 - \tilde{n}_2}{\tilde{n}_1 + \tilde{n}_2}, \quad r_3 = \frac{\tilde{n}_2 - \tilde{n}_3}{\tilde{n}_2 + \tilde{n}_3}. \quad (2.1)$$

Transmission through graphene and SiO_2 layers causes changes in the optical path.

The corresponding phase shifts are:

$$\Phi_1 = \frac{2\pi\tilde{n}_1d_1}{\lambda}, \quad \Phi_2 = \frac{2\pi\tilde{n}_2d_2}{\lambda}. \quad (2.2)$$

At this stage, the total reflectance (R) from this trilayer structure can be readily calculated [9]:

$$R(d_2, \lambda) = \left| \frac{r_1 e^{i(\Phi_1 + \Phi_2)} + r_2 e^{-i(\Phi_1 - \Phi_2)} + r_3 e^{-i(\Phi_1 + \Phi_2)} + r_1 r_2 r_3 e^{i(\Phi_1 - \Phi_2)}}{e^{i(\Phi_1 + \Phi_2)} + r_1 r_2 e^{-i(\Phi_1 - \Phi_2)} + r_1 r_3 e^{-i(\Phi_1 + \Phi_2)} + r_2 r_3 e^{i(\Phi_1 - \Phi_2)}} \right|^2. \quad (2.3)$$

The optical contrast C is defined as the difference in the total reflectance in the presence ($\tilde{n}_1 \neq 1$) and absence ($\tilde{n}_1 = \tilde{n}_0 = 1$) of graphene,

$$C = \frac{R(\text{no_graphene}) - R(\text{with_graphene})}{R(\text{no_graphene})}. \quad (2.4)$$

According to this definition, a positive contrast value means that the graphene film would appear darker than the surrounding substrate surface.

A color plot generated by Matlab® for the expected contrast as a function of SiO₂ layer thickness and incident visible light wavelength is shown in Fig. 2.5. By studying this plot, one may notice: (1) within the given range, the contrast values are nearly always positive, meaning (single-layer) graphene appears almost always darker than the exposed substrate surface; (2) if illuminated with light of appropriate wavelengths, graphene films can be made visible to the human eye, except for a SiO₂ thickness of around 150 nm or below 25 nm. In graphene research, silicon substrates with a ~300 nm thick SiO₂ layer on top are most commonly used. When illuminated with yellow light ($\lambda \approx 600$ nm), graphene on this type of substrate has a fairly high contrast ($C > 0.1$) that makes the search of this atomically thin material possible.

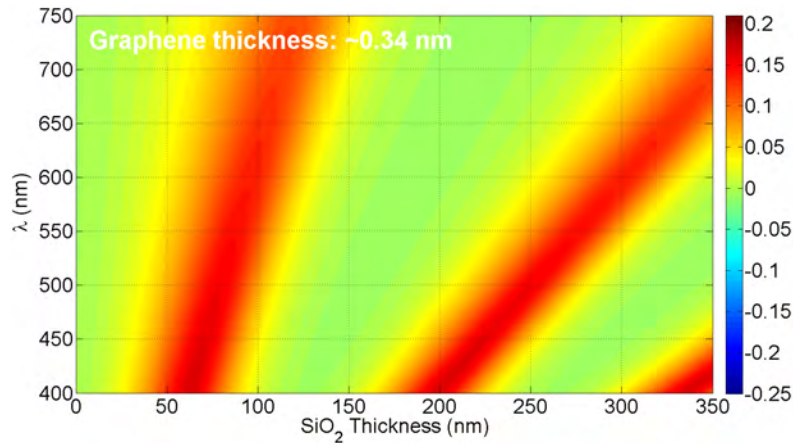


Figure 2.5: Color plot of (single-layer) graphene's expected contrast as a function of wavelength λ and SiO₂ thickness according to Eq. 2.4.

In practice, however, we do not always need the involvement of expensive narrow-band optical filters to improve the visibility of graphene. One may simply take a full-color photograph (without contrast enhancement or image manipulation at this stage) for the graphene candidate on ~ 300 nm thick SiO_2 with white light illumination, and then extract the red component from the RGB indices array of the pixels to form a new “contrast-enhanced” image for the same graphene flake. This task can be accomplished with commercially available image analysis software. An example is demonstrated in Fig. 2.2(b-c). On the basis of the experimental observations that the opacity of few-layer graphene linearly increases with the number of layers [2], we are able to utilize the “RGB extraction” method mentioned above to precisely identify single-, bi- and even triple-layer graphene on oxidized silicon wafers. The identification results have been verified by subsequent AFM topography and/or magneto-transport measurements. Note, however, that this method is no longer applicable on thicker graphite pieces, since they tend to become totally opaque in the visible range due to the existence of free electrons in the layered structure.

Of course, equations 2.1-2.4 can be extended to the contrast calculation for other thin film systems, e.g. nanometer thick hexagonal boron nitride (h-BN) on oxidized Si substrates.

Fig. 2.6(a) shows the schematic of h-BN crystal structure, which features an AA' stacking along the c -axis with 0.33-0.34 nm interlayer spacing. The lattice mismatch between graphene and layered h-BN is less than 2% [10]; however, the two atoms in the unit cell of the h-BN crystal are chemically inequivalent. The significant difference in the electronegativities between onsite atoms results in an energy gap as large as ~ 6 eV [11].

This makes layered h-BN crystal electrically insulating and essentially transparent in the visible regime. Within one atomic layer of h-BN, boron and nitrogen atoms are bonded with strong, partially ionic, sp^2 -hybridized bonds. In the vertical direction it is mainly van der Waals force that binds these layers to form a highly anisotropic three-dimensional crystal. This in principle makes it possible to isolate atomically thin h-BN sheets from bulk crystal with the same mechanical exfoliation method as described above. A few-nanometer thick h-BN flake deposited on an oxidized Si wafer is shown in Fig. 2.6(b). Note, however, that due to the existence of the slightly ionic bonding out of the plane, h-BN crystals are harder and more brittle than HOPG or natural graphite, and it is also more difficult to obtain extremely thin h-BN sheets (comprising of one or only a few atomic layers) with homogeneous thickness via micromechanical cleavage.

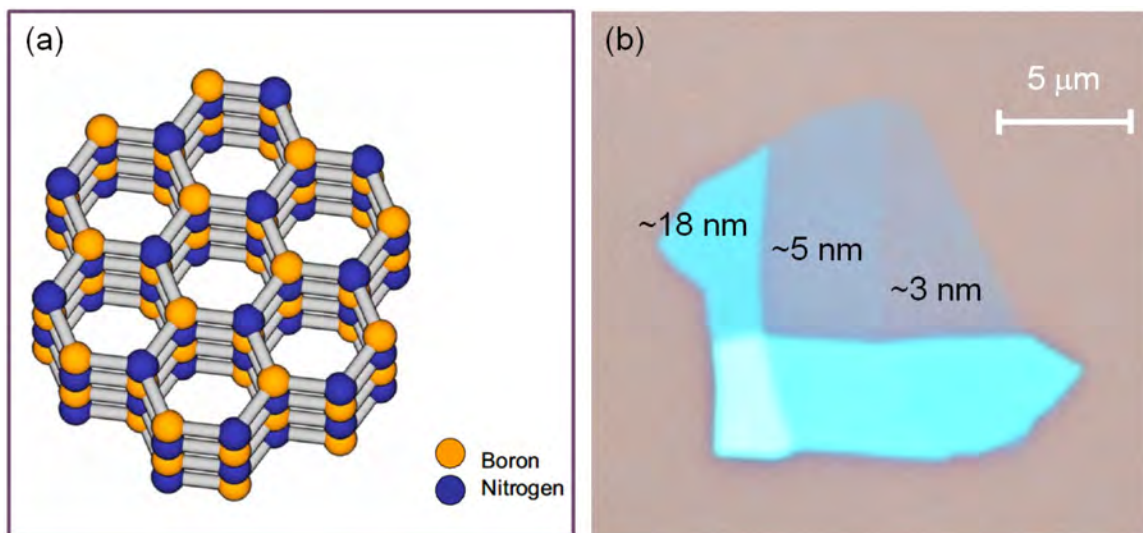


Figure 2.6: Schematic of an AA'-stacked hexagonal boron nitride (h-BN) crystal (a), and optical image of a thin h-BN crystallite (with local thicknesses indicated) on an oxidized Si wafer (b).

In this work, few-nanometer thick h-BN films were isolated based on their optical contrast on SiO_2 in order to use them as a top-gate dielectric in graphene electronic devices. As was already mentioned, we can readily utilize equations 2.1-2.5 to predict the

contrast of a thin h-BN sheet lying on an oxidized Si wafer, simply by replacing $\tilde{n}_1 \approx 2.6 - 1.3i$ with $\tilde{n}_1 \approx 2.2$ [12], which is the measured complex index of refraction of h-BN crystal in the visible range (note that here \tilde{n}_1 is independent of wavelength λ , and the extinction coefficient vanishes in h-BN films). During sample preparation, we found that when illuminated with white light, an h-BN sheet with a thickness of around 2.5 nm shows a contrast rather similar to that of (single-layer) graphene in the optical microscope (e.g. Nikon Eclipse®). However, the color plot of the expected h-BN contrast for that particular thickness (i.e. 2.5 nm) reveals some very different features, as is illustrated in Fig. 2.7. For the purpose of comparison, the same scale bar as that in Fig. 2.5 is employed here. One may immediately notice that on 300 nm thick SiO₂, h-BN's contrast will alter sign when the illumination goes from blue light to red, denoting that the thin h-BN sheet on top of SiO₂ may appear either brighter or darker than the surrounding substrate surface depending on illumination wavelength. Since within this work, the thickness of SiO₂ layer on Si substrates is always close to 300 nm, it is worthwhile to generate another color plot for h-BN's expected contrast as a function of h-BN thickness and incident (visible) light wavelength, as is shown in Fig. 2.8. Generally, at a given wavelength λ , the contrast of h-BN sheets changes monotonically with its thickness (except for $\lambda \approx 600$ nm, where the contrast changes sign). Based on this result, we are able to estimate the local thickness of an h-BN flake by extracting the RGB information from the specimen's full-color image, and for a piece within 10 nm thick, the error is generally less than 1 nm. Fig. 2.9 demonstrates the "contrast-enhanced" pictures for a few h-BN flakes on oxidized Si wafers. The sheets' actual thicknesses obtained from AFM topography measurements are

also shown for reference. Note, however, that organic residue on the surface of the atomically thin films or SiO₂ substrate may significantly affect the contrast reading.

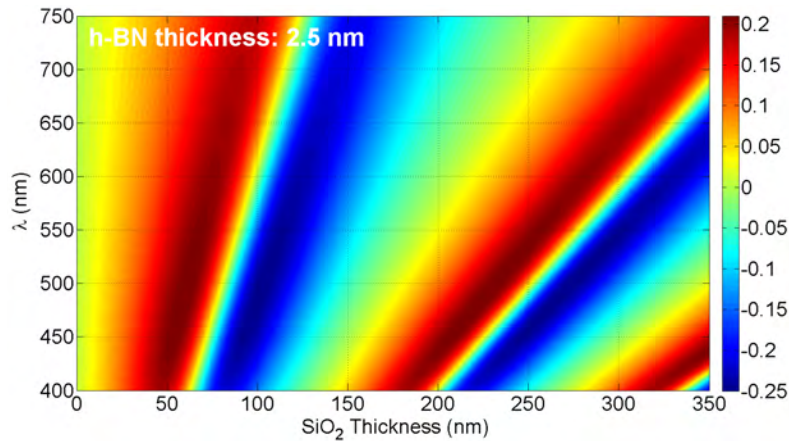


Figure 2.7: Calculated contrast of 2.5 nm thick h-BN as a function of wavelength and SiO₂ thickness. Here, an approximate value for $\tilde{n}_1 \approx 2.2$ (complex index of refraction of h-BN in visible range according to literature [12]) is inserted in equations 2.1-2.5. For comparison, the color scale on the right is made identical to that in Figure 2.5.

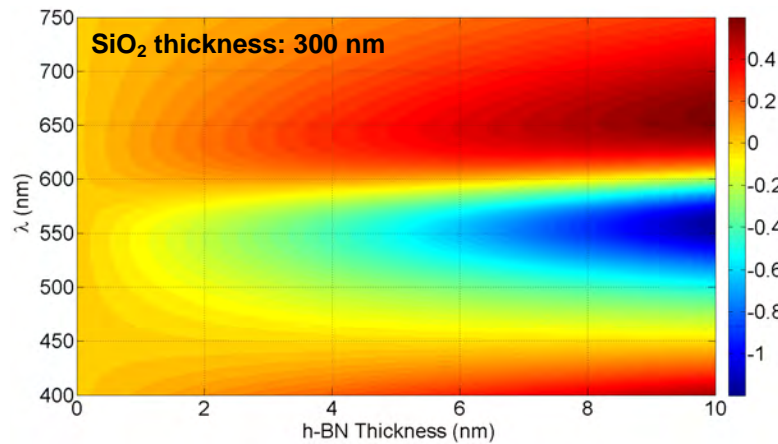


Figure 2.8: Expected contrast of h-BN on 300 nm thick SiO₂ as a function of wavelength and h-BN thickness.

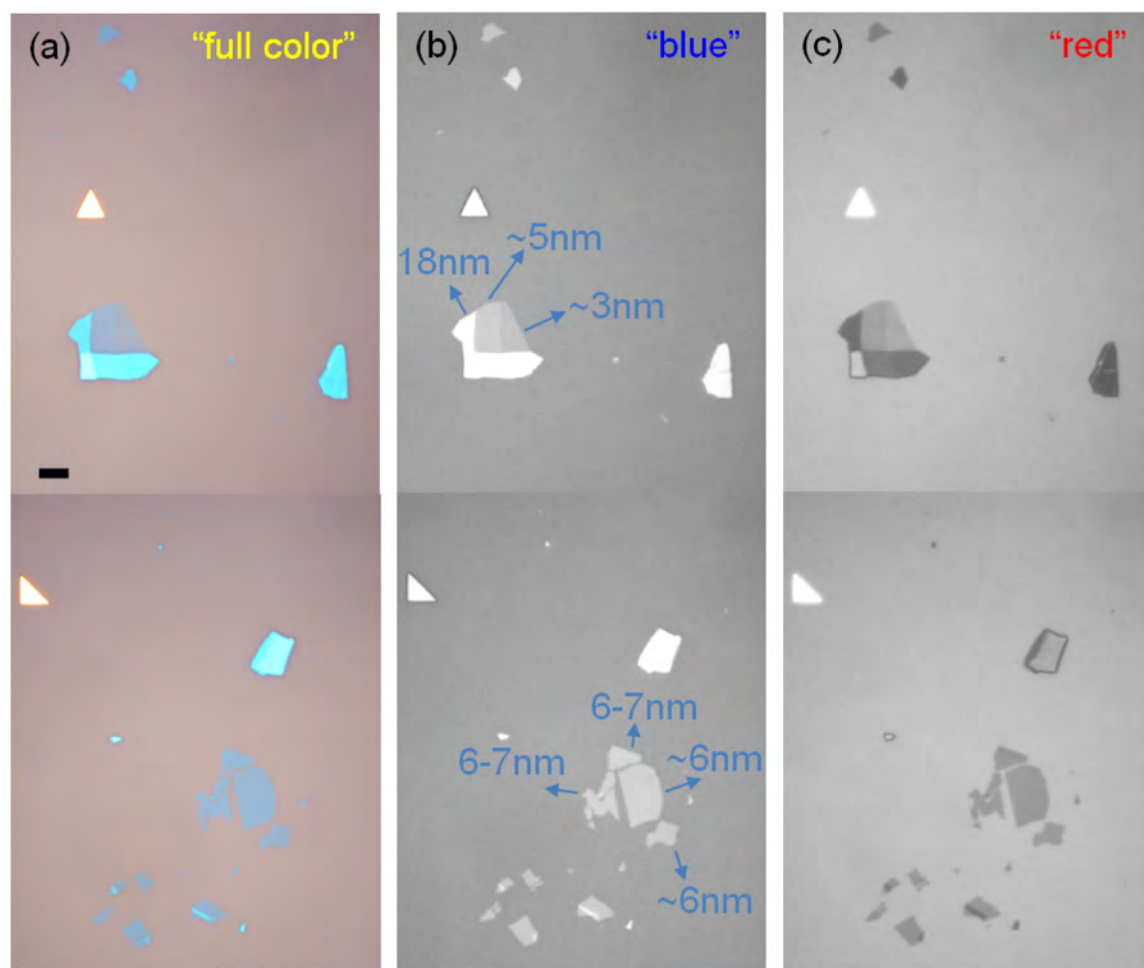


Figure 2.9: (a) Full color image of a few h-BN crystallites on ~ 300 nm SiO_2 illuminated with white light. Contrast-enhanced pictures in (b) and (c) are obtained by extracting the "blue" and "red" components from the RGB array of (a), respectively. Scale bar in (a) = $5 \mu\text{m}$.

2.2 Definition and deposition of metal contacts

After a graphene sheet with appropriate shape (i.e. close to a rectangular) and size (typically a few microns by a few microns) is isolated and identified, we need to make electrodes on it. Electron beam lithography (EBL) is a very powerful tool in the definition of micrometer-sized electrical contacts. The fabrication procedure is schematically illustrated in Fig. 2.10. It comprises the following steps: (1) electron-beam (e-beam) resist spin-coating and e-beam exposure, (2) development, (3) metallization, and (4) lift-off.

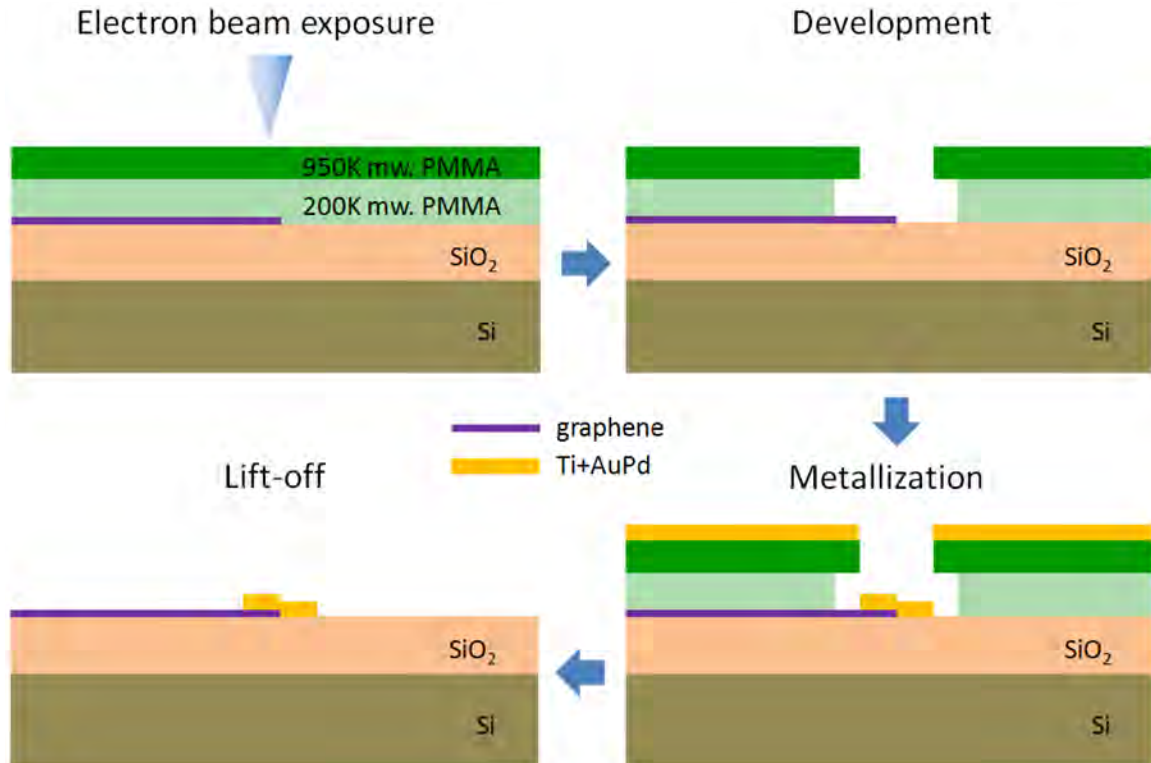


Figure 2.10: Schematic illustration of the fabrication procedure for electrical contacts. In the first step, a double-layer PMMA e-beam resist is spin-coated on the Si substrate, and an electron beam pattern generator writes the contacts into the resist with a highly energetic focused electron beam. During development, the exposed portions of PMMA are dissolved in a MIBK/IPA developer. Then metal films are deposited on top of the sample with thermal evaporation. Finally, the remaining resist is lifted off in warm NMP.

First of all, the substrate surface with graphene on top is coated with a double-layer of poly(methyl methacrylate) (PMMA) e-beam resist. The coated chip is baked on a convection surface to remove the chlorobenzene solvent from the resist. The bottom layer of PMMA (200k mw.) is more sensitive to the electron bombardment than the top layer (950k mw.). This results in an “undercut” in the resist profile after development. It greatly improves the lift-off procedure since resist strippers can laterally attack the resist. During electron beam exposure, an electron beam pattern generator writes the CAD device design into the e-beam resist by breaking the bonds in the polymer with accelerated electrons (usually with tens of keV kinetic energy). The “exposed” parts of the resist become soluble in a developer (PMMA is a positive resist). Note, that the electron dose has to be optimized prior to writing, as overexposure may downgrade the contact profile or even damage the graphene film, while too low a dose (underexposure) will leave resist residue on the contact area after development (this tends to degrade the contact performance). The developer we have been using is methyl isobutyl ketone (MIBK) 1:3 mixed with isopropanol (IPA), and IPA is the stopper. It is necessary to constantly stir the chip in the developer for a few minutes to ensure a thorough development. After this, the exposed polymer is dissolved while the unexposed parts remain essentially unaffected. They act as a mask during the subsequent metal evaporation. Throughout this work, metal contacts are deposited with thermal evaporation in a high-vacuum chamber (Leybold Univex®) with a deposition rate of 0.1-2 Å/sec and at a background pressure on the order of 10^{-7} mbar. We found that a clean background environment is critical to the formation of ohmic low-resistance contacts. After the deposition of a relatively thin adhesion layer (e.g. 1-5 nm Ti, or 3-6 nm Cr),

tens of nanometers of Au or AuPd are evaporated in the same chamber to avoid oxidation of the adhesion-promoting layer of Ti or Cr. In the lift-off step, deposited metals lying on top of the unexposed PMMA (mask) are removed from the chip by dissolving the polymer in warm NMP (at 55-60°C) for around 2 hours (followed by acetone and IPA rinsing and N₂ gas blow-drying). Although in graphene research gold is more commonly used as the conducting material for electrical contacts, the author prefers the alloy of gold and palladium (with 60% Au). Compared with Au, deposited AuPd films generally feature a much smaller grain size (at the same deposition rate), as is clearly demonstrated by the SEM micrograph in Fig. 2.11(a). These contacts work better at high current densities or high temperatures. Fig. 2.11(b) shows the optical image of a meander-shaped metallic resistor made of deposited AuPd with a cross-section of 200 nm × 16 nm. At ~1.7 K, this device is capable of continuously and stably working for hours with a permanent DC current as large as ~2.2 mA. Fine-grained AuPd contacts are also less subject to material migration when being treated at relatively high temperatures. Fig. 2.11(c) displays the SEM image of broken Au contacts of a graphene device after being annealed (the working principle and effects induced by annealing will be discussed in Chapter 3) at 350°C for 3 hours in flowing “forming gas” (5% H₂ + 95% N₂). The AuPd electrodes on the reference sample with identical contact design remained intact after the same thermal treatment, as is illustrated in Fig. 2.11(d).

After lift-off and annealing, the sample is glued to a 24-pin chip carrier with highly conductive silver paste. It is now ready for ultrasonic wire bonding. The sonication power as well as bonding force has to be adequate in order not to break the thin SiO₂ layer

between graphene and the highly doped Si substrate; otherwise, the device may suffer from a (back) gate leakage later on.

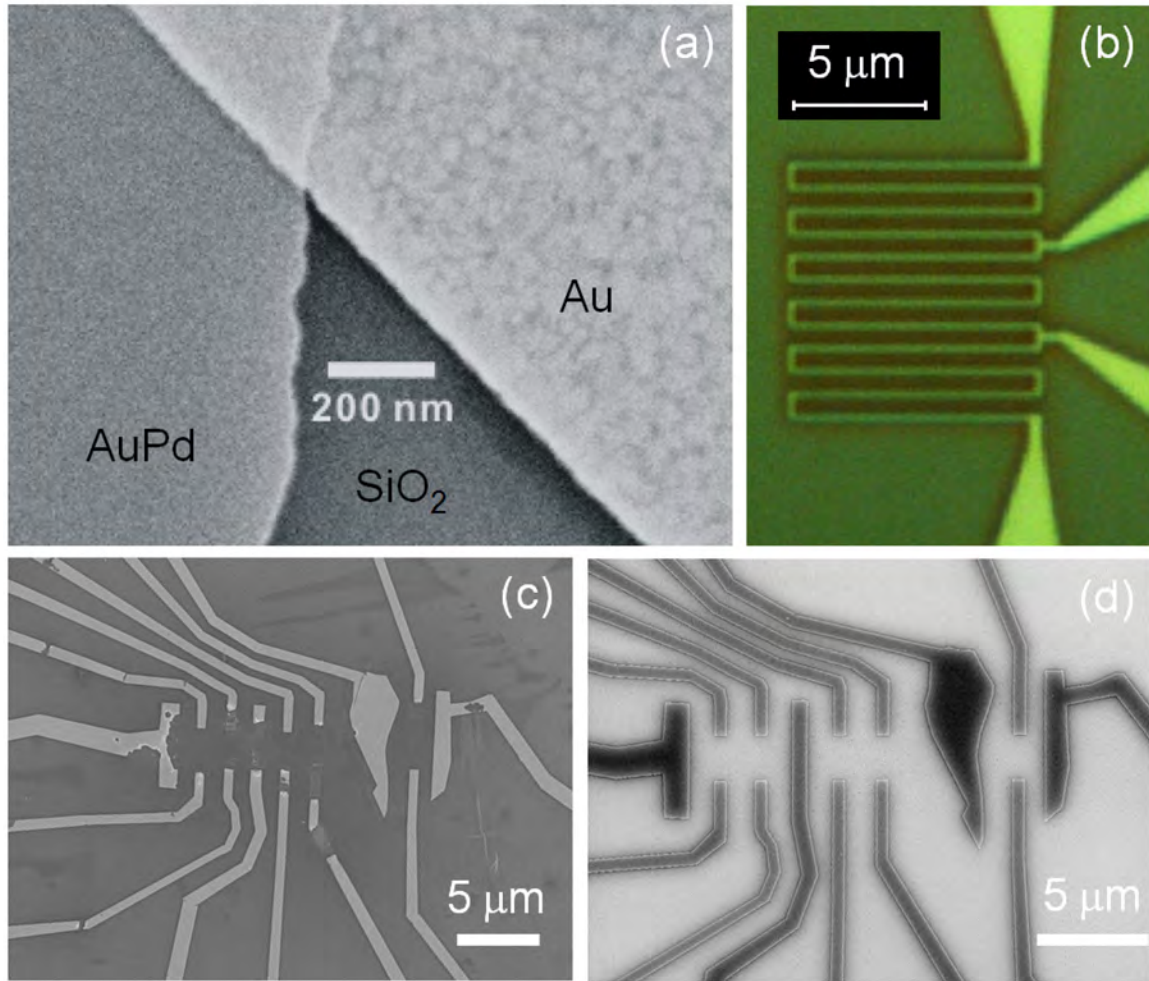


Figure 2.11: (a) SEM image of deposited Au and AuPd films on an oxidized Si wafer. (b) Optical micrograph of a meander-shaped AuPd resistor featuring a cross-section of $\sim 200 \times 16 \text{ nm}^2$ and $\sim 20 \text{ k}\Omega$ total resistance at room temperature. (c-d) Broken Au electrodes (c) and intact AuPd leads (d) after being treated in flowing forming gas at 350°C for 3 hours.

2.3 Preparation of top-gate dielectric

Degenerately doped, highly conductive Si substrates have been commonly employed as the global back-gate ever since the very first field effect measurement on graphene by Novoselov *et al.* in 2004 [1]. In the simplest graphene field effect transistors (GFET), global control of carrier type and density relies solely on the electrical field perpendicular to the graphene sheet applied by the single Si (back-) gate. However, from both scientific and technological point of view, fabrication of more complex graphene devices, such as graphene *p-n* junctions, is of great necessity and significance. The introduction of local top-gates enables the realization of in-plane bipolar graphene devices [13]. Electric fields applied by a global back-gate and a local top-gate render independent control over the carrier type and density in two adjacent regions of the graphene sheet. We notice that appropriate preparation of the top-gate dielectric is crucial to the quality and functionality of a dual-gated graphene device. We have systematically evaluated several methods for the creation of a suitable top-gate dielectric. These approaches will be discussed in the following sections.

2.3.1 Thermal Evaporation of SiO_x

Amorphous SiO_x ($x = 1-2$) can be thermally evaporated (through sublimation) as the top-gate dielectric with a dielectric constant slightly below 4 (3.6-3.9 in our case). The deposited insulating layer can either be patterned or not. The corresponding final device structures are schematically illustrated in Fig. 2.12.

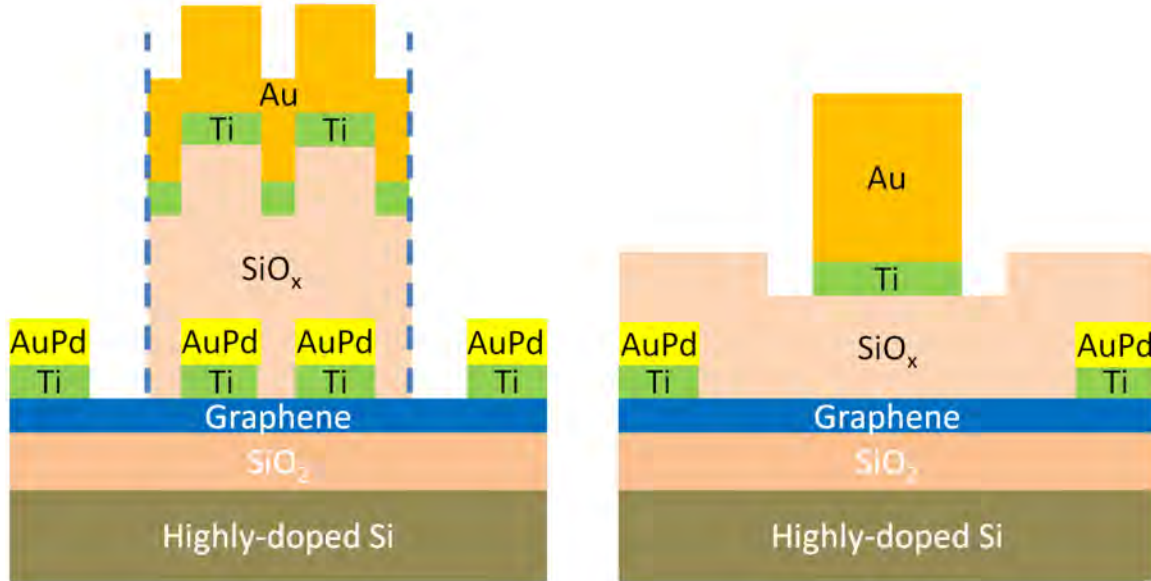


Figure 2.12: Cross-section of a dual-gated graphene device with patterned (left) or unpatterned (right) top-gate dielectric (thermally evaporated SiO_x in this case).

In the patterned case (Fig. 2.12(a)), the area on graphene to be covered by the top-gate dielectric is defined by electron-beam lithography after the formation of electrical contacts. SiO_x and top-gate metals are then deposited subsequently, if possible during the same evacuation sequence of the vacuum chamber in order to avoid contamination due to exposure to air. After lift-off, the chip can be annealed in flowing forming gas at elevated temperatures (typically 200-350°C) to remove resist residues from the exposed parts of graphene.

By using the shadow mask technique, one can also cover the whole top surface of graphene with SiO_x without patterning an opening in the resist (Fig. 2.12(b)). Before evaporation of the dielectric, a metallic foil with a small hole at the center is carefully placed over the active area of the graphene device, such that graphene gets exposed to the evaporation source while all the metallic bond-pads are masked. Electron beam

lithography is then employed after deposition of SiO_x to define the metallic gate area itself. Hydrogen annealing is in this case not necessary.

We observe that graphene devices with top-gate dielectric prepared as described above consistently show a rather low carrier mobility, i.e. always below $3000 \text{ cm}^2/\text{Vs}$ at a charge density $n \approx 2 \times 10^{12} \text{ cm}^{-2}$ at room temperature, regardless of the charge carrier type. At low temperatures (e.g. 4.2 K) and in a high external magnetic field (e.g. 14 Tesla), graphene's characteristic quantum Hall plateaus [14, 15] could hardly be seen except those at filling factors ± 2 . We attribute the degradation of graphene's electronic quality in these devices mainly to the increase in carrier scattering caused by the deposited SiO_x .

2.3.2 Metallic Air Bridge

To avoid the “physical” contact between the top-gate stacks and the graphene sheet, metallic air bridges can be introduced in which air or vacuum serves as the dielectric medium.

Our fabrication procedure for a suspended air bridge is schematically illustrated in Fig. 2.13. The e-beam resist for this purpose consists of three layers. The resist most sensitive to electron exposure (e.g. MMA, supplier: ALLRESIST GmbH) is located in the middle. At the bottom the least sensitive resist (e.g. 950k mw. PMMA) is deposited. We use 200k mw. PMMA for the top-most layer to define the shape of the suspended part of the bridge. The success of the fabrication largely relies on the precise electron dose control for both the suspended and the substrate-supported portions of the bridge structure. We need high electron dose to create windows through all three resist layers for the posts. They serve as electrical leads contacting the suspended structure. A lower

electron dose is applied to the suspended part, such that only the polymer bonds in the top two layers of the resist are broken. Those in the bottom layer remain nearly intact. After development in MIBK:IPA mixture (1:3), the remaining bottom layer of PMMA on top of graphene acts as a temporary support on which the metal bridge is deposited. During lift-off, all resists are removed by warm NMP, leaving a suspended metallic bridge connected to the top-gate electrodes. Note that metal evaporations at $\pm 45^\circ$ may be necessary to fully cover the steps induced by the supporting bottom-layer resist and to ensure a good contact between the bridge and the posts, especially when the spacing between the graphene sheet and the suspended structure is fairly large, i.e. above 100 nm.

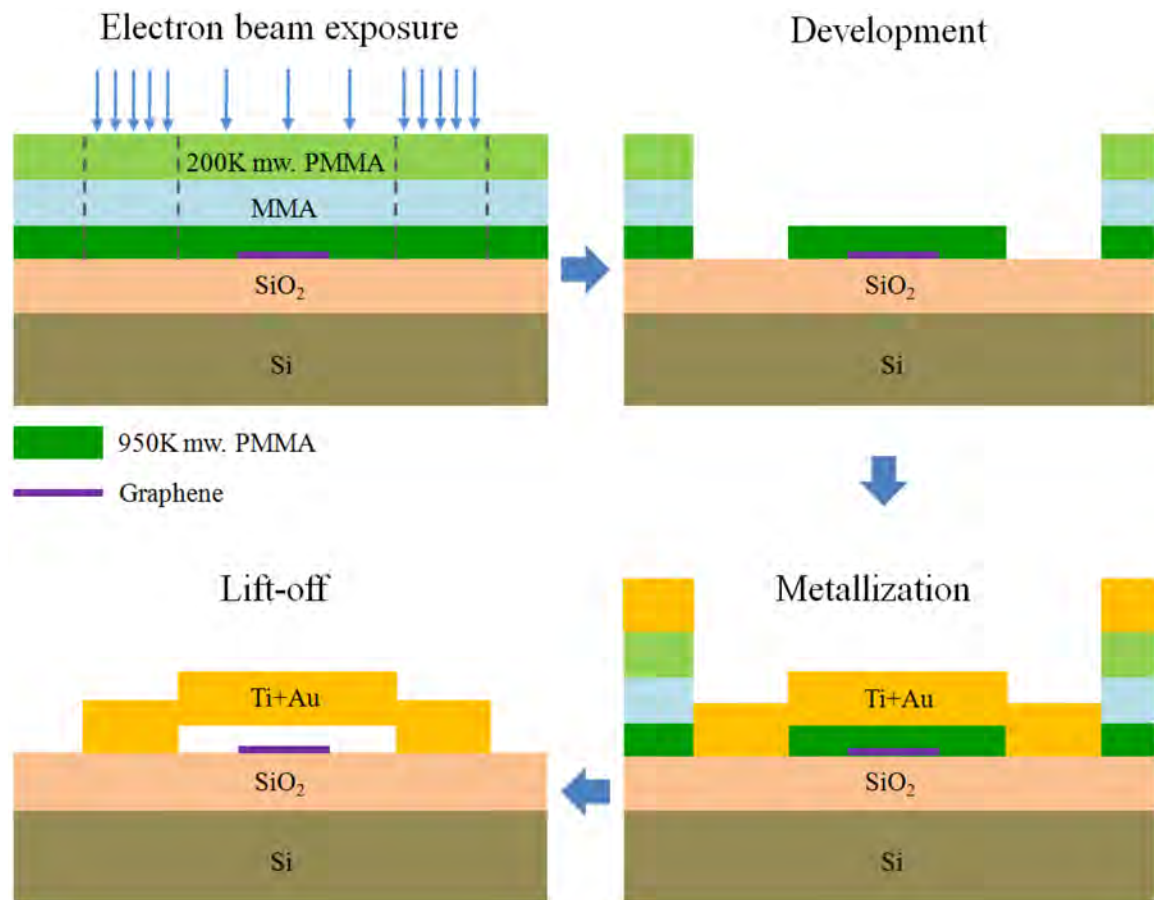


Figure 2.13: Schematic illustration of the air-bridge fabrication process. It consists of four steps: electron beam lithography with two different exposure doses, development, metallization, and lift-off.

The SEM images of a few finished air bridges on an oxidized Si wafer are shown in Fig. 2.14(a). The overall yield for such suspended structures is around 50%. Bridges with a span longer than a few micrometers can easily collapse during lift-off. An example is displayed in Fig. 2.14(b). AFM topography shows that the thickness of the suspended top-gate is spatially inhomogeneous in general. This reflects the difficulty in the local electron dose control during exposure. The problem may be alleviated by introducing a flat spacer layer on top of graphene prior to bridge structuring. The spacer is removed after the metal bridge is deposited [16, 17]. This, however, requires one more e-beam lithography step.

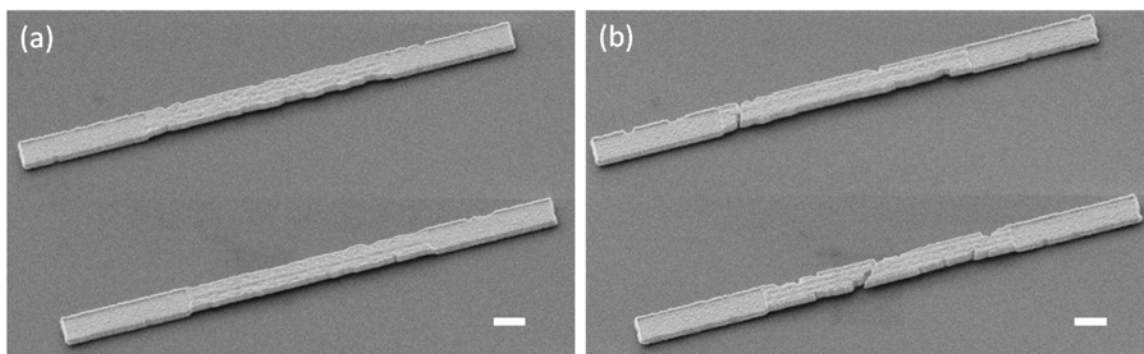


Figure 2.14: SEM micrographs of suspended (a) and collapsed (b) air bridges after lift-off. Note that they were fabricated on the same Si wafer. Scale bar in both pictures = 1 μm .

2.3.3 Atomic Layer Deposition

The main merits of atomic layer deposition (ALD) technique are the precise control over the thickness of the deposited materials, the possibility of growing densely packed high- κ dielectrics and the uniform coating of complex 3D geometries. In graphene research, ALD growth of Al_2O_3 [13, 18-20] and HfO_2 [21, 22] dielectrics has been frequently used and reported.

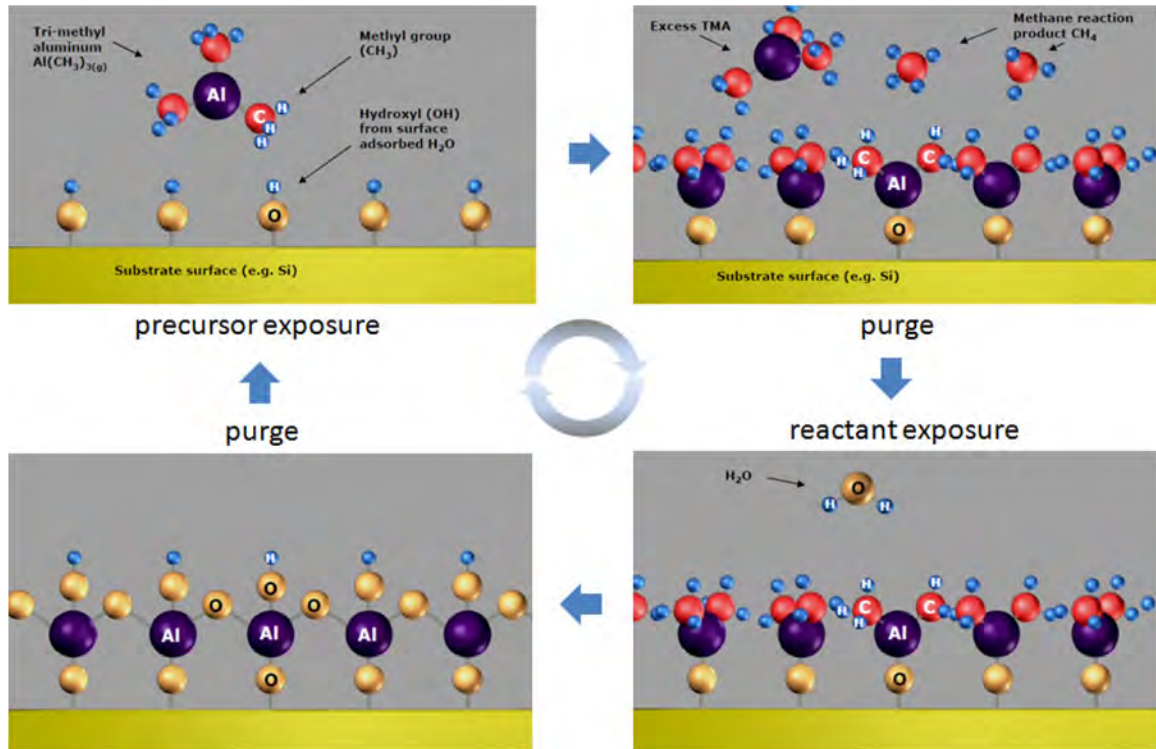


Figure 2.15: Four steps forming one reaction cycle in ALD (adapted from literature [23]): self-terminating precursor (e.g. trimethyl aluminum, TMA) exposure, purge of excessive precursor and reaction byproduct (e.g. CH₄), self-terminating reactant (e.g. H₂O) exposure, and purge of excessive reactant as well as reaction byproduct (again CH₄).

The working principle for growing an Al₂O₃ film on Si substrate with ALD is illustrated schematically in Fig. 2.15. Essentially, atomic layer deposition consists of four steps: (1) precursor exposure, in which a precursor (e.g. trimethyl aluminum, TMA) gas is pulsed into the ALD chamber and reacts with the chemically active groups (e.g. –OH) on the substrate surface in a self-terminating way until the surface is passivated with a single layer of chemisorbed precursor species; (2) purging of precursor and reaction byproduct, in which the excessive precursor is pumped away from the chamber together with the reaction byproduct (e.g. methane); (3) reactant exposure again in self-limiting way, in which an oxidant or reagent (e.g. H₂O vapor) is pulsed into the chamber and chemically adsorbed only on the sites where precursor is present, activating the surface

again by providing chemically active surface groups for the subsequent reaction with precursor; (4) purging of excessive reactant as well as reaction byproducts. Steps (1)-(4) make up a *reaction cycle*, in which step (1) and (3) are often referred to as *half reactions* of an ALD reaction cycle [24]. By repeating these cycles, dielectric oxide films can be grown atomic layer by atomic layer with a precise thickness control and a high degree of uniformity. The Al₂O₃ growth rate based on TMA and H₂O is usually about 0.1 nm/cycle in our machine (model “Savannah” from Cambridge NanoTech Inc.).

Due to the lack of chemically active dangling groups on “defect-free” clean graphene, the ALD precursor is not able to nucleate on top of pristine graphite sheets (except at the grain boundaries) [18]. Therefore, the graphene surface has to be functionalized prior to dielectric growth with ALD. Various surface treatment methods have been proposed, including carboxylate-terminated perylene coating [18], hydrogen silsesquioxane (HSQ) coating [21, 22], NO₂ functionalization [13, 19], ozone functionalization [20], etc. The author of the thesis, however, prefers to fulfill this goal by introducing a very thin layer of oxidized aluminum between graphene and the dielectric (to be grown with ALD). This is based on the observation that compared to other materials deposited Al apparently brings minimal negative effects to the electronic quality of graphene. The process begins with thermal evaporation of around 1 nm thick Al. The deposited material tends to form clusters on graphene (or graphite) surface (Fig. 2.16), which immediately oxidizes when exposed to air. To ensure a full coverage of the graphene surface with oxidized Al, this evaporation and oxidation procedure is repeated once. The resulted thin alumina layer acts as nucleation media for subsequent ALD. The ALD starts with pulsing of H₂O vapor.

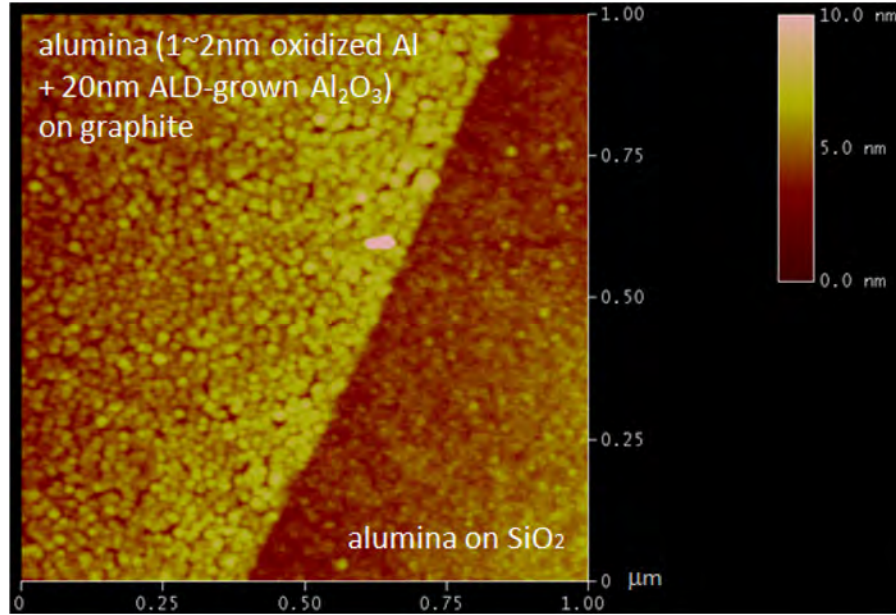


Figure 2.16: AFM image of alumina on graphite and SiO₂. A very thin (~1 nm) layer of Al was thermally evaporated onto graphite as well as SiO₂ surface and then oxidized by exposure to air, followed by ALD growth of 20 nm thick Al₂O₃. Alumina on graphite shows a mean roughness of ~0.52 nm, in contrast to ~0.33 nm on SiO₂.

As has been briefly described in section 2.3.1, a patterned top-gate dielectric may allow hydrogen annealing of the sample after lift-off. This proves to be very effective in removing the resist residues and hence enhancing device quality. The same practice has been carried out with the ALD technique, in which Al evaporation/oxidation, ALD growth of Al₂O₃, and metal top gate deposition are done in a consecutive way after a window in the PMMA resist is defined via electron beam lithography. The subsequent lift-off becomes fairly challenging, though, as the side walls of the e-beam resist are nearly fully covered by the ALD-grown alumina. To achieve a thorough stripping of the resist, a few tricks have been implemented: (1) the ALD has to be done at low temperatures (and with much longer precursor and reactant pulses), i.e. slightly above 100°C, such that no resist hard-baking may take place; (2) before immersing the chip in warm remover, a few scratches are intentionally made on the chip surface with a needle.

The needle scratches through the deposited materials and resist layers down to the substrate surface, resulting in a much higher efficiency in resist removal; (3) pulsed sonication is applied during lift-off to more effectively dislodge the resist. Fig. 2.17 shows the optical and SEM images of some test structures prepared with this recipe. Although the yield for successful lift-off appears acceptable, wire bonding has to be very carefully performed on real devices to avoid possible “peel-off” of the bond-pads from ALD-grown Al_2O_3 .

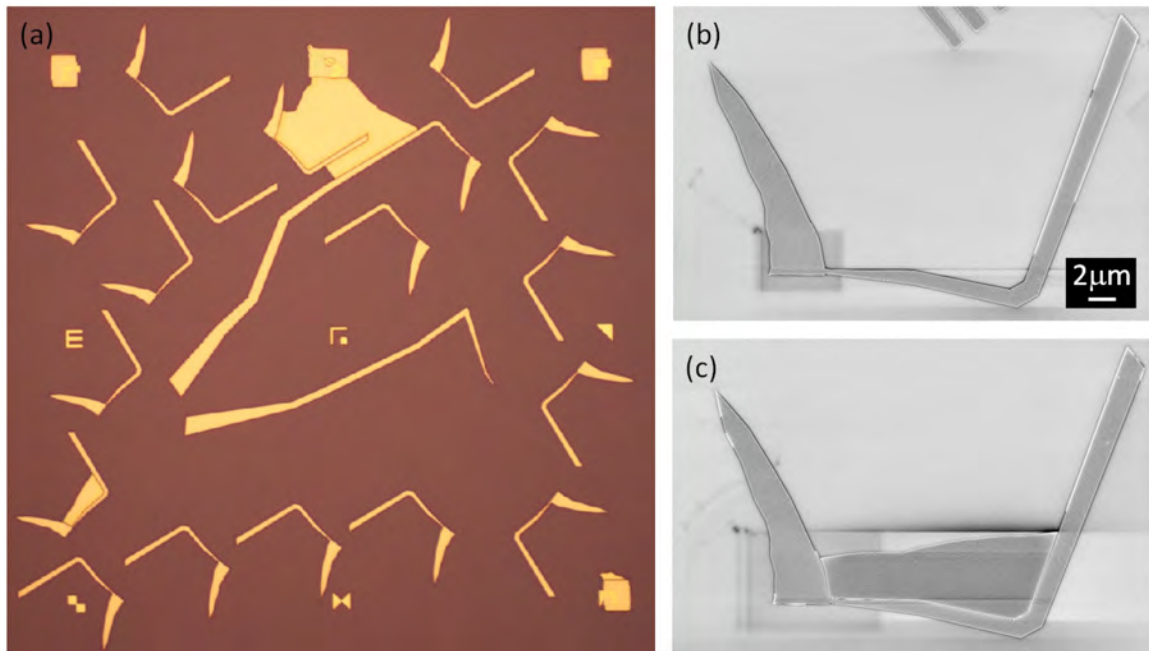


Figure 2.17: Optical (a) and SEM images (b-c) of test structures with patterned ALD-grown dielectric as well as metal top gates. An example of a clean and an unsuccessful lift-off is displayed in (b) and (c), respectively.

2.3.4 Hybrid top-gate dielectric

In trying to combine the merits of naturally oxidized Al and the simplicity of thermally evaporating SiO_x ($x = 1-2$), a top-gate dielectric composed of both a very thin layer of oxidized Al and thermally deposited SiO_x is proposed and investigated. A dual-gated graphene bipolar junction with a patterned hybrid top-gate dielectric is shown in

Fig. 2.18. The sample's electronic transport characteristics will be discussed in detail in Chapter 5.

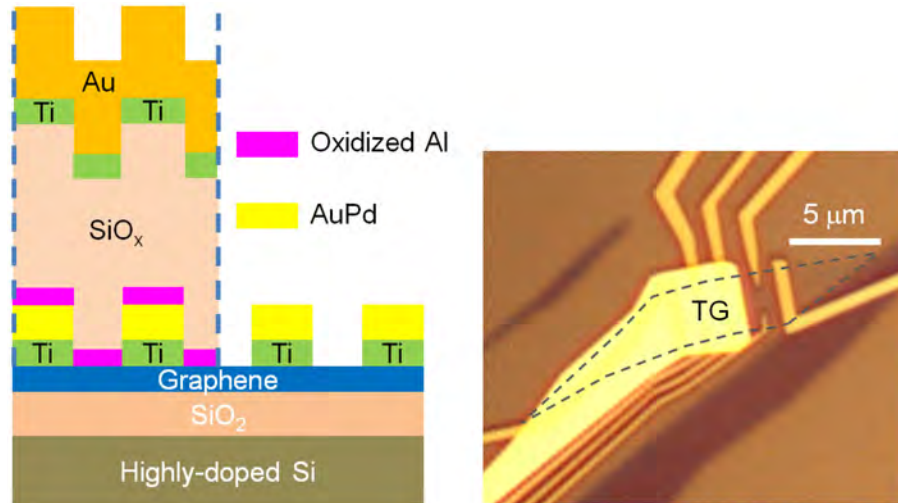


Figure 2.18: Cross-section (left) and optical image (right) of a bipolar graphene device featuring a patterned and hybrid top-gate (TG) dielectric. The gray dashed line in the right panel highlights the edge of the graphene sheet.

The first step in fabricating such a device is to define electrical contacts to graphene followed by hydrogen annealing. After the opening of a window in the PMMA resist for the top-gate with the help of electron beam lithography, deposition of Al, oxidization of Al by exposure to air, thermal evaporation of SiO_x and deposition of the metal top gate are carried out consecutively. Then another hydrogen annealing is performed after lift-off. Both thermal treatments in hydrogen atmosphere work well since the top-gate dielectric only partially covers the graphene sheet. This recipe results in high-quality bipolar graphene devices with a yield of nearly 100%.

2.3.5 Precise transfer of ultra-thin boron nitride films

The investigation of some topics in graphene physics, e.g. quantum capacitance measurement [25] and Coulomb drag between closely spaced single layers [26], requires

a very thin dielectric film. In these occasions, a hybrid dielectric prepared as described in previous section may not be the best option, as the negative effect due to the relatively high roughness of the oxidized Al is no longer negligible when the dielectric thickness is scaled down to a few nanometers. We need to develop a film “deposition” technique with which an ultra-thin yet highly insulating and homogeneous dielectric layer can be prepared on top of graphene without a significant degradation of the device quality. Precise transfer of atomically thin h-BN films onto target graphene sheets may hopefully fulfill these requirements. The detailed process is illustrated in Fig. 2.19.

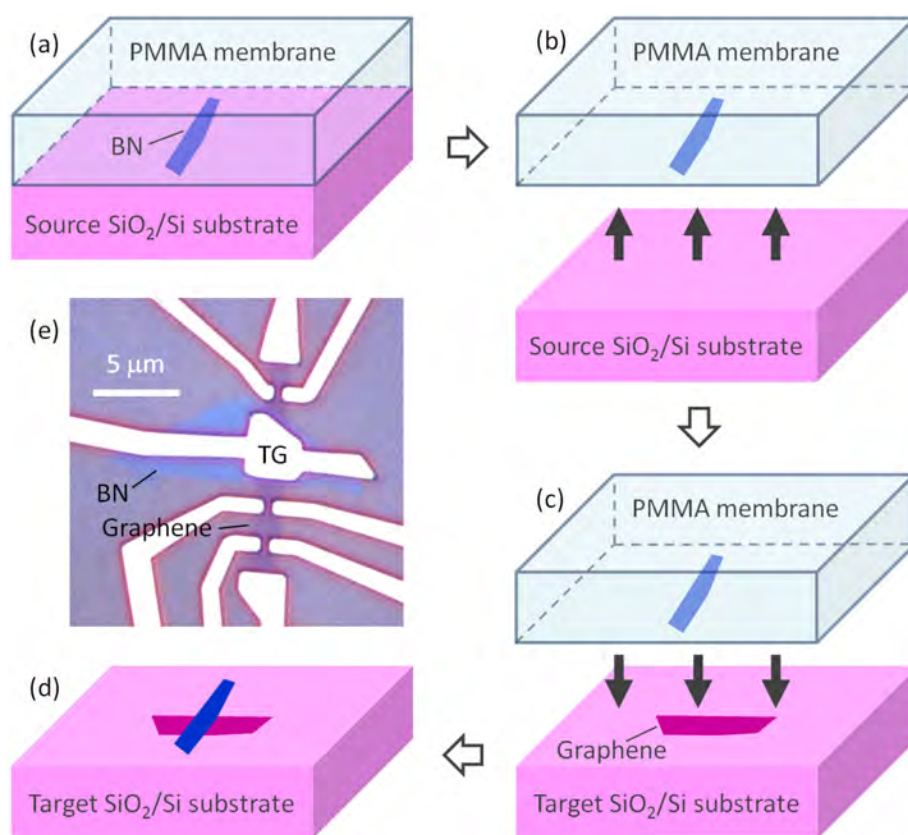


Figure 2.19: (a-d) Schematic representation outlining the transfer process used to fabricate BN-on-graphene devices. (a) The SiO₂/Si substrate that supports the source BN film is spin-coated with a PMMA layer (and then glued to a supporting glass frame). (b) The PMMA membrane along with the BN film and the imprints of alignment markers is detached from the source substrate by applying a NaOH etch. (c) With the help of a micro-manipulator, the source BN is aligned to the target graphene and the two sheets are brought into contact. (d) PMMA is dissolved in warm acetone or NMP. (e) Optical image of a finished BN-on-graphene device. The top-gate (TG) and the other electrodes are defined by standard electron beam lithography.

The procedure starts with the mechanical exfoliation of both source h-BN and target graphene sheets, which are identified on oxidized Si wafers with the aid of an optical microscope (and AFM topography measurements if necessary). The source substrate containing the h-BN flake is spin-coated with 300-500 nm thick PMMA. The PMMA is baked and glued to a supporting glass frame using a double-sided tape. This supporting frame with a hole (already covered by the attached source substrate from one side of the frame) in the center is then immersed in hot NaOH solution (5%, ~90°C) for about 10 minutes. This etches away the SiO₂ layer on the Si substrate, and results in the detachment of the source chip from the PMMA membrane (note that the PMMA membrane is still adhered to the glass frame). Now, the polymer membrane carries the source h-BN flake as well as the imprints of the source substrate's alignment markers. The h-BN film (together with the PMMA carrier) is then carefully aligned with the graphene sheet on the target substrate, with the help of a homemade 3D micro-manipulator and a large-working-distance optical microscope (VHX-1000 Digital Microscope of Keyence Corp.). After touchdown, the PMMA membrane is released from the supporting glass frame by dissolving the PMMA with chloroform. The remaining e-beam resist on the target substrate is removed in warm acetone or NMP, leaving only the h-BN film on top of the graphene sheet. The electrical contacts and metal top gate are subsequently defined with electron beam lithography, metallization and lift-off, followed by hydrogen annealing. Alternatively, one may anchor the target graphene sheet with electrodes first and anneal the target before h-BN transfer. Then a second e-beam lithography step is utilized to define the metal gate on top of transferred h-BN. This option may render a cleaner device at the expense of one more lithography step.

References

- [1] K. S. Novoselov, A. K. Geim, S. V. Morozov, D. Jiang, Y. Zhang, S. V. Dubonos, I. V. Grigorieva, and A. A. Firsov, *Electric field effect in atomically thin carbon films*, Science **306**, 666 (2004).
- [2] R. R. Nair, P. Blake, A. N. Grigorenko, K. S. Novoselov, T. J. Booth, T. Stauber, N. M. R. Peres, and A. K. Geim, *Fine structure constant defines visual transparency of graphene*, Science **320**, 1308 (2008).
- [3] P. Blake, E. W. Hill, A. H. C. Neto, K. S. Novoselov, D. Jiang, R. Yang, T. J. Booth, and A. K. Geim, *Making graphene visible*, Applied Physics Letters **91**, 063124 (2007).
- [4] E. D. Palik, *Handbook of optical constants of solids* (Academic, 1998), pp. 547-570.
- [5] B. Brixner, *Refractive-index interpolation for fused silica*, Journal of the Optical Society of America **57**, 674 (1967).
- [6] J. Henrie, S. Kellis, S. Schultz, and A. Hawkins, *Electronic color charts for dielectric films on silicon*, Opt. Express **12**, 1464-1469 (2004).
- [7] L. Pauling, *The nature of the chemical bond* (Cornell University Press, 1960), pp. 234-235.
- [8] M. Bruna and S. Borini, *Optical constants of graphene layers in the visible range*, Applied Physics Letters **94**, 031901 (2009).
- [9] H. Anders, *Thin films in optics* (Focal, 1967), pp. 18-48.
- [10] G. Giovannetti, P. A. Khomyakov, G. Brocks, P. J. Kelly, and J. van den Brink, *Substrate-induced band gap in graphene on hexagonal boron nitride: ab initio density functional calculations*, Physical Review B **76**, 073103 (2007).

- [11] K. Watanabe, T. Taniguchi, and H. Kanda, *Direct-bandgap properties and evidence for ultraviolet lasing of hexagonal boron nitride single crystal*, Nature Materials **3**, 404-409 (2004).
- [12] R. V. Gorbachev, I. Riaz, R. R. Nair, R. Jalil, L. Britnell, B. D. Belle, E. W. Hill, K. S. Novoselov, K. Watanabe, T. Taniguchi, A. K. Geim, and P. Blake, *Hunting for monolayer boron nitride: optical and Raman signatures*, Small **7**, 465-468 (2011).
- [13] J. R. Williams, L. DiCarlo, and C. M. Marcus, *Quantum Hall effect in a gate-controlled p-n junction of graphene*, Science **317**, 638-641 (2007).
- [14] K. S. Novoselov, A. K. Geim, S. V. Morozov, D. Jiang, M. I. Katsnelson, I. V. Grigorieva, S. V. Dubonos, and A. A. Firsov, *Two-dimensional gas of massless Dirac fermions in graphene*, Nature **438**, 197-200 (2005).
- [15] Y. Zhang, Y.-W. Tan, H. L. Stormer, and P. Kim, *Experimental observation of the quantum Hall effect and Berry's phase in graphene*, Nature **438**, 201 (2005).
- [16] G. Liu, J. J. Velasco, W. Bao, and C. N. Lau, *Fabrication of graphene p-n-p junctions with contactless top gates*, Applied Physics Letters **92**, 203103 (2008).
- [17] R. T. Weitz, M. T. Allen, B. E. Feldman, J. Martin, and A. Yacoby, *Broken-symmetry states in doubly gated suspended bilayer graphene*, Science **330**, 812-816 (2010).
- [18] X. Wang, S. M. Tabakman, and H. Dai, *Atomic layer deposition of metal oxides on pristine and functionalized graphene*, Journal of the American Chemical Society **130**, 8152-8153 (2008).
- [19] Y. M. Lin, K. A. Jenkins, V. G. Alberto, J. P. Small, D. B. Farmer, and P. Avouris, *Operation of graphene transistors at gigahertz frequencies*, Nano Letters **9**, 422-426 (2009).

- [20] J. Kim, B. Lee, S. Y. Park, H. C. Kim, K. Cho, E. M. Vogel, M. J. Kim, and R. M. Wallace, *Conformal Al₂O₃ dielectric layer deposited by atomic layer deposition for graphene-based nanoelectronics*, Applied Physics Letters **92**, 203102 (2008).
- [21] A. F. Young and P. Kim, *Quantum interference and Klein tunnelling in graphene heterojunctions*, Nature Physics **5**, 222-226 (2009).
- [22] B. Özyilmaz, P. Jarillo-Herrero, D. Efetov, D. A. Abanin, L. S. Levitov, and P. Kim, *Electronic transport and quantum Hall effect in bipolar graphene p-n-p junctions*, Physical Review Letters **99**, 166804 (2007).
- [23] Cambridge NanoTech Inc., *Tutorial to atomic layer deposition* (2005).
- [24] R. L. Puurunen, *Surface chemistry of atomic layer deposition: a case study for the trimethylaluminum/water process*, Journal of Applied Physics **97**, 121301-52 (2005).
- [25] J. Xia, F. Chen, J. Li, and N. Tao, *Measurement of the quantum capacitance of graphene*, Nature Nanotechnology **4**, 505 (2009).
- [26] H. Min, R. Bistritzer, J.-J. Su, and A. H. MacDonald, *Room-temperature superfluidity in graphene bilayers*, Physical Review B **78**, 121401 (2008).

Chapter 3

Electronic Transport in Graphene

In this chapter, we describe the “capacitor geometry” for the experimental investigation of electronic transport in monolayer graphene samples at zero magnetic fields. Through careful substrate-cleaning and lift-off, we find that without any thermal treatment room-temperature Drude mobility of our devices can reach $10000 \text{ cm}^2\text{V}^{-1}\text{s}^{-1}$ under ambient conditions at a carrier density $n \approx 4 \times 10^{12} \text{ cm}^{-2}$. We show that a relatively high initial-doping-level does not necessarily reflect a poor sample quality, and an *in situ* vacuum annealing is capable of shifting the charge neutrality point of a graphene device to nearly 0 V with however limited improvement on carrier mobility. On the basis of an excellent quantitative agreement with our measured data, we find it adequate to adopt a self-consistent Boltzmann theory within the random phase approximation to study the zero-field diffusive transport at reasonably large carrier densities. Within this formalism, both the strongly sublinear conductivity curve and the (estimated) low charged-impurity concentration ($\sim 10^{11} \text{ cm}^{-2}$) of our sample suggest that point defects in the graphene lattice most probably become the dominant source of scattering when the carrier density is reasonably high. Our surface morphology investigations and the surface study reported by other research groups indicate that organic residues, ripples and wrinkles on the graphene sheet, dangling bonds on SiO_2 surface and trapped charges on (or near) the surface of SiO_2 may be the major sources of charged impurities in our graphene devices.

3.1 Sample preparation and measurement methods

The monolayer graphene flakes are obtained using the mechanical exfoliation method described in Chapter 2. We use electron beam lithography to define electrodes on top of graphene, which are typically arranged into a Hall-bar geometry. After thermal evaporation of contact metals (Ti/AuPd = 3/20 nm), lift-off is carried out in warm NMP at 55-60°C for about 2 hours followed by rinsing in fresh acetone at ~55°C several times. In order to test the effectiveness of *in situ* vacuum annealing, the samples in this study are immediately loaded into the sample holder after lift-off without being thermally treated in flowing forming gas in-between.

Room-temperature measurements are performed in a home-made sample holder. It can be evacuated down to a pressure of about 10^{-6} mbar. Low-temperature transport experiments are done in a variable temperature insert (Oxford Instruments) with temperatures achievable from 1.4 to 300 K. In the insert, samples are cooled by a continuous flow of ^4He vapor. The resistances of the graphene samples are measured by the standard lock-in technique (Stanford Research Systems SR830 lock-in amplifier) with an excitation current of 100 nA_{rms} (Stanford Research Systems DS345 function generator in series connection with a 10 M Ω standard resistor) at a frequency of 23.87 Hz. The gate voltages were supplied by Yokogawa DC sources.

Fig. 3.1(a) illustrates the “capacitor geometry” commonly involved in our measurements. The graphene sheet and the degenerately doped Si are separated by a layer of thermally grown SiO₂ with a thickness between 285 and 315 nm. By varying the voltages applied to the highly doped Si, which serves as a back-gate, we are able to tune

the density and even the polarity of the charge carriers in the graphene sheet [1]. The gate-induced carrier density n_g is given by

$$n_g = C_{bg} V_{bg} / e, \quad (3.1)$$

where V_{bg} is the applied back-gate voltage and C_{bg} is the gate capacitance. From geometrical considerations, C_{bg} is estimated to be about 11.5 nF/cm^2 (assuming a dielectric thickness of 300 nm and a dielectric constant of 3.9 for the SiO_2 layer). In fact, we find that this estimation agrees well with our Hall measurements, as well as with an analysis of the Shubnikov-de Haas (SdH) oscillation period. This will be addressed in Chapter 4.

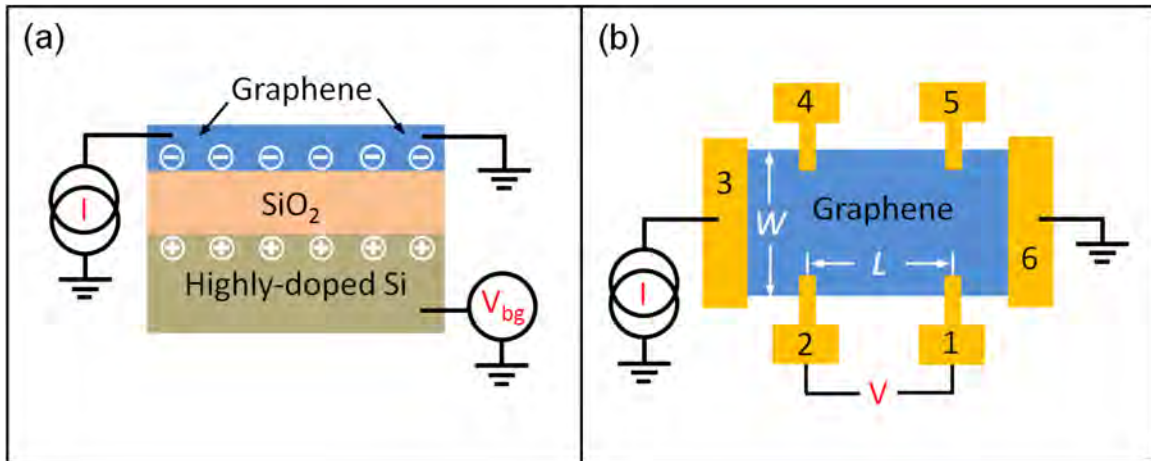


Figure 3.1: (a) Schematic illustration of the “capacitor geometry”, in which graphene and the degenerately doped silicon (wafer) act as the two electrodes of a capacitor. The sandwiched dry-oxidized SiO_2 dielectric has a thickness of $285\text{-}315 \text{ nm}$. Charges are induced in the graphene layer through the electric field effect by applying a back-gate voltage V_{bg} to the highly doped Si. (b) Schematic diagram of a typical four-terminal measurement setup. While a certain excitation current I is driven through the source and drain electrodes, the voltage difference V between the potential probes is measured. In this configuration, measurement results are not affected by the contact resistances.

The schematic of a standard four-terminal configuration is shown in Fig. 3.1(b).

During the measurement, an excitation current I_{sd} is driven through the source and drain

contacts (contacts 3-6 in the figure), and the induced voltage drop V_{2-1} between potential probes 2 and 1 (or equivalently, V_{4-5}) is measured. The four-terminal resistance R_{2-1} is given by V_{2-1} divided by I_{sd} , and graphene's resistivity ρ can then be obtained according to

$$\rho = R \left(\frac{L}{W} \right)^{-1}, \quad (3.2)$$

where W is the width of the graphene stripe, L the longitudinal separation between the voltage probes, and hence L/W the aspect ratio of the graphene device.

The semi-classical Drude model is employed to calculate the carrier mobility μ [2-4],

$$\mu = \frac{\sigma}{e|n|} = \frac{1}{e|n|\rho}, \quad (3.3)$$

where σ is the electrical conductivity of graphene and n the carrier density. A description of how n can be determined is deferred to the following section.

3.2 “Charge-neutrality-point engineering” via *in situ* annealing

Fig. 3.2(a) shows the electric field effect of resistivity ρ at zero magnetic field in a representative graphene device (left inset) before (red curve) and after (green curve) *in situ* vacuum annealing. The sharp peaks in the plot correspond to the Dirac point of graphene, where by definition the Fermi energy (strictly speaking, chemical potential when above zero Kelvin) approaches “zero” and the density of states vanishes [5] as schematically illustrated in the right inset. The reduced carrier density in the vicinity of the charge neutral Dirac point results in a resistivity maximum. When crossing the charge neutrality point, the carriers in the 2D graphene layer change polarity, as can be easily verified in Hall measurements. Note, however, that charge neutrality only holds on

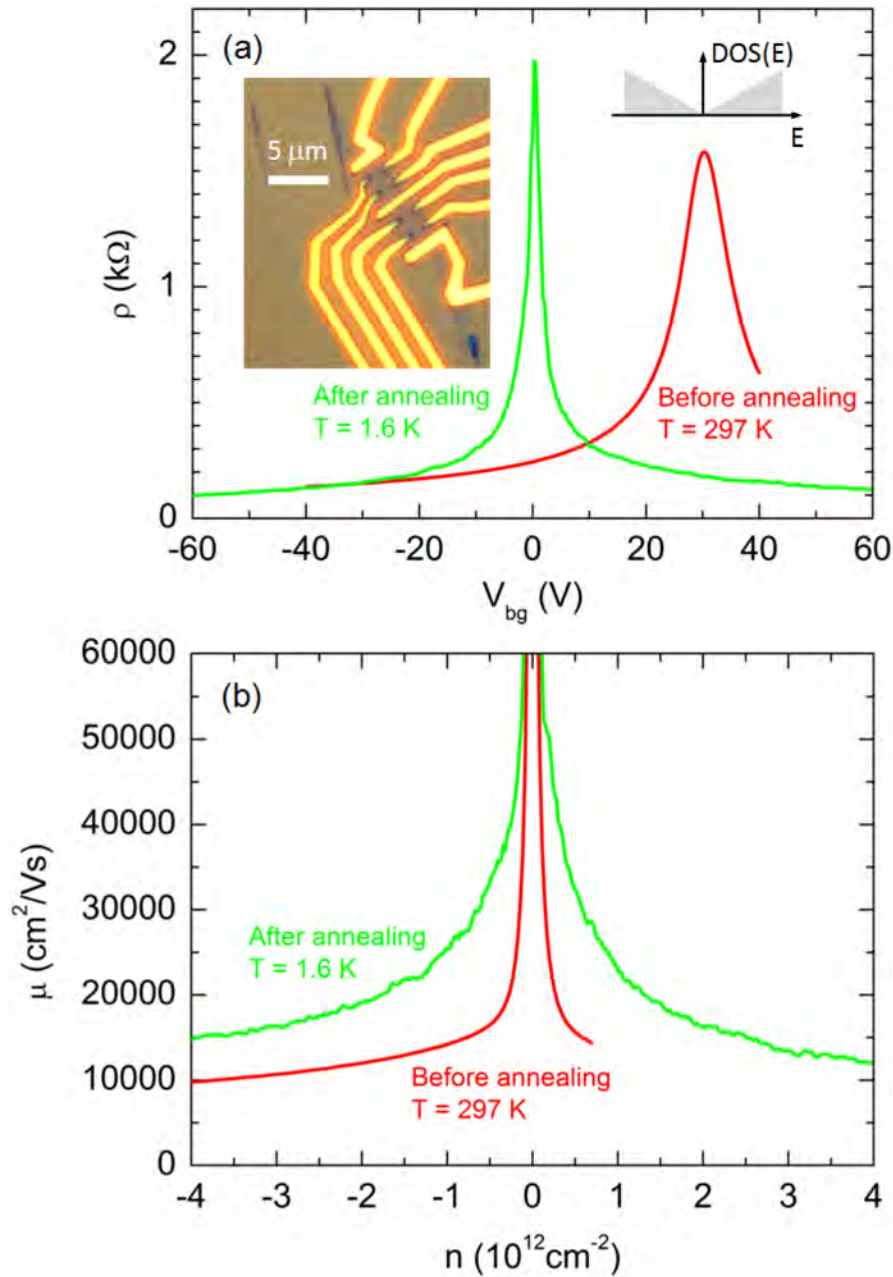


Figure 3.2: (a) Resistivity of a representative graphene sample as a function of the applied back-gate voltage measured before (red line) and after (green line) an *in situ* vacuum annealing. The optical micrograph of the device is shown in the left inset. The right inset schematically illustrates the linear relation between the density of states (DOS) and energy at low energies. (b) Drude mobility (obtained by applying Eq. 3.3 to the data in (a)) as a function of carrier density before (red line) and after (green line) annealing. The back-gate-induced charge density is estimated from the capacitor geometry illustrated in Fig. 3.1(a).

average [4, 6-12]. At charge neutrality, a spatially inhomogeneous distribution of small

electron-rich and hole-rich conducting puddles has been observed in graphene [7, 10] with the characteristic dimension about 20 nm [10]. Depending on the amplitude of the charge density fluctuations induced by the charged impurities, a few volts (or even more) back gate voltage may be needed to neutralize these electron or hole droplets [6, 7, 10].

Right after processing, the charge neutrality point (V_g^0) of the graphene device in Fig. 3.2(a) is found to be ~ 30 V, which indicates a relatively high p -doping (hole-doping) with a charge-doping concentration of about $2 \times 10^{12} \text{ cm}^{-2}$. A back-gate voltage of about 30 V is required to neutralize this hole-doping with electrons. Therefore, the actual carrier density n in the graphene sheet induced by the back-gate voltage in the presence of impurity doping is given by

$$n = C_{bg} (V_{bg} - V_g^0) / e, \quad (3.4)$$

where V_g^0 is 30 V in this case. The charge-providing impurities may be adsorbed gas molecules [13], e-beam resist residue, trapped charges on the surface or in the bulk of SiO_2 dielectric, etc. In our experiments, annealing in vacuum or forming gas has been found quite effective to shift the charge neutrality point close to 0 V, presumably by thermal desorption or decomposition of the adsorbates. We pump the sample holder to a pressure of $\sim 10^{-6}$ mbar prior to applying heating. The annealing temperature is maintained at about 130°C , while the four-terminal resistance of the graphene device at zero back-gate voltage is monitored throughout the heating. The charge neutrality point V_g^0 is observed to move monotonically toward 0 V, until it remains between 0 ± 3 V in most cases. For the majority of our samples, V_g^0 stabilizes within 3 hours of heating. The field effect recorded after annealing is plotted in Fig. 3.2(a) as the green curve. It is

measured at 1.6 K. The charge neutrality point is very close to zero back-gate voltage. The narrow resistance peak with an FWHM (full width at half maximum) of about 3 V serves as an indicator for a high cleanliness of the graphene sample [14]. The resistivity of graphene becomes as low as $\sim 100 \Omega$ at the relatively high carrier density of $\sim 4 \times 10^{12} \text{ cm}^{-2}$.

Fig. 3.2(b) shows the Drude mobility as a function of the charge density of the same device. The room-temperature hole mobility reaches $10000 \text{ cm}^2\text{V}^{-1}\text{s}^{-1}$ at a density of $4 \times 10^{12} \text{ cm}^{-2}$. For the sake of comparison, the electron or hole mobility in Si typically remains below $300 \text{ cm}^2\text{V}^{-1}\text{s}^{-1}$ for an ionized impurity concentration of 10^{18} cm^{-3} at room temperature [15]. We notice that the mobility of our device before vacuum annealing is already roughly twice that of the sample in Ref. [16] with $V_g^0 \sim 0 \text{ V}$. In ref. [4] and ref. [8], the authors found that a large $|V_g^0|$ was generally accompanied by a low carrier mobility. While it may hold for some types of disorder, this may not be a general rule. We have observed that graphene samples on dirty (e.g. with an organic residue network on top of SiO_2 visible in an optical microscope at virtually any magnification) or very rough (i.e. with the surface root-mean-square roughness of the SiO_2 layer much higher than the usual value that is between 0.3 and 0.4 nm) oxidized-Si substrates consistently show poor mobility (as low as $\mu < 2000 \text{ cm}^2\text{V}^{-1}\text{s}^{-1}$ at $n \sim 4 \times 10^{12} \text{ cm}^{-2}$) regardless of the heat treatment, although the charge neutrality point of most of these devices could still be shifted to $\sim 0 \text{ V}$ by *ex situ* hydrogen annealing or/and *in situ* vacuum annealing. For a “most-likely-high-quality” device shown in Fig. 3.2, the improvement on the sample’s mobility by annealing also appears limited, if not marginal, considering the enhanced phonon scattering at elevated temperatures. Note, however, that at relatively large carrier

densities graphene resistivity arising from charged impurity scattering should be essentially independent of temperature within a wide temperature range [6]. This is because based on the linear energy-momentum dispersion relation the Fermi temperature T_F in graphene is defined as [5, 16, 17]

$$T_F = |E_F| / k = |\hbar k_F v_F| / k = \hbar v_F \sqrt{\pi |n|} / k, \quad (3.5)$$

where $k_F = \sqrt{\pi |n|}$ is the Fermi wave vector and $v_F \sim 10^6$ m/s [2, 3] is the Fermi velocity of the relativistic particles in graphene. At a carrier density $n = 4 \times 10^{12}$ cm⁻², the corresponding Fermi temperature is as high as 2700 K.

It is worthwhile to point out that at either room temperature or low temperature μ in Fig. 3.2(b) diverges when n approaches zero, indicating the break-down of the Drude-Boltzmann transport model at low carrier densities (i.e. $n \leq n_{im}$) in graphene [6].

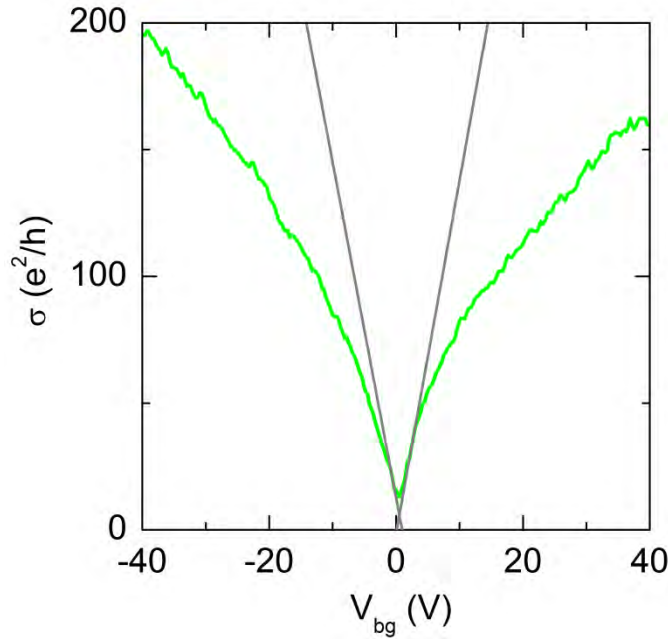


Figure 3.3: Conductivity (of the representative device shown in Fig. 3.2(a)) after annealing versus applied back-gate voltage at a temperature of 1.6 K (green line). Gray lines are fits to the linear parts of the curve at relatively low charge densities based on Eq. 3.6. The crossing defines the charge neutrality point [8]. Charged-impurity concentration n_{im} can be estimated from the slope and yields $n_{im} \sim 1.1 \times 10^{11}$ cm⁻² as explained in the text.

To estimate the density of charged impurities n_{im} in the sample after vacuum annealing, we employ the self-consistent Boltzmann theory within the random phase approximation introduced by ref. [9] and [6]. When the graphene conductivity is limited by charged-impurity scattering, the conductivity can be expressed as [18-20]

$$\sigma(n) = C^0 e \left| \frac{n}{n_{im}} \right| + \sigma_{res}, \quad (3.6)$$

where $C^0 = 5 \times 10^{15} \text{ V}^{-1} \text{ s}^{-1}$ is a constant [6] and σ_{res} is the residual conductivity at the charge neutrality point (Note: σ_{res} is determined by a linear fit to the measured $\sigma(V_{bg})$). This residual conductivity will be discussed later. It very often differs from the measured minimum conductivity σ_{min} [8, 19, 20]. According to Eq. 3.6, the graphene conductivity scales linearly with the carrier density n , when charged impurities being the dominating scattering mechanism. Now let us examine our experimental data. The green line in Fig. 3.3 shows the low-temperature conductivity σ after annealing as a function of the back-gate voltage V_{bg} for the same sample as in Fig. 3.2. A linear dependence of σ on V_{bg} is only observed at rather low carrier densities. By adopting a least-square fitting method similar to that in ref. [18], we fit the low-density regions on both electron and hole sides to eq. 3.6. These fits are indicated as the gray lines in Fig. 3.3. The crossing of the two fits yields the charge neutrality point [8]. It is located at a back-gate voltage of $\sim 0.5 \text{ V}$. The strong sublinearity in the original $\sigma(V_{bg})$ plot at high carrier densities indicates that in this type of sample the (neutral) point defects in the graphene lattice are most probably the dominant source of scattering because the concentration of charged impurities is low [4, 6, 8]. The slopes of both fits give $n_{im} \sim 1.1 \times 10^{11} \text{ cm}^{-2}$ (since $|slope| = C^0 C_{bg} / n_{im}$ according to Eq. 3.4 and 3.6), which reflects the high cleanliness of the device [4], and is

consistent with the measured mobility values. Interestingly, the FWHM of the $\rho(V_{bg})$ spike in Fig. 3.2(a) is ~ 3 V, and half of that corresponds to a charge density of $\sim 1.1 \times 10^{11}$ cm^{-2} , which “coincidentally” equals the n_{im} value obtained by fitting. We find in general that the FWHM of the sample’s low-temperature $\rho(V_{bg})$ curve provides a good estimate of n_{im} . The residual conductivity σ_{res} at charge neutrality ($n = 0$) can be obtained by rewriting Eq. 3.6 in the following form

$$\sigma(V_{bg}) = C^0 C_{bg} \left| \frac{V_{bg} - V_g^0}{n_{im}} \right| + \sigma_{res} = \text{slope_of_the_fit} \cdot (V_{bg} - V_g^0) + \sigma_{res}. \quad (3.7)$$

Here, $V_g^0 \sim 0.5$ V is the charge neutrality point from the crossing of the two linear fits. Since the slope of either fit is already known, it is straightforward to obtain $\sigma_{res} \sim 5.7 e^2/h$ on the electron side, and $\sim 6.0 e^2/h$ on the hole side. Notice that both numbers are close to the σ_{res} obtained from the crossing point of the linear fits ($\sim 5.8 e^2/h$, according to Eq. 3.6 and 3.7). These quantities are similar to reported values in the literature [19].

The relationship between electrical conductivity σ and carrier density n can also provide us information about the mean free path l_m of the charge carriers in the sample. To express l_m explicitly as a function of σ and n within the Boltzmann model, we write the Einstein relation [17] between the conductivity and Fermi level properties in the following equivalent forms:

$$\sigma = e^2 D^* D(E_F) = \frac{2e^2}{h} k_F v_F \tau = \frac{2e^2}{h} \sqrt{\pi |n|} \cdot l_m, \quad (3.8)$$

where D^* is the diffusion constant at the Fermi Energy E_F , $D(E_F)$ is the density of states at E_F and τ is the scattering time. In the above equalities, we have utilized the identities

$$D^* = 1/2 v_F^2 \tau \text{ [17]}, \quad D(E_F) = 2E_F (\pi \hbar^2 v_F^2)^{-1} \text{ [17]}, \quad E_F = \hbar k_F v_F \text{ [5]} \text{ and } k_F = \sqrt{\pi |n|} \text{ [17]}, \text{ as}$$

well as the definition $l_m = v_F \tau$. Fig. 3.4 depicts the resulting low-temperature $l_m(n)$ plot for the sample in Fig. 3.2(a). In this device, the carrier mean free path between two consecutive scattering events ranges from 220 nm to 360 nm over nearly the whole density range. The fact that these l_m values are much smaller than the typical dimension (a few microns) of our graphene samples validates the adequateness of treating the transport in the diffusive regime by employing the Boltzmann transport theory.

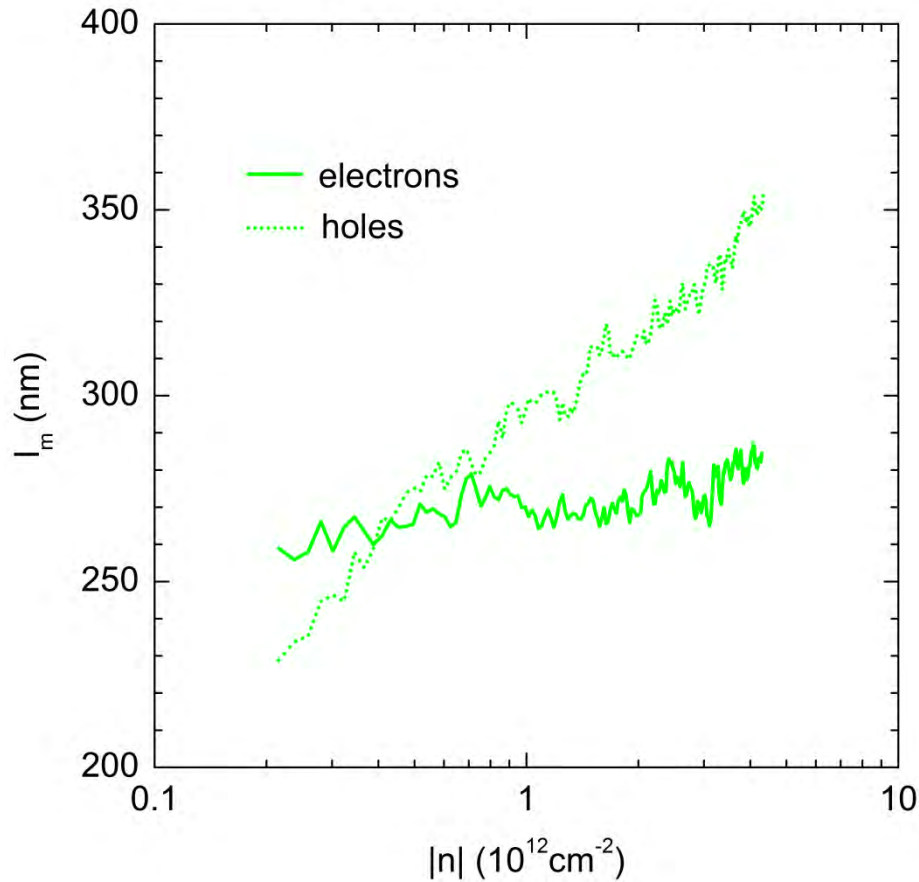


Figure 3.4: Estimated carrier mean free path (of the sample in Fig. 3.2(a)) as a function of density at a temperature of 1.6 K based on Eq. 3.8. The maximum mean free path (~ 360 nm) is about one order of magnitude shorter than the dimension of the graphene sample. Hence, it is justified to use the Boltzmann transport model.

We have shown that through careful substrate-cleaning and lift-off we are able to fabricate graphene devices featuring room-temperature mobility $\geq 10000 \text{ cm}^2 \text{ V}^{-1} \text{ s}^{-1}$

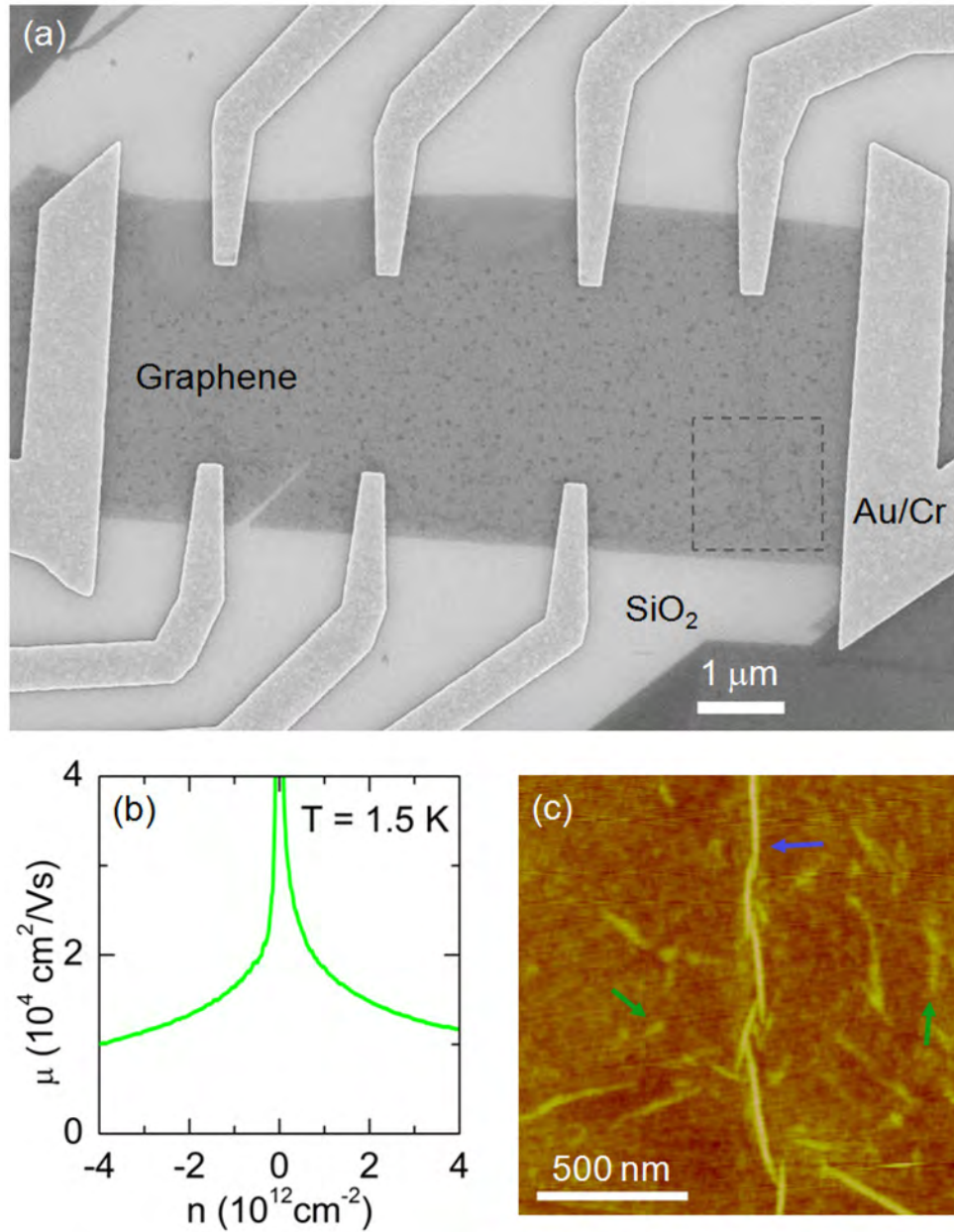


Figure 3.5: SEM image (a) and low-temperature Drude mobility (b) of an ordinary graphene sample obtained after *in situ* vacuum annealing. In the SEM micrograph the exposed SiO₂ substrate appears rather clean, in contrast to a random network of tiny dark spots visible within the graphene flake region. AFM topography of the area in the dashed box is shown in (c). The wrinkle (indicated by the blue arrow) features a height of 5-6 nm, while the little bumps (highlighted by the green arrows) that correspond to the tiny dark spots in (a) are generally lower than 3 nm.

without any thermal treatment. However, we also observed that it is generally very

difficult to obtain sample mobilities above $20000 \text{ cm}^2\text{V}^{-1}\text{s}^{-1}$ even with the help of annealing (e.g. a thermal treatment at $\sim 400^\circ\text{C}$ in flowing forming gas for a few hours). We suspect that the ultimate hindrance to the gigantic intrinsic mobility [21] of graphene comes from the imperfections in the SiO_2 back-gate dielectric [6, 21] that directly supports the graphene flake, as well as the interactions among the graphene sheet, the SiO_2 surface and the organic solvents that cause deformations in the carbon film. Fig. 3.5(a) shows the secondary-electron SEM image of an ordinary graphene sample after *in situ* vacuum annealing (with the charge neutrality point being shifted to $\sim 0 \text{ V}$), while Fig. 3.5(b) depicts its low-temperature post-annealing mobility. The device was electrically contacted and grounded before being loaded into the SEM chamber, essentially excluding any charging effect during the scan. Randomly distributed dark spots, a crack with a length $\sim 1 \mu\text{m}$ near the edge and a wrinkle spreading nearly across the flake are clearly visible on the SEM micrograph. These dark spots correspond to the small bumps on the AFM topography picture shown in Fig. 3.5(c) with heights below 3 nm , while the wrinkle was measured to be $5\text{-}6 \text{ nm}$ in height. These macroscopic imperfections, especially the small bumps and wrinkles, are commonly found in SiO_2 -supported graphene devices. Generally, a thermal treatment in either vacuum or flowing forming gas at elevated temperatures and/or with prolonged time could not eliminate them completely. We suspect that the bumps are essentially ripples in the graphene sheet, underneath which organic residues exist. These organic residues, together with the dangling bonds on SiO_2 surface and the trapped charges either on the surface or in the bulk of SiO_2 [6, 21], most probably form the major sources of charged impurities. Therefore, in order to approach the expected giant intrinsic carrier mobilities [22] in graphene, one has to reconsider the

choice of the back-gate dielectric. Among many possible alternatives to SiO₂, suspended graphene in air (or vacuum) [23-27], a dangling-bond-free substrate such as hexagonal boron nitride [14, 28-30], and a diamond-like non-polar dielectric [31] appear most promising. These are all, however, at the expense of extra fabrication steps.

References

- [1] K. S. Novoselov, A. K. Geim, S. V. Morozov, D. Jiang, Y. Zhang, S. V. Dubonos, I. V. Grigorieva, and A. A. Firsov, *Electric field effect in atomically thin carbon films*, Science **306**, 666 (2004).
- [2] K. S. Novoselov, A. K. Geim, S. V. Morozov, D. Jiang, M. I. Katsnelson, I. V. Grigorieva, S. V. Dubonos, and A. A. Firsov, *Two-dimensional gas of massless Dirac fermions in graphene*, Nature **438**, 197-200 (2005).
- [3] Y. Zhang, Y.-W. Tan, H. L. Stormer, and P. Kim, *Experimental observation of the quantum Hall effect and Berry's phase in graphene*, Nature **438**, 201 (2005).
- [4] Y. W. Tan, Y. Zhang, K. Bolotin, Y. Zhao, S. Adam, E. H. Hwang, S. D. Sarma, H. L. Stormer, and P. Kim, *Measurement of scattering rate and minimum conductivity in graphene*, Physical Review Letters **99**, 246803 (2007).
- [5] P. R. Wallace, *The band theory of graphite*, Physical Review **71**, 622 (1947).
- [6] E. H. Hwang, S. Adam, and S. D. Sarma, *Carrier transport in two-dimensional graphene layers*, Physical Review Letters **98**, 186806 (2007).
- [7] J. Martin, N. Akerman, G. Ulbricht, T. Lohmann, J. H. Smet, K. von Klitzing, and A. Yacoby, *Observation of electron-hole puddles in graphene using a scanning single-electron transistor*, Nature Physics **4**, 144 (2008).
- [8] J. H. Chen, C. Jang, S. Adam, M. S. Fuhrer, E. D. Williams, and M. Ishigami, *Charged-impurity scattering in graphene*, Nature Physics **4**, 377 (2008).
- [9] S. Adam, E. H. Hwang, V. M. Galitski, and S. Das Sarma, *A self-consistent theory for graphene transport*, Proceedings of the National Academy of Sciences **104**, 18392-18397 (2007).

- [10] Y. Zhang, V. W. Brar, C. Girit, A. Zettl, and M. F. Crommie, *Origin of spatial charge inhomogeneity in graphene*, Nature Physics **5**, 722-726 (2009).
- [11] T. Ando, *Screening effect and impurity scattering in monolayer graphene*, J. Phys. Soc. Jpn. **75**, 074716 (2006).
- [12] K. Nomura and A. H. MacDonald, *Quantum transport of massless Dirac fermions*, Physical Review Letters **98**, 076602 (2007).
- [13] F. Schedin, A. K. Geim, S. V. Morozov, E. W. Hill, P. Blake, M. I. Katsnelson, and K. S. Novoselov, *Detection of individual gas molecules adsorbed on graphene*, Nature Materials **6**, 652-655 (2007).
- [14] C. R. Dean, A. F. Young, I. Meric, C. Lee, L. Wang, S. Sorgenfrei, K. Watanabe, T. Taniguchi, P. Kim, K. L. Shepard, and J. Hone, *Boron nitride substrates for high-quality graphene electronics*, Nature Nanotechnology **5**, 722-726 (2010).
- [15] S. M. Sze, *Physics of semiconductor devices* (John Wiley & Sons, Inc., 3 ed, 2007), pp. 29.
- [16] A. K. Geim and K. S. Novoselov, *The rise of graphene*, Nature Materials **6**, 183-191 (2007).
- [17] C. W. J. Beenakker and H. van Houten, *Quantum transport in semiconductor nanostructures*, Solid State Physics **44**, 1-228 (1991).
- [18] J. H. Chen, C. Jang, S. Adam, M. S. Fuhrer, E. D. Williams, and M. Ishigami, *Charged-impurity scattering in graphene*, Nat Phys **4**, 377 (2008).
- [19] M. Trushin and J. Schliemann, *Minimum electrical and thermal conductivity of graphene: A quasiclassical approach*, Physical Review Letters **99**, 216602 (2007).
- [20] X.-Z. Yan, Y. Romiah, and C. S. Ting, *Electric transport theory of Dirac fermions in graphene*, Physical Review B **77**, 125409 (2008).

- [21] J. H. Chen, C. Jang, S. Xiao, M. Ishigami, and M. S. Fuhrer, *Intrinsic and extrinsic performance limits of graphene devices on SiO₂*, *Nature Nanotechnology* **3**, 206-209 (2008).
- [22] S. V. Morozov, K. S. Novoselov, M. I. Katsnelson, F. Schedin, D. C. Elias, J. A. Jaszczak, and A. K. Geim, *Giant intrinsic carrier mobilities in graphene and its bilayer*, *Physical Review Letters* **100**, 016602 (2008).
- [23] K. I. Bolotin, K. J. Sikes, Z. Jiang, M. Klima, G. Fudenberg, J. Hone, P. Kim, and H. L. Stormer, *Ultrahigh electron mobility in suspended graphene*, *Solid State Communications* **146**, 351-355 (2008).
- [24] K. I. Bolotin, K. J. Sikes, J. Hone, H. L. Stormer, and P. Kim, *Temperature-dependent transport in suspended graphene*, *Physical Review Letters* **101**, 096802 (2008).
- [25] X. Du, I. Skachko, A. Barker, and E. Y. Andrei, *Approaching ballistic transport in suspended graphene*, *Nature Nanotechnology* **3**, 491-495 (2008).
- [26] X. Du, I. Skachko, F. Duerr, A. Luican, and E. Y. Andrei, *Fractional quantum Hall effect and insulating phase of Dirac electrons in graphene*, *Nature* **462**, 192-195 (2009).
- [27] K. I. Bolotin, F. Ghahari, M. D. Shulman, H. L. Stormer, and P. Kim, *Observation of the fractional quantum Hall effect in graphene*, *Nature* **462**, 196-199 (2009).
- [28] C. R. Dean, A. F. Young, P. Cadden-Zimansky, L. Wang, H. Ren, K. Watanabe, T. Taniguchi, P. Kim, J. Hone, and K. L. Shepard, *Multicomponent fractional quantum Hall effect in graphene*, *Nature Physics* **7**, 693-696 (2011).
- [29] J. Xue, J. Sanchez-Yamagishi, D. Bulmash, P. Jacquod, A. Deshpande, K. Watanabe, T. Taniguchi, P. Jarillo-Herrero, and B. J. LeRoy, *Scanning tunnelling microscopy and spectroscopy of ultra-flat graphene on hexagonal boron nitride*, *Nature Materials* **10**, 282-285 (2011).

- [30] R. G. Decker, Y. Wang, V. W. Brar, W. Regan, H.-Z. Tsai, Q. Wu, W. Gannett, A. Zettl, and M. F. Crommie, *Local electronic properties of graphene on a BN substrate via scanning tunneling microscopy*, Nano Letters 2291-2295 (2011).
- [31] Y. Wu, Y.-m. Lin, A. A. Bol, K. A. Jenkins, F. Xia, D. B. Farmer, Y. Zhu, and P. Avouris, *High-frequency, scaled graphene transistors on diamond-like carbon*, Nature **472**, 74-78 (2011).

Chapter 4

Magneto-Transport in Graphene

In this chapter, we probe the quantum Hall effect (QHE) in graphene using a four-terminal configuration in a magnetic field perpendicular to the graphene plane. From the measured longitudinal and Hall resistivities we obtain the magneto-conductivities of the graphene sample through matrix inversion operations. Due to the existence of a zeroth Landau level (LL) at zero energy which is equally shared by the electrons and holes, the quantized Hall conductivity σ_{xy} in graphene bears an unconventional sequence of $\sigma_{xy} = \pm 4(|N| + 1/2)e^2/h$, where N is the LL index. Besides the unconventional QHE, we observe a quantum Hall state at filling factor $\nu = 0$ in high-quality samples under very low excitation currents. We then demonstrate the extraction of the back-gate capacitance from the Shubnikov-de Haas (SdH) oscillations in graphene. The result justifies the simple parallel-plate capacitor model as introduced in Chapter 3. We proceed to measure a large critical current associated with the breakdown of the $\nu = 2$ quantum Hall state. The observed extraordinarily robust QHE at $\nu = 2$ may probably help to qualify graphene as an excellent candidate material for the quantum resistance standard.

4.1 Experimental methods and measurement setup

In a sufficiently strong magnetic field perpendicular to the graphene layer, the zero-field linear low-energy spectrum in graphene quantizes into discrete Landau levels (see Chap. 1). The Landau spectrum in graphene is described by [1-3]

$$E_N = \pm v_F \sqrt{2e\hbar B |N|}, \quad (4.1)$$

where v_F is the Fermi velocity ($\sim 10^6$ m/s [4, 5]), B is the magnetic field, N is the Landau level (LL) index, and the positive and negative signs stand for electrons and holes, respectively. Due to the inevitable presence of disorder in exfoliated graphene, these LLs become broadened and mobility gaps appear [6]. At zero energy there is a unique zeroth LL ($N = 0$ in Eq. 4.1) which is equally shared by electrons and holes. The LL spacing between the zeroth and first LLs at $B = 14$ T is as high as 149 meV, or equivalently, 1730 K. We note that this energy spacing is more than six times the cyclotron energy of the 2DES in GaAs/AlGaAs heterostructures [7].

In a perpendicular external magnetic field, both the resistivity and the (electric) conductivity of a 2DES in a Hall-bar geometry take tensor forms, with the conductivity tensor $\hat{\sigma}$ being the inverse of the resistivity tensor $\hat{\rho}$: $\hat{\sigma} = \hat{\rho}^{-1}$. On the basis of Ohm's law and the assumption of isotropy in the two-dimensional (2D) plane, $\hat{\rho}$ can be written as

$$\hat{\rho} = \begin{pmatrix} \rho_{xx} & \rho_{xy} \\ -\rho_{xy} & \rho_{xx} \end{pmatrix}, \quad (4.2)$$

where ρ_{xx} and ρ_{xy} are the longitudinal and transverse components of the 2D resistivity, respectively. A simple matrix inversion operation gives

$$\hat{\sigma} = \begin{pmatrix} \sigma_{xx} & \sigma_{xy} \\ -\sigma_{xy} & \sigma_{xx} \end{pmatrix} = \frac{1}{\rho_{xx}^2 + \rho_{xy}^2} \begin{pmatrix} \rho_{xx} & -\rho_{xy} \\ \rho_{xy} & \rho_{xx} \end{pmatrix}, \quad (4.3)$$

where σ_{xx} and σ_{xy} are the longitudinal and transverse (or, Hall) components of the 2D conductivity, respectively. Hence we have

$$\sigma_{xx} = \frac{\rho_{xx}}{\rho_{xx}^2 + \rho_{xy}^2} \quad (4.4)$$

and

$$\sigma_{xy} = -\frac{\rho_{xy}}{\rho_{xx}^2 + \rho_{xy}^2}. \quad (4.5)$$

Using the same matrix conversion method, it is straightforward to obtain

$$\rho_{xx} = \frac{\sigma_{xx}}{\sigma_{xx}^2 + \sigma_{xy}^2} \quad (4.6)$$

and

$$\rho_{xy} = -\frac{\sigma_{xy}}{\sigma_{xx}^2 + \sigma_{xy}^2}. \quad (4.7)$$

The QHE in a 2DES (with a Hall-bar geometry) is defined by a vanishing longitudinal conductivity σ_{xx} , associated with a Hall conductivity σ_{xy} quantized in multiples of e^2/h : $\sigma_{xy} = \nu e^2/h$, where ν is an integer filling factor [6, 8]. Here, electrons (holes) are assigned with positive (negative) filling factors. According to Eq. 4.7, ρ_{xy} equals $-1/\sigma_{xy}$ in a quantum Hall state (when $\sigma_{xy} \neq 0$, of course). In a 2DES, the Hall resistivity ρ_{xy} is identical to the Hall resistance R_{xy} . Therefore, the QHE in the 2DES of a Hall-bar sample features a quantized Hall resistance $R_{xy} = h/\nu e^2$. When $\nu = 1$, $R_{xy} = R_K = h/e^2 = 25812.807557(18) \Omega$ [9] is the von Klitzing constant. To date, the QHE allows the international standard for resistance to be defined on the basis of R_K , which can be

reproduced within a relative uncertainty of one part per billion [7, 9] and is theoretically only linked to the electron charge and Planck's constant. In addition, the QHE provides a new method for the determination of the fine structure constant $\alpha = e^2/2\epsilon_0 ch$ [10], where ϵ_0 is the permittivity of free space and c is the speed of light in vacuum.

To probe the QHE and SdH oscillations in graphene, we isolated graphene flakes on top of oxidized Si wafers via mechanical exfoliation. The electrodes of the graphene devices were defined into Hall-bar geometries by electron beam lithography. A vacuum or H₂ annealing was always carried out after lift-off in order to shift the charge neutrality point of the graphene sample toward 0 V.

Fig. 4.1(a) schematically illustrates the four-terminal setup for the majority of the measurements discussed in this chapter. In this configuration, a low-frequency ($f < 30$ Hz) excitation current I_{sd} is driven through the source and drain contacts (contacts 3-6 in the figure), and the potential differences V_{2-1} (or V_{4-5}) and V_{2-4} (or V_{1-5}) are measured at the voltage probes by the standard lock-in technique. The longitudinal resistance R_{xx} is obtained by $R_{xx} = V_{2-1}/I_{sd}$, while the Hall resistance R_{xy} equals V_{2-4}/I_{sd} . Then the longitudinal and Hall resistivities are given by $\rho_{xx} = R_{xx} W/L$ and $\rho_{xy} = R_{xy}$, respectively. Here W is the width of the graphene stripe and L the longitudinal separation between the involved voltage probes.

Fig. 4.1(b) shows the configuration particularly suitable for low-dissipation measurements on highly resistive samples. A low-frequency ($f < 10$ Hz) voltage is applied between the source and drain electrodes by a function generator (Stanford Research Systems DS345) and a voltage divider (100:1 or 1000:1). The current (typically below 5 nA) flowing through source-drain is monitored by a low-noise current

preamplifier (Ithaco 1211 powered by batteries), the output of which is read by a lock-in amplifier (Stanford Research Systems SR830). Voltage differences between the voltage probes are amplified by high-input-impedance voltage preamplifiers (Stanford Research Systems SR560 with an input impedance $100\text{M}\Omega \parallel 25\text{pF}$), and then recorded by lock-in amplifiers.

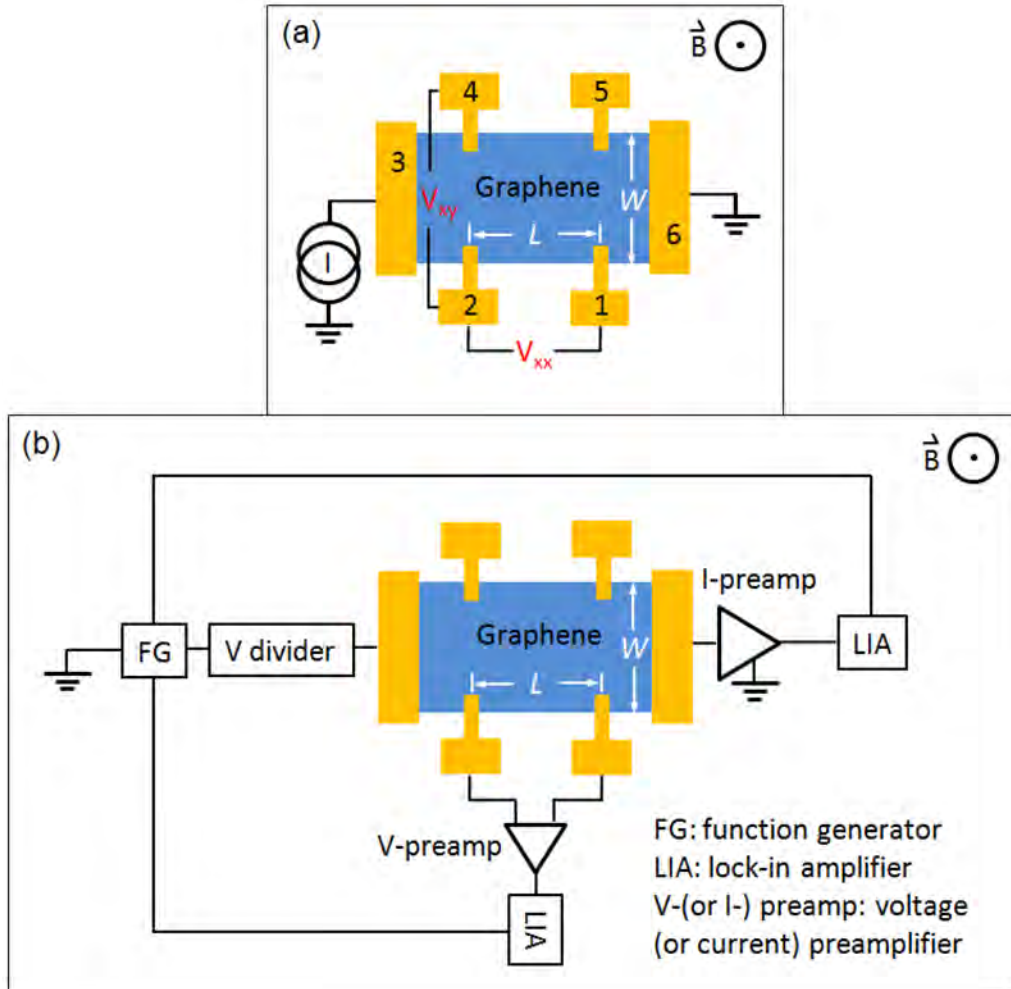


Figure 4.1: (a) Four-terminal Hall-bar configuration for magneto-transport measurements. In this setup, longitudinal voltage V_{xx} and Hall voltage V_{xy} are sensed via the voltage probes when a certain excitation current I is driven through the source and drain electrodes. (b) Experimental setup for low-dissipation measurements. It is particularly suitable for highly resistive samples operated at low frequencies. The voltage output of a function generator is divided before being applied across the source and drain electrodes. The small current flowing through the sample is amplified by a low-noise current-preamplifier and then recorded by a lock-in amplifier. Any tiny voltage signal between the voltage probes is amplified by a high-input-impedance voltage-preamplifier before being sent into by another lock-in amplifier.

All of our magneto-transport measurements are performed in a variable temperature insert (Oxford Instruments) with temperatures between 1.4 and 300 K. Samples are cooled by a continuous flow of ^4He vapor. An external magnetic field (up to 15 T) perpendicular to the graphene plane is applied using a superconducting magnet.

4.2 Quantum Hall effect and its breakdown in graphene

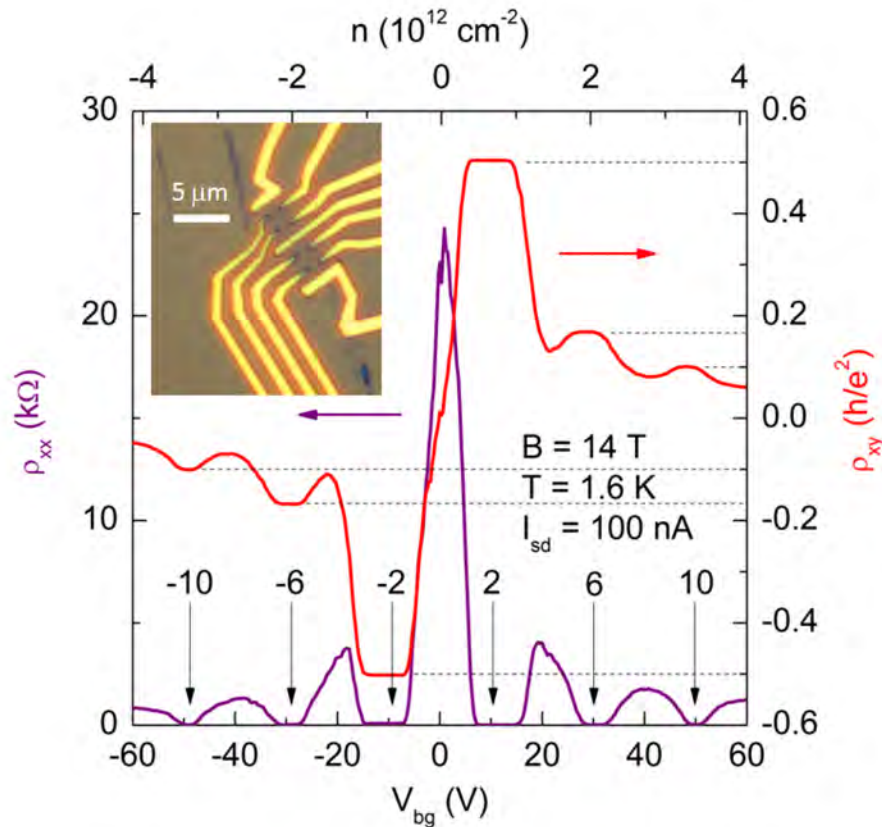


Figure 4.2: Magneto-resistivities as a function of the applied back-gate voltage for the graphene device shown in the inset. Well developed quantum Hall plateaus with precisely quantized Hall resistivities and vanishing longitudinal resistivities occur at filling factors ± 2 , ± 6 and ± 10 (indicated by the vertical black arrows with the corresponding filling factors on top).

Fig. 4.2 depicts the longitudinal and Hall resistivities (ρ_{xx} and ρ_{xy}) as a function of the back-gate voltage V_{bg} for the sample shown in the inset. During the magneto-resistance measurement, a current bias of $100 \text{ nA}_{\text{rms}}$ is applied in a magnetic field $B = 14 \text{ T}$ at a

temperature $T = 1.6$ K. The back-gate capacitance (see Chapter 3) is extracted by analyzing how the periodicity of the Shubnikov-de Haas oscillations changes with the back-gate voltage. The details of the extraction will be addressed later. The filling factor ν is calculated according to the formula $\nu = hn / eB$, where n is the carrier density in the graphene layer. During the back-gate sweep, V_{bg} is varied from -60 V to 60 V. The Fermi energy E_F (strictly speaking, chemical potential when $T > 0$) in the 2DES is shifted continuously [11-13] with

$$E_F = \hbar k_F v_F = \pm \hbar v_F \sqrt{\pi |n|}, \quad (4.8)$$

where $k_F = \sqrt{\pi |n|}$ is the Fermi wave vector, v_F is the carrier Fermi velocity and “+” and “-” signs stand for electrons and holes, respectively. In the figure, well-developed plateaus in ρ_{xy} appear with striking precisions in a sequence of $\rho_{xy} = h/\nu e^2$, where $\nu = -10, -6, -2, 2, 6$ and 10 . Simultaneously, ρ_{xx} vanishes due to the suppression of back-scattering when E_F is located in a gap of the LL spectrum [14]. The sign change in ρ_{xy} across the charge neutrality point (which is ~ 0.5 V in V_{bg}) reflects that the carrier type changes.

Magneto-conductivities as a function of the back-gate voltage were obtained by using Eq. 4.4 and 4.5. They are plotted in Fig. 4.3(a). Fig. 4.3(b) schematically illustrates the formation of the quantum Hall plateaus in graphene through localization-delocalization transitions. During the back-gate sweep (from $V_{bg} = -60$ V to 60 V), electronic states in the broadened LLs are gradually filled up. When E_F moves in the region of localized states (i.e. in the mobility gap), there is no conductivity in the longitudinal direction and the occupation of the extended states remains unchanged [15, 16]. Since the electric current is only carried by these extended states, the Hall conductivity will remain constant and hence give rise to a quantum Hall plateau. On the other hand, when E_F

reaches the vicinity of the next LL, dissipation occurs in the system and the Hall conductivity quickly changes to the next plateau.

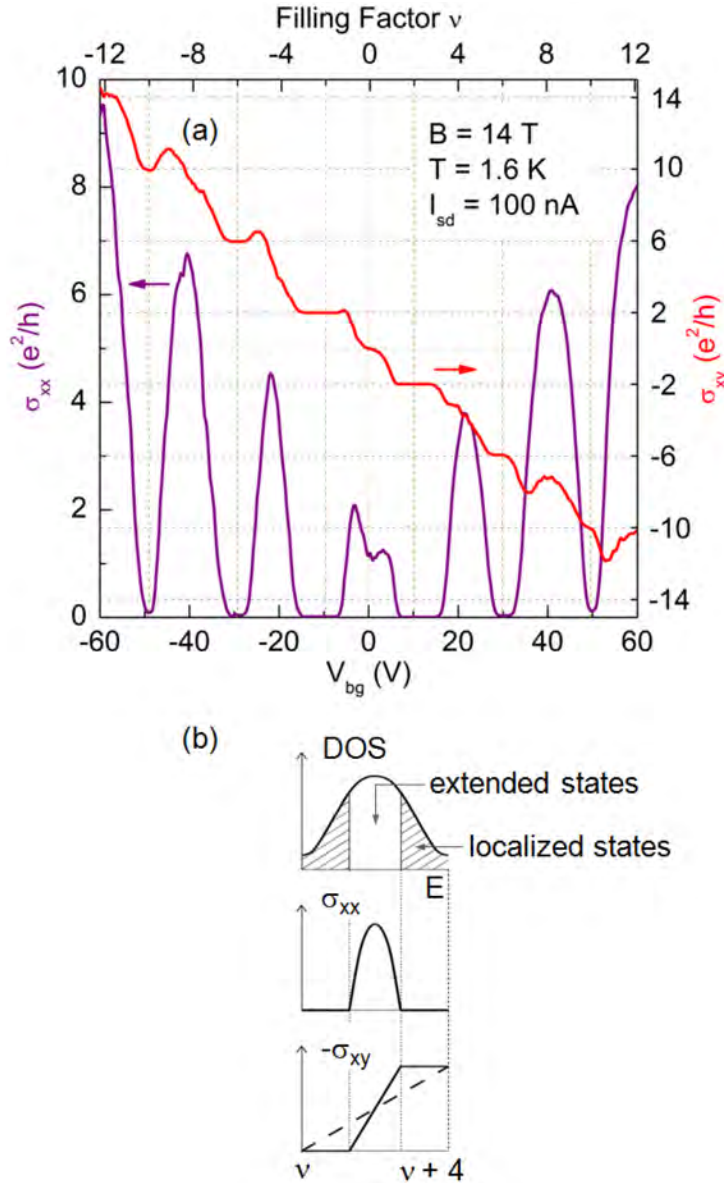


Figure 4.3: (a) Magneto-conductivities as a function of the back-gate voltage V_{bg} as well as the filling factor ν for the device in Fig. 4.2. The longitudinal conductivity σ_{xx} and the Hall conductivity σ_{xy} are calculated according to Eq. 4.4 and Eq. 4.5, respectively. Clearly, quantum Hall states in the graphene sample occur at filling factors in accordance with $\nu = \pm 4(|N| + 1/2)$, where N is the Landau level index. Note the developing-plateau-like structure in σ_{xy} at $\nu \sim 0$. (b) Schematic diagram for the process of localization-delocalization transitions in graphene during the back-gate sweep. Fermi energy E_F in graphene is being shifted as carrier density changes. When E_F moves in the region of localized states, σ_{xx} vanishes while σ_{xy} keeps constant, hence giving rise to a quantum Hall plateau. When E_F reaches the delocalized states of the next LL, however, σ_{xx} becomes finite and σ_{xy} quickly changes to the next plateau.

In Fig. 4.3(a), the quantization of σ_{xy} occurs at integer filling factors with unconventional sequence (compared to the QHE sequences in regular 2DES) of

$$\sigma_{xy} = -\nu \frac{e^2}{h} = \pm 4 \left(|N| + \frac{1}{2} \right) \frac{e^2}{h}. \quad (4.9)$$

Here, N is the LL index (integer). A positive (negative) filling factor ν corresponds to electrons (holes). The factor “4” in the expression accounts for double spin degeneracy and double sub-lattice degeneracy (i.e. the two inequivalent Dirac valleys in the band dispersion of graphene; see Chapter 1), while the additional “1/2” in Eq. 4.9 shows that the QHE sequence in graphene is shifted with respect to the standard ones in regular 2DES by 1/2 [1-3, 17]. This odd factor “1/2” can be understood as arising from the existence of the unique zeroth LL at zero energy in graphene, which is equally shared by electrons and holes [1-3, 13]. Or otherwise stated, the lowest LL in the conduction band and the highest LL in the valence band merge and hence contribute equally to the zero energy mode. It reflects the particle-hole symmetry in graphene [17].

A closer examination of Fig. 4.3(a) reveals that a plateau in σ_{xy} develops at $\nu = 0$. It is accompanied also by a dip in σ_{xx} , as well as a kink feature in ρ_{xy} near the charge neutrality point in Fig. 4.2(a). This developing plateau at $\nu = 0$ is only observed in high-quality samples, and is found to be better developed at lower excitation current probably because the associated energy gap is small and heating has to be avoided [18-20]. Fig. 4.4(a) shows σ_{xy} vs. V_{bg} at various current biases for the sample in Fig. 4.2. At $I_{sd} = 1$ nA, the plateau region extends for over 2 V in V_{bg} . The fluctuations with low amplitude on this $\nu = 0$ plateau are believed to originate from the fluctuations in ρ_{xy} in the close vicinity of the charge neutrality point (Fig. 4.4(b)). We suspect that the random network of electron-hole puddles [21-23] at very low average carrier densities is responsible for these noise-

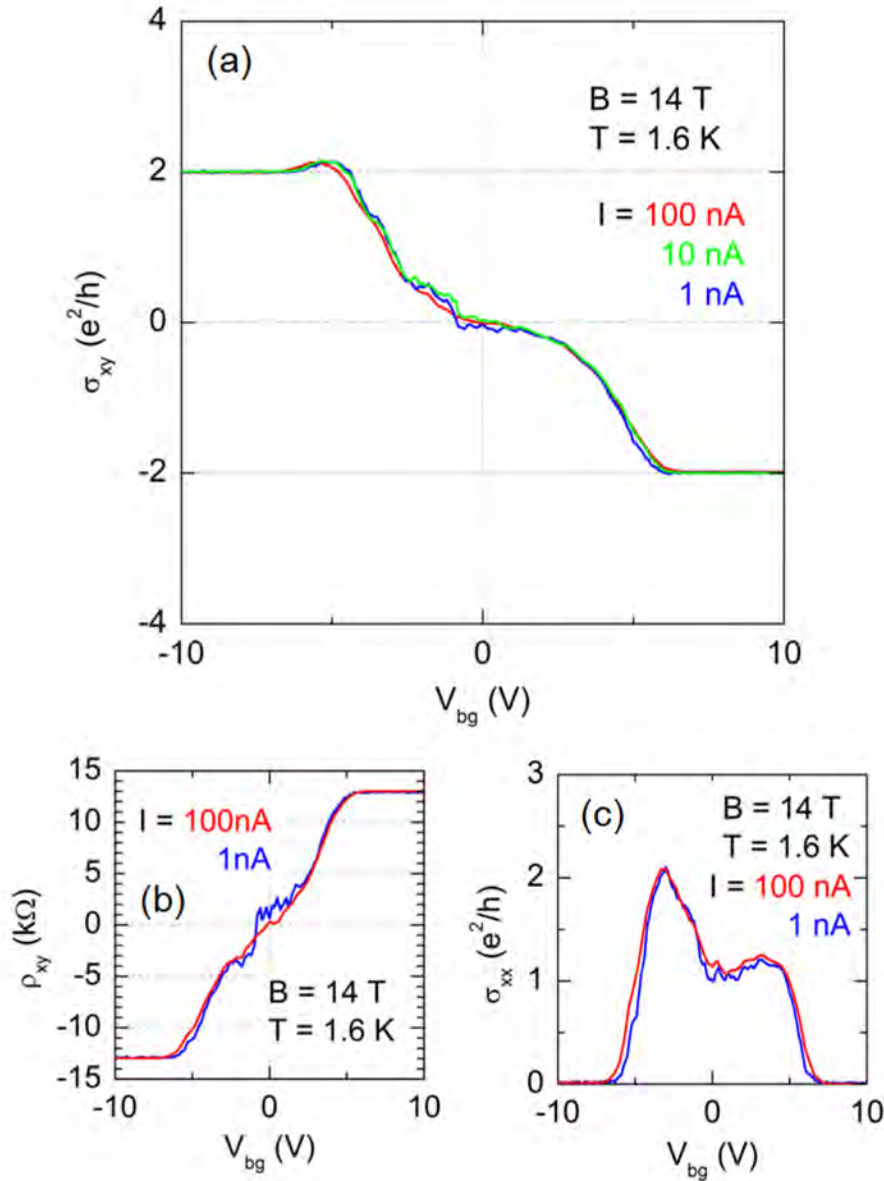


Figure 4.4: Evolution of σ_{xy} (a), ρ_{xy} (b) and σ_{xx} (c) at $\nu \sim 0$ with reduced excitation current. The plateau-like feature in σ_{xy} at $\nu = 0$ at $I_{sd} = 1$ nA has a width of above 2 V. σ_{xx} at $\nu = 0$ shows a trend of approaching zero when the current decreases.

like features. The behavior of σ_{xx} at $I_{sd} = 1$ nA is depicted in Fig. 4.4(c). The dip near zero carrier density approaches 0 further when the amplitude of the excitation current is reduced. This trend has been verified by sub-nA measurements with the setup shown in Fig. 4.1(b). In the literature, data were reported at higher magnetic fields and/or lower

temperatures [18-20, 24]. This brought σ_{xx} at $\nu = 0$ closer to zero. The quantum Hall state at $\nu = 0$ originates either from a lifting of the spin or valley degeneracy. This is still debated continuously in the literature [18-20, 24-26].

The QHE can also be observed by sweeping the magnetic field B while keeping the carrier density in the graphene layer constant, as depicted in Fig. 4.5(a). ρ_{xy} plateaus corresponding to filling factors -6, -10, -14, -18, -22, -26, ... are resolved for the device shown in Fig. 4.5(b). The magneto-oscillations (Shubnikov-de Haas oscillations, SdHOs) in ρ_{xx} are essentially due to the successive depopulation of LLs with increasing B . ρ_{xx} goes through one cycle as the Fermi energy E_F moves from the center of one LL to the center of the next LL (or alternatively, from the center of one mobility gap to the center of the next mobility gap) [27]. Hence, one magneto-oscillation in graphene corresponds to a change of 4 in the filling factor under the assumption that spin and valley degeneracies are not lifted.

Fig. 4.5(c) highlights the linear part of ρ_{xy} vs. B at low magnetic fields in Fig. 4.5(a). It resembles the behavior of a classical Hall effect, where one may assume the equilibrium between the electric force and Lorentz force on a point charge moving in the direction of the current flow. The slope of ρ_{xy} yields an estimate for the carrier density in the 2DES according to the relation

$$\rho_{xy} = R_{xy} = \frac{V_{xy}}{I_{sd}} = \frac{B}{en}. \quad (4.10)$$

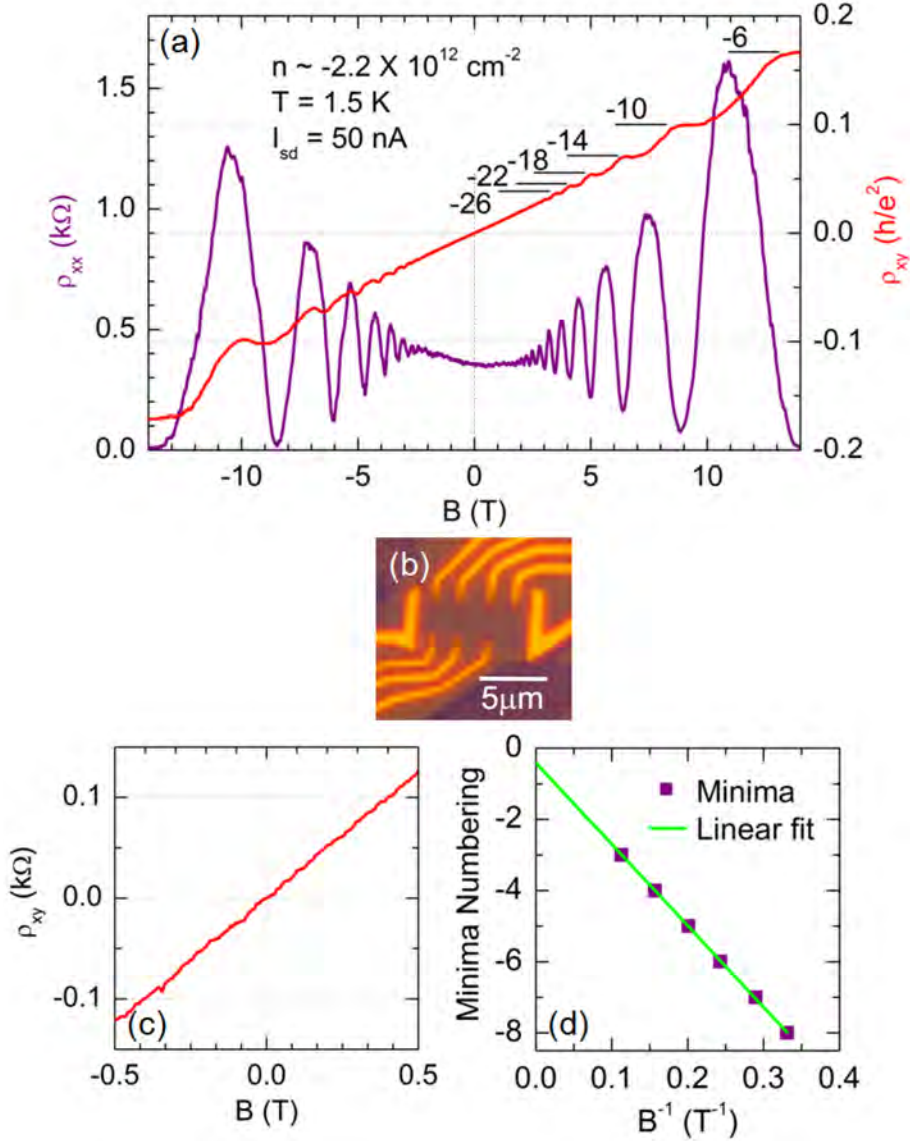


Figure 4.5: (a) Graphene longitudinal and Hall resistivities as a function of the magnetic field at a fixed carrier density of $\sim 2.2 \times 10^{12} \text{ cm}^{-2}$. Quantum Hall plateaus corresponding to such filling factors as -6, -10, -14, -18, -22, -26 ... (indicated in the plot) are unambiguously resolved. The optical image of the sample is shown in (b). The classical Hall effect in $\rho_{xy}(B)$ at low magnetic fields is highlighted in (c). (d) Numbering of successive local minima in $\rho_{xx}(B)$ oscillations in (a) as a function of the inverse magnetic field at which the minima occur. The slope is proportional to the carrier density and follows from Eq. 4.12.

Fig. 4.5(d) demonstrates the procedure for the estimation of carrier density in graphene based on the periodicity in the SdHOs in Fig. 4.5(a). For the filling factors corresponding to two successive local minima (or maxima) in the SdHO curve, we have

$$|v_1 - v_2| = \left| \frac{hn}{eB_1} - \frac{hn}{eB_2} \right| = 4, \quad (4.11)$$

and this yields

$$\left| \Delta \left(\frac{1}{B} \right) \right| = \left| \frac{1}{B_1} - \frac{1}{B_2} \right| = \frac{4e}{h|n|}. \quad (4.12)$$

Therefore, we plot the positions of the successive minima in ρ_{xx} as a function of the inverse magnetic field as shown in Fig. 4.5(c). The period of the SdHOs is extracted from the slope. We then obtain a carrier density of $\sim 2.2 \times 10^{12} \text{ cm}^{-2}$ for graphene. This agrees well with a thickness of $\sim 280 \text{ nm}$ for the SiO_2 layer right underneath the graphene sheet (by assuming the dielectric constant of SiO_2 to be 3.9). The thickness of SiO_2 is further confirmed by an independent ellipsometry measurement. The agreement justifies the simple parallel-plate capacitor model introduced in Chapter 3. Alternatively, one can apply a Fourier transform to the original ρ_{xx} (when plotted on an inverse B axis) to extract the period of the SdHOs.

4.3 The robust $\nu = 2$ quantum Hall state

When the current injected into a Hall-bar-shaped 2DES in the quantum Hall regime exceeds a certain critical value, the transport is no longer dissipationless and ρ_{xx} takes on a finite value instead of being zero. This is referred to as the breakdown of the QHE [15]. The magnitude of this breakdown current I_C is important for metrology applications, where Hall resistance under quantum Hall conditions is used as the resistance standard. The precision of this type of quantum resistance standard is, however, subject to the observed linear relation

$$\Delta\rho_{xy} = s\rho_{xx}, \quad (4.13)$$

where $\Delta\rho_{xy}$ is the deviation of the Hall resistivity from its ideally quantized value, and s is a proportionality factor varying between -0.01 and -1.1 [15, 28].

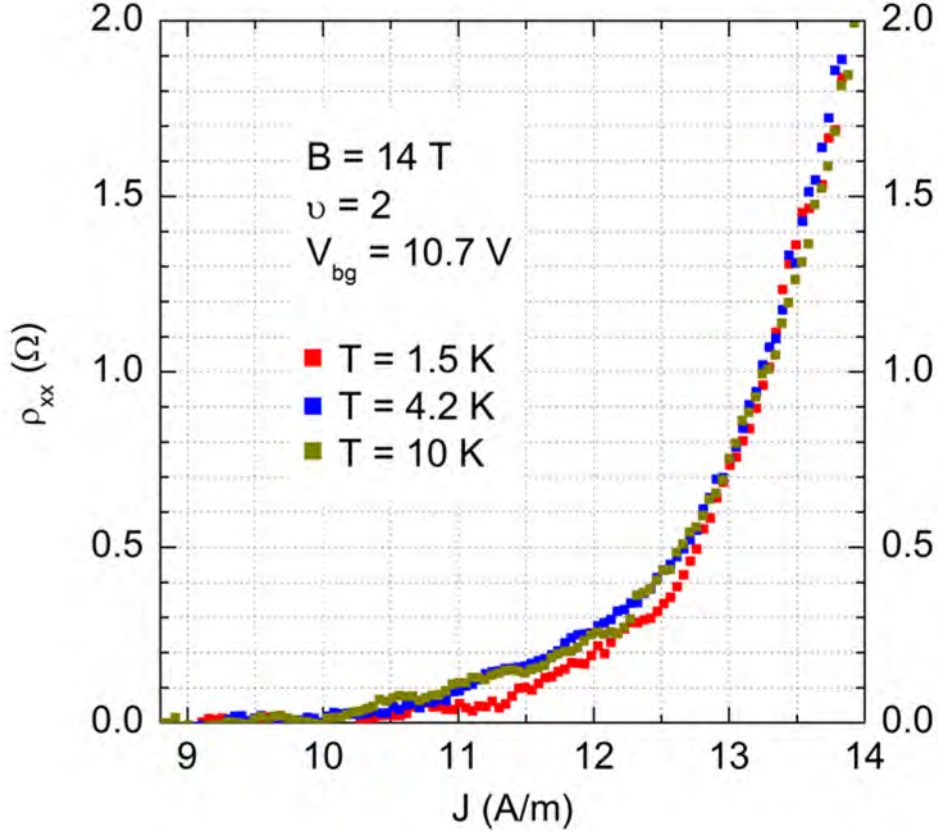


Figure 4.6: Current density dependence of the longitudinal resistivity for the $\nu = 2$ quantum Hall state at various temperatures (for the device in Fig. 4.5). When the current density J exceeds ~ 13 A/m, ρ_{xx} increases rapidly with J . The critical current density J_C signaling the breakdown of the quantum Hall effect is ~ 11 A/m if $\rho_{xx} > 0.1 \Omega$ [29] is used as the breakdown criterion. Between 1.5 K and 10 K, J_C shows a weak temperature dependence.

Fig. 4.6 depicts the current density dependence of ρ_{xx} for the $\nu = 2$ plateau of the graphene sample in Fig. 4.5 at a magnetic field of 14 T. In order to compare our data to the reported ones [29] in conventional 2DES, we adopt $\rho_{xx} \geq 0.1\Omega$ as the criterion (which is somewhat arbitrary) for the breakdown of the QHE in graphene. The critical current density J_C is found to be about 11 A/m for the $\nu = 2$ quantum Hall state at $B = 14$ T, with

a rather weak temperature dependence between 1.5 K and 10 K. We notice that for the same magnetic field this J_C in our graphene sample is several times higher than the measured values in conventional 2DES [15].

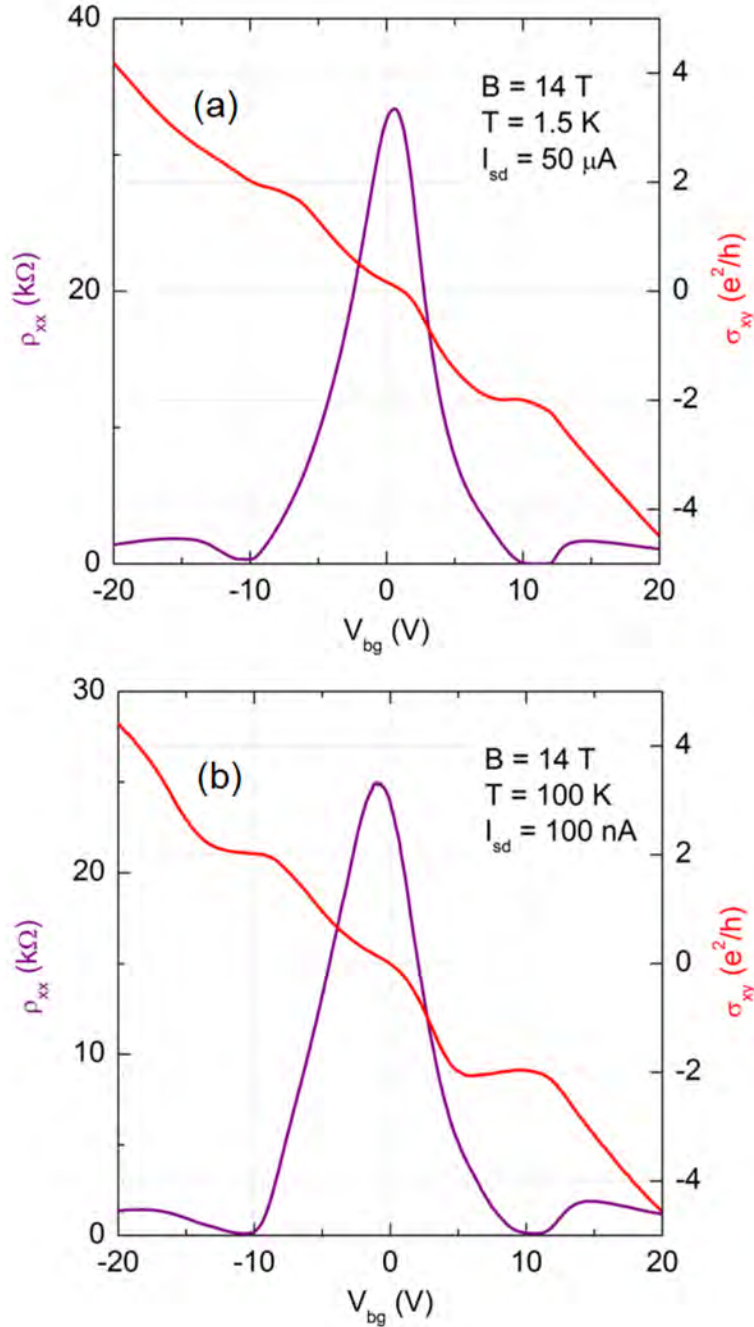


Figure 4.7: (a) Quantum Hall effect (in the device in Fig. 4.5) at a DC excitation current as high as $50 \mu A$ (or equivalently, at a current density of ~ 14 A/m). (b) QHE in the same device at a temperature of 100 K. In both cases, the $\nu = 2$ plateau in σ_{xy} is well resolved and the corresponding ρ_{xx} remains close to zero, indicating a robust QH state at $\nu = 2$ in graphene.

To further test the robustness of the $\nu = 2$ quantum Hall state in graphene, we carried out magneto-transport measurements at higher temperatures and/or with very large excitation currents. Fig. 4.7(a) and (b) show the large-current QHE with $I_{sd(DC)} = 50 \mu\text{A}$ (corresponding to a current density of $\sim 14 \text{ A/m}$) and high-temperature QHE at $T = 100 \text{ K}$, respectively. In either case, the quantum Hall plateau at $\nu = 2$ is well resolved, and the corresponding ρ_{xx} is vanishingly small. The survival of the $\nu = 2$ QHE in graphene to these “extreme” conditions can probably be attributed to the large LL energy spacing between the zeroth and the first LLs in a moderate magnetic field. The observed extraordinarily robust QHE at $\nu = 2$ suggests that graphene is an excellent candidate material for the quantum resistance standard.

References

- [1] Y. Zheng and T. Ando, *Hall conductivity of a two-dimensional graphite system*, Physical Review B **65**, 245420 (2002).
- [2] V. P. Gusynin and S. G. Sharapov, *Unconventional integer quantum Hall effect in graphene*, Physical Review Letters **95**, 146801 (2005).
- [3] N. M. R. Peres, F. Guinea, and A. H. Castro Neto, *Electronic properties of disordered two-dimensional carbon*, Physical Review B **73**, 125411 (2006).
- [4] K. S. Novoselov, A. K. Geim, S. V. Morozov, D. Jiang, M. I. Katsnelson, I. V. Grigorieva, S. V. Dubonos, and A. A. Firsov, *Two-dimensional gas of massless Dirac fermions in graphene*, Nature **438**, 197-200 (2005).
- [5] Y. Zhang, Y. W. Tan, H. L. Stormer, and P. Kim, *Experimental observation of the quantum Hall effect and Berry's phase in graphene*, Nature **438**, 201-204 (2005).
- [6] R. B. Laughlin, *Quantized Hall conductivity in two dimensions*, Physical Review B **23**, 5632 (1981).
- [7] W. Poirier, F. Schopfer, J. Guignard, O. Thévenot, and P. Gournay, *Application of the quantum Hall effect to resistance metrology*, Comptes Rendus Physique **In Press, Corrected Proof**, (2011).
- [8] B. I. Halperin, *Quantized Hall conductance, current-carrying edge states, and the existence of extended states in a two-dimensional disordered potential*, Physical Review B **25**, 2185 (1982).
- [9] P. J. Mohr, B. N. Taylor, and D. B. Newell, *CODATA recommended values of the fundamental physical constants: 2006*, Reviews of Modern Physics **80**, 633 (2008).

- [10] K. v. Klitzing, G. Dorda, and M. Pepper, *New method for high-accuracy determination of the fine-structure constant based on quantized Hall resistance*, Physical Review Letters **45**, 494 (1980).
- [11] P. R. Wallace, *The band theory of graphite*, Physical Review **71**, 622 (1947).
- [12] C. W. J. Beenakker and H. van Houten, *Quantum transport in semiconductor nanostructures*, Solid State Physics **44**, 1-228 (1991).
- [13] A. K. Geim and K. S. Novoselov, *The rise of graphene*, Nature Materials **6**, 183-191 (2007).
- [14] M. Büttiker, *Absence of backscattering in the quantum Hall effect in multiprobe conductors*, Physical Review B **38**, 9375 (1988).
- [15] B. Jeckelmann and B. Jeanneret, *The quantum Hall effect as an electrical resistance standard*, Reports on Progress in Physics **64**, 1603 (2001).
- [16] L. Sheng, D. N. Sheng, F. D. M. Haldane, and L. Balents, *Odd-integer quantum Hall effect in graphene: interaction and disorder effects*, Physical Review Letters **99**, (2007).
- [17] S. Das Sarma, S. Adam, E. H. Hwang, and E. Rossi, *Electronic transport in two-dimensional graphene*, Reviews of Modern Physics **83**, 407 (2011).
- [18] J. G. Checkelsky, L. Li, and N. P. Ong, *Zero-energy state in graphene in a high magnetic field*, Physical Review Letters **100**, 206801 (2008).
- [19] A. J. M. Giesbers, L. A. Ponomarenko, K. S. Novoselov, A. K. Geim, M. I. Katsnelson, J. C. Maan, and U. Zeitler, *Gap opening in the zeroth Landau level of graphene*, Physical Review B **80**, 201403 (2009).
- [20] L. Zhang, Y. Zhang, M. Khodas, T. Valla, and I. A. Zaliznyak, *Metal to insulator transition on the $n=0$ Landau level in graphene*, Physical Review Letters **105**, 046804 (2010).

- [21] E. H. Hwang, S. Adam, and S. D. Sarma, *Carrier transport in two-dimensional graphene layers*, Physical Review Letters **98**, 186806 (2007).
- [22] J. Martin, N. Akerman, G. Ulbricht, T. Lohmann, J. H. Smet, K. von Klitzing, and A. Yacoby, *Observation of electron-hole puddles in graphene using a scanning single-electron transistor*, Nature Physics **4**, 144 (2008).
- [23] Y. Zhang, V. W. Brar, C. Girit, A. Zettl, and M. F. Crommie, *Origin of spatial charge inhomogeneity in graphene*, Nature Physics **5**, 722-726 (2009).
- [24] Z. Jiang, Y. Zhang, H. L. Stormer, and P. Kim, *Quantum Hall states near the charge-neutral dirac point in graphene*, Physical Review Letters **99**, 106802 (2007).
- [25] K. Nomura and A. H. MacDonald, *Quantum Hall ferromagnetism in graphene*, Physical Review Letters **96**, 256602 (2006).
- [26] S. Das Sarma and K. Yang, *The enigma of the $\nu=0$ quantum Hall effect in graphene*, Solid State Communications **149**, 1502-1506 (2009).
- [27] S. Datta, *Electronic transport in mesoscopic systems* (Cambridge University Press, 1995), pp. 26.
- [28] K. Yoshihiro, J. Kinoshita, K. Inagaki, C. Yamanouchi, J. Moriyama, and S. Kawaji, *Quantized Hall and transverse resistivities in silicon MOS n-inversion layers*, Physica B+C **117-118**, 706-708 (1983).
- [29] S. Kawaji, *Breakdown of the integer quantum Hall effect at high currents in GaAs/AlGaAs heterostructures*, Semicond. Sci. Technol. **11**, 1546 (1996).

Chapter 5

Transport in gate-controlled graphene p - n junctions

In this chapter, we report on four-terminal transport measurements in high-quality bipolar graphene devices featuring a hybrid top-gate dielectric. Electric fields applied by a global back-gate and a local top-gate enable independent control over the carrier type and density in two adjacent regions of the graphene sheet. The charge density in either of the regions can be varied across the charge neutrality point, allowing p - n (or n - p), p - p and n - n junctions to be formed at the interface. The local potentials on the two sides of the junction can be probed by multiple voltage contacts. The observed characteristic quantization of both the Hall and longitudinal resistances in a perpendicular magnetic field provides direct evidence for the equilibration of edge states at the p - n interface under quantum Hall conditions. Our experimental results are in excellent quantitative agreement with the Landauer-Büttiker formula [1] and the mode mixing model [2]. We also discuss the electrical characterizations on graphene p - n - p devices featuring an extremely thin (< 5 nm) h-BN (hexagonal boron nitride) top-gate dielectric that is prepared by a precise transfer of exfoliated h-BN films. The top gate is found to possess a very high coupling efficiency and a rather low leakage current.

5.1 Sample preparation and measurement setup

The hybrid top-gate dielectric comprising oxidized Al and evaporated SiO_2 is prepared according to the description in section 2.3.4. Fig. 5.1(a) shows the optical micrograph of a completed bipolar graphene sample with assigned electrical leads. A cross-section of the dual-gated device and the electrical biasing of the two gates (i.e. the local top-gate and the global Si back-gate) are illustrated in Fig. 5.1(b). The transport measurements are carried out in a four-terminal configuration as schematically represented in Fig. 5.1(c).

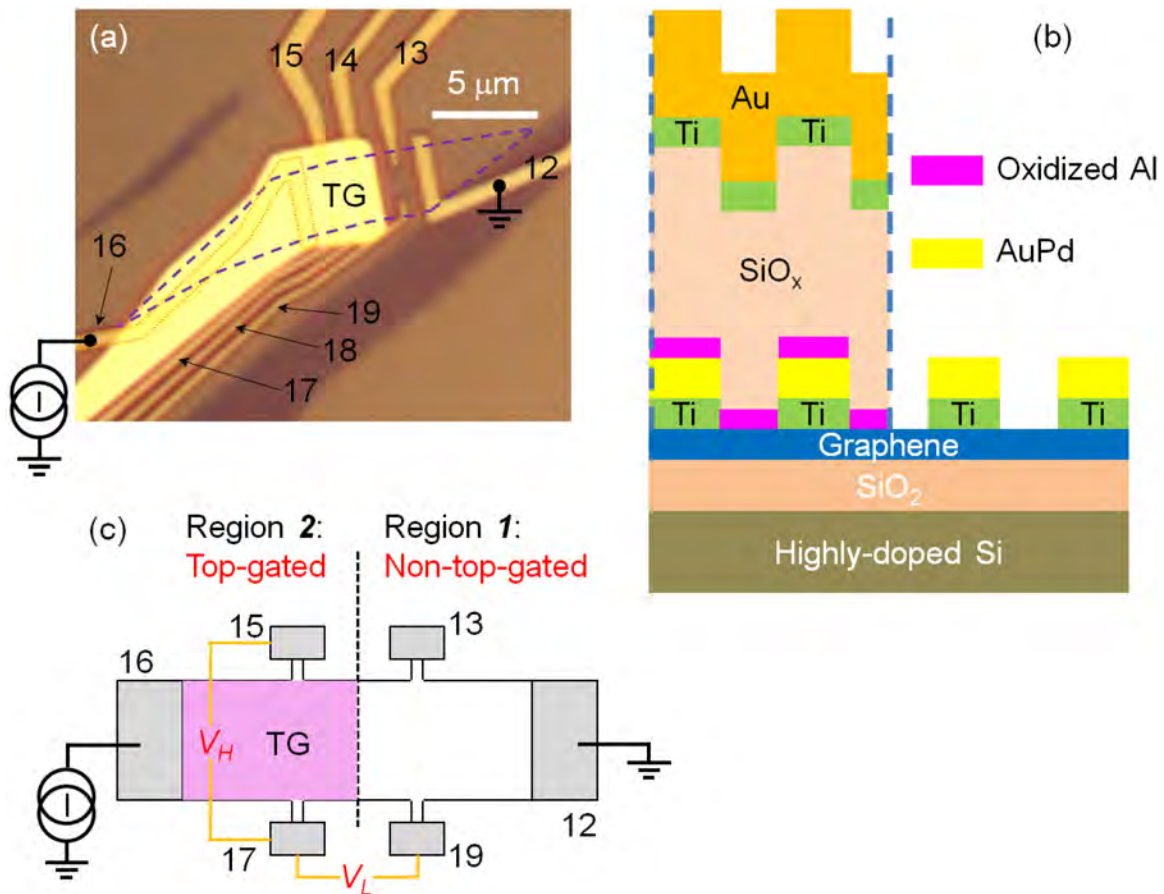


Figure 5.1: (a) Optical image of a double-gated graphene device. The assignment of the electrical leads has been included. The purple dashed line highlights the edge of the graphene sheet, while the gold dotted line indicates one of the source/drain electrodes. (b) Cross-section view of the dually gated device in (a). (c) Schematic of the four-terminal measurement setup for the device in (a). V_H (V_{15-17}) and V_L (V_{17-19}) stand for Hall voltage (in magneto-transport measurements) and longitudinal voltage, respectively.

The bipolar graphene samples are cooled in a ^4He cryostat. They are characterized at a temperature $T \sim 1.5$ K. The resistances are measured by the standard lock-in technique with a current bias of $100 \text{ nA}_{\text{rms}}$ at 23.87 Hz. The top- and back-gate voltages are supplied by Yokogawa DC sources.

5.2 Four-terminal transport at zero magnetic field

For the dual-gated device in Fig. 5.1(a), Fig. 5.2(a) shows the two-dimensional (2D) color map of the longitudinal resistance ($R_L = R_{17-19} = V_{17-19} / I$) as a function of the top gate (V_{tg} , horizontal axis) and back gate voltage (V_{bg} , vertical axis) at zero magnetic field ($B = 0$ T). The horizontal band centered around $V_{bg} \sim 0.8$ V marks the charge neutrality point in the region without a top gate (region 1), while the diagonal band corresponds to the local resistance maxima in the top-gated region (region 2). These two bands divide the parameter space into four different quadrants of well-defined carrier types in the top-gated and non-top-gated regions of the graphene sample. The crossing of the bands at $(V_{tg}, V_{bg}) \cong (-2.8 \text{ V}, 0.8 \text{ V})$ indicates the position of the global charge neutrality point, where the resistance across the entire graphene sheet reaches the maximum. The small deviation of the center of the horizontal band from zero back gate voltage indicates a low chemical-doping level in graphene after annealing.

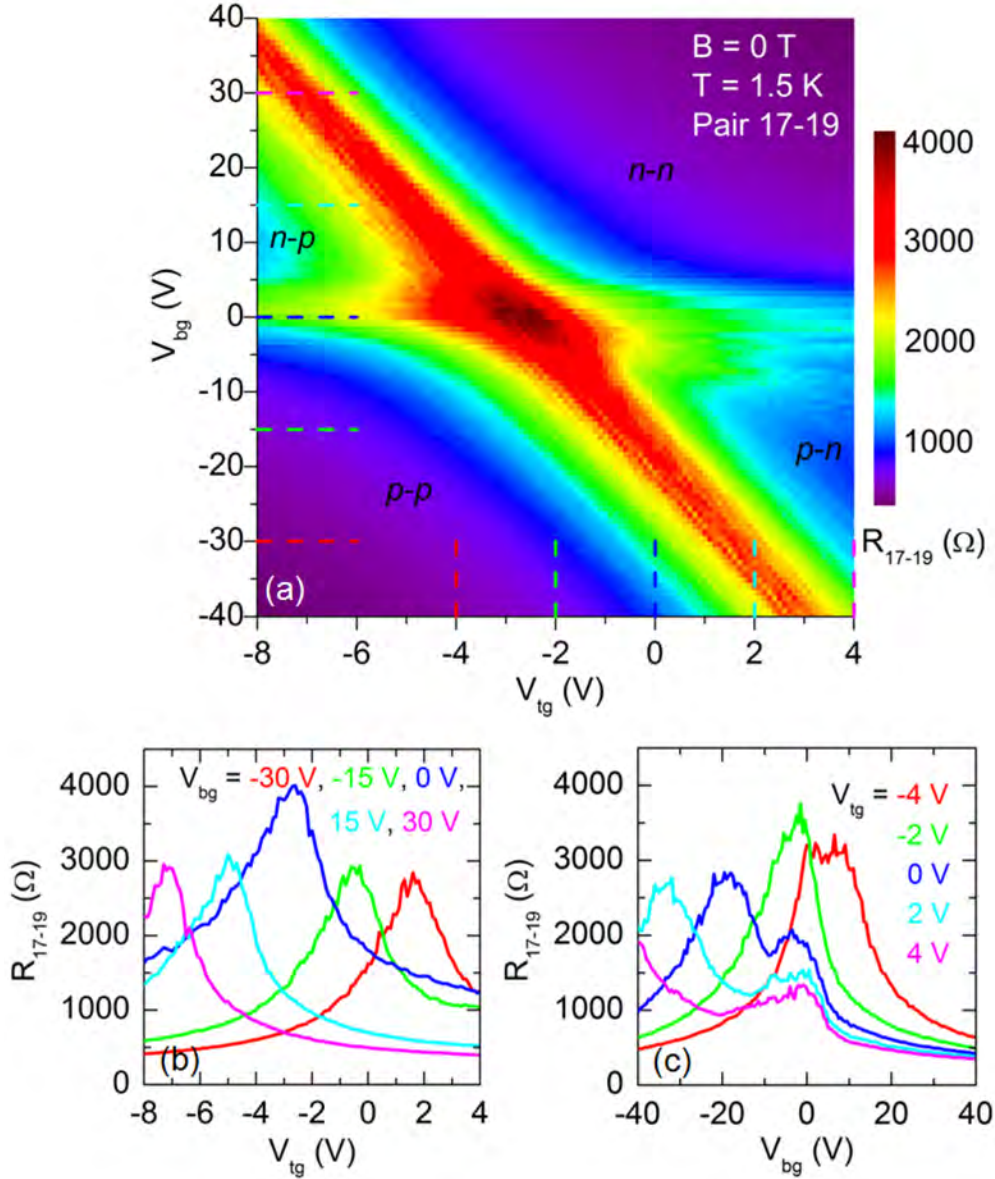


Figure 5.2: (a) Two-dimensional color plot of the longitudinal resistance R_{17-19} as a function of gate voltages at $B = 0$ T and $T = 1.5$ K, manifesting independent control over the carrier type and density in region 1 (i.e. the non-top-gated part) and 2 (the top-gated part) of the graphene sheet. The carrier types are labeled in each of the four quadrants. The first letter corresponds to the carrier type in region 1. (b) $R_L(V_{tg})$ extracted from (a) at $V_{bg} = -30, -15, 0, 15$ and 30 V. (c) $R_L(V_{bg})$ extracted from (a) at $V_{tg} = -4, -2, 0, 2$ and 4 V.

Fig. 5.2(b) shows R_L as a function of V_{tg} at several fixed back-gate voltages. These horizontal cuts through Fig. 5.2(a) exhibit a single asymmetric peak. This peak corresponds to the charge neutrality point in the top-gated region (region 2). Fig. 5.2(c)

plots R_L versus V_{bg} at five fixed V_{tg} . These curves correspond to the vertical cuts through the 2D map in Fig. 5.2(a). Slices for $V_{tg} \geq 0$ V clearly manifest a double-peak feature that reveals the presence of two charge neutrality points across the graphene sheet. In this case, the weaker peak, which remains close to $V_{bg} \sim 0.8$ V at all V_{tg} , corresponds to the charge neutrality point of region 1 (non-top-gated region). The stronger peak, which moves linearly with V_{tg} , is the charge neutrality point of region 2 (top-gated region). The differences in peak height reflect the different length-to-width ratios of the regions with and without top-gating between potential probes 17 and 19.

Electric fields applied by the back and top gates allow independent control over the carrier type and density in region 1 and 2 of the graphene sheet. From simple geometry consideration, the average carrier density in region 1 (non-top-gated part) is given by [3] (see also chapter 3):

$$n_1 = \frac{C_{bg}(V_{bg} - V_{bg}^0)}{e}, \quad (5.1)$$

where C_{bg} is the back gate capacitance (per unit area) and V_{bg}^0 is the charge neutrality point in region 1 (~ 0.8 V in this case). In region 2, the average carrier density is modulated by both the back gate and top gate according to:

$$n_2 = n_1 + \frac{C_{tg}(V_{tg} - V_{tg}^0)}{e} \quad (5.2)$$

where C_{tg} is the top gate capacitance (per unit area), and V_{tg}^0 is the (top-gate) charge neutrality point in region 2 when $V_{bg} \sim 0.8$ V ($V_{tg}^0 \approx -2.8$ V for the sample in Fig. 5.1(a)).

It is assumed in Eq. 5.2 that the top-gated region has the same V_{bg}^0 as the non-top-gated part, and this assumption is justified by the existence of the (single) global neutrality

point where both n_1 and n_2 vanish. Obviously, the horizontal band in Fig. 5.2(a) is defined by letting $n_1 = 0$ in Eq. 5.1, while $n_2 = 0$ in Eq. 5.2 renders the diagonal one. The slope η of this skewed line yields the ratio of the coupling efficiencies of the two gates to the graphene sheet with $\eta = C_{tg} / C_{bg} \approx 7.0$. Since the gate capacitive coupling C is defined by

$$C = \frac{\epsilon_0 \epsilon_r}{d}, \quad (5.3)$$

where ϵ_0 is the permittivity of free space, ϵ_r is the dielectric constant of the gate dielectric and d is the thickness of the dielectric layer, the ratio of the coupling efficiencies equals:

$$\eta = \frac{\epsilon_{tg}}{\epsilon_{bg}} \cdot \frac{d_{bg}}{d_{tg}} \approx 7.0, \quad (5.4)$$

where d_{bg} and ϵ_{bg} are the thickness and dielectric constant of back-gate dielectric (~ 300 nm thick dry-oxidized SiO_2 with $\epsilon_{bg} \sim 3.9$ in this case), and d_{tg} and ϵ_{tg} are the top-gate counterparts of d_{bg} and ϵ_{bg} . We estimate d_{tg} to be around 43 nm (which has been calibrated in other samples fabricated with exactly the same procedure); by placing these numbers in Eq. 5.4 we obtain $\epsilon_{tg} \sim 3.9$. This value is very reasonable considering the fact that the hybrid top-gate dielectric comprises thermally deposited SiO_x ($x \rightarrow 2$) and a very thin (1-2 nm thick) layer of oxidized Al (the dielectric constant of Al_2O_3 is about 9).

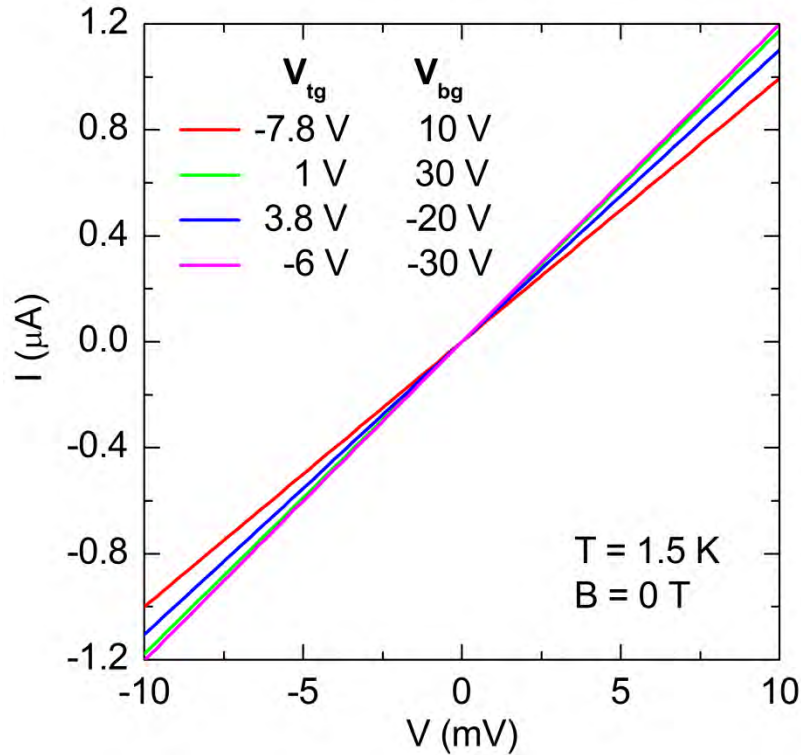


Figure 5.3: I - V plots at the gate voltage settings $(V_{tg}, V_{bg}) = (-7.8\text{V}, 10\text{V})$, $(1\text{V}, 30\text{V})$, $(3.8\text{V}, -20\text{V})$ and $(-6\text{V}, -30\text{V})$. These four points are randomly picked out from each of the four quadrants in Fig. 5.2(a). The ohmic I - V behavior here represents the linear characteristics throughout the whole (V_{tg}, V_{bg}) plane.

Fig. 5.3 depicts the current-voltage (I - V) characteristics measured between the source and drain contacts at various (V_{tg}, V_{bg}) combinations in a two-terminal configuration. The I - V traces are linear and show no sign of rectification (which is seen in conventional Si p - n diodes) in any of the four quadrants in the (V_{tg}, V_{bg}) -parameter space or at either of the charge-neutral ridges between quadrants. This type of ohmic behavior does not come as a surprise. Graphene is a gapless material with a linear energy-momentum dispersion relation at low energies. The conservation of the pseudospin degree of freedom allows reflectionless (“Klein”) tunneling at the p - n interface independent of the height and width of the potential barrier [4-8] (see also chapter 1). By comparing the resistance values to those obtained by four-terminal measurements, we estimate the contact resistance at the

interface between the source/drain metal contacts and the graphene sheet to be close to 1 k Ω .

5.3 Four-terminal transport in the quantum Hall regime

In this sub-chapter, discussions are focused on four-terminal magneto-resistances in such a dual-gated graphene device as shown in Fig. 5.1(a) under quantum Hall conditions.

In a doubly gated graphene sheet, the quantum Hall edge modes can propagate along or across the “ p - n ” interface, depending on whether the device operates in the bipolar or unipolar regime [2]. The propagating direction of the edge states is determined by the direction of the external magnetic field and the carrier type. In the bipolar regime, edge modes in the p and n sides of the graphene layer travel in the opposite directions along one edge of the carbon sheet until they meet at the p - n boundary. Then all the modes move (in the same direction) along the interface, where mode mixing (i.e. equilibration of the electrochemical potential) and energy dissipation occur. The scenario is rather different when a double-gated graphene device operates in the unipolar regime. In this case, the quantum Hall edge states in the top-gated and non-top-gated regions circulate in the same direction, and the conductance between the source and drain electrodes is determined by the modes that permeate the whole graphene layer[2]. Reported experiments on a two-terminal graphene p - n junction [6] showed that its conductance under the quantum Hall conditions can be adequately interpreted within the Landauer-Büttiker formalism.

Here we employ a four-terminal setup to examine the picture of mode mixing/transmission at the “ p - n ” interface in the quantum Hall regime. Local voltage

probes on the two sides of the junction not only eliminate the measurement uncertainties caused by contact resistances, but also allow us to study the nature of mode propagation/interaction by monitoring the local potentials along the two edges of the graphene layer across the “*p-n*” boundary.

For the sample in Fig. 5.1(a) in a perpendicular magnetic field of 14 T, Fig. 5.4 shows the calculated Hall resistance R_H (for the sake of simplicity, only the corresponding filling factor numbers ν in $R_H = h/\nu e^2$ are displayed) as a function of the gate voltages in the quantum Hall regime. R_H in the non-top-gated and top-gated regions is denoted by the first and second filling factor numbers, respectively. The boundaries of various quantum Hall parallelograms in the parameter space of gate voltages are defined by a set of horizontal and skewed lines. These lines correspond to such filling factor values as 0, ± 4 , $\pm 8 \dots$ on the two sides of the graphene junction. For region 1 (i.e. the part of the graphene sheet without top-gating), the filling factor ν_1 is given by

$$\nu_1 = \frac{n_1 h}{eB} = \frac{h C_{bg} (V_{bg} - V_{bg}^0)}{e^2 B}, \quad (5.5)$$

where B is the perpendicular magnetic field and n_1 is the carrier density. For the filling factor ν_2 in region 2 (with top-gating), similarly we have:

$$\nu_2 = \frac{n_2 h}{eB} = \frac{h}{e^2 B} \left[C_{bg} (V_{bg} - V_{bg}^0) + \eta C_{bg} (V_{tg} - V_{tg}^0) \right]. \quad (5.6)$$

By letting $\nu_{1,2} = 0, \pm 4, \pm 8 \dots$ in Eq. 5.5 and 5.6 (C_{bg} , η , V_{bg}^0 and V_{tg}^0 are all already known), we specify the boundaries of the quantum Hall regions and thus obtain the pattern shown in Fig. 5.4.

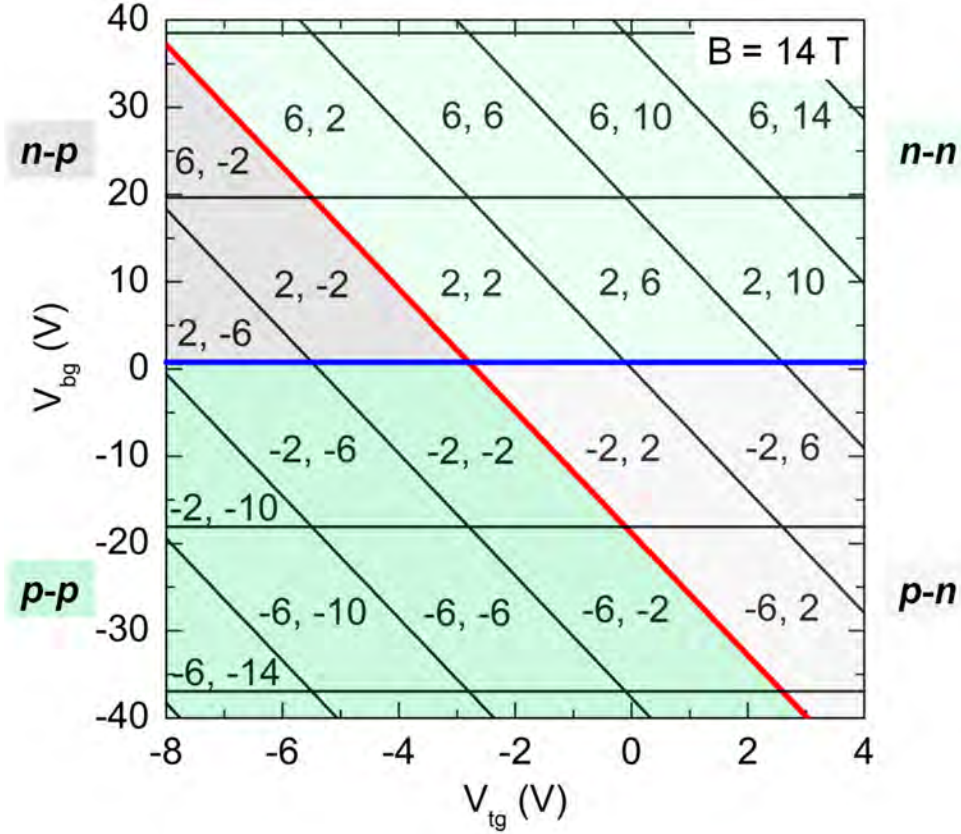


Figure 5.4: Expected Hall resistances R_H (represented by the associated filling factor numbers ν with $R_H = h/\nu e^2$) in the non-top-gated (indicated by the first filling factor number) and top-gated parts of the graphene layer as a function of gate voltages under quantum Hall conditions (at $B = 14$ T). The boundaries of the quantum Hall parallelograms are defined by $\nu_{1,2} = 0, \pm 4, \pm 8, \dots$. The gate voltage dependence of $\nu_{1,2}$ is given by Eq. 5.5 and 5.6. The thicker blue and red lines indicate a zero filling factor (i.e. a vanishing carrier density) in the regions without and with top-gating, respectively.

A 2D color map for the Hall resistance in region I measured between probe 13 and 19 at $B = 14$ T is shown in Fig. 5.5(a). It comprises a few horizontal bands that correspond to the characteristic Hall plateaux in graphene under quantum Hall conditions (see Chapter 4). Fig. 5.5(b) and (c) display a horizontal and a vertical cut across the 2D map, respectively. The perfect flatness of the curve in Fig. 5.5 (b) manifests that the Hall resistances in region I are indeed independent of the top-gate voltage.

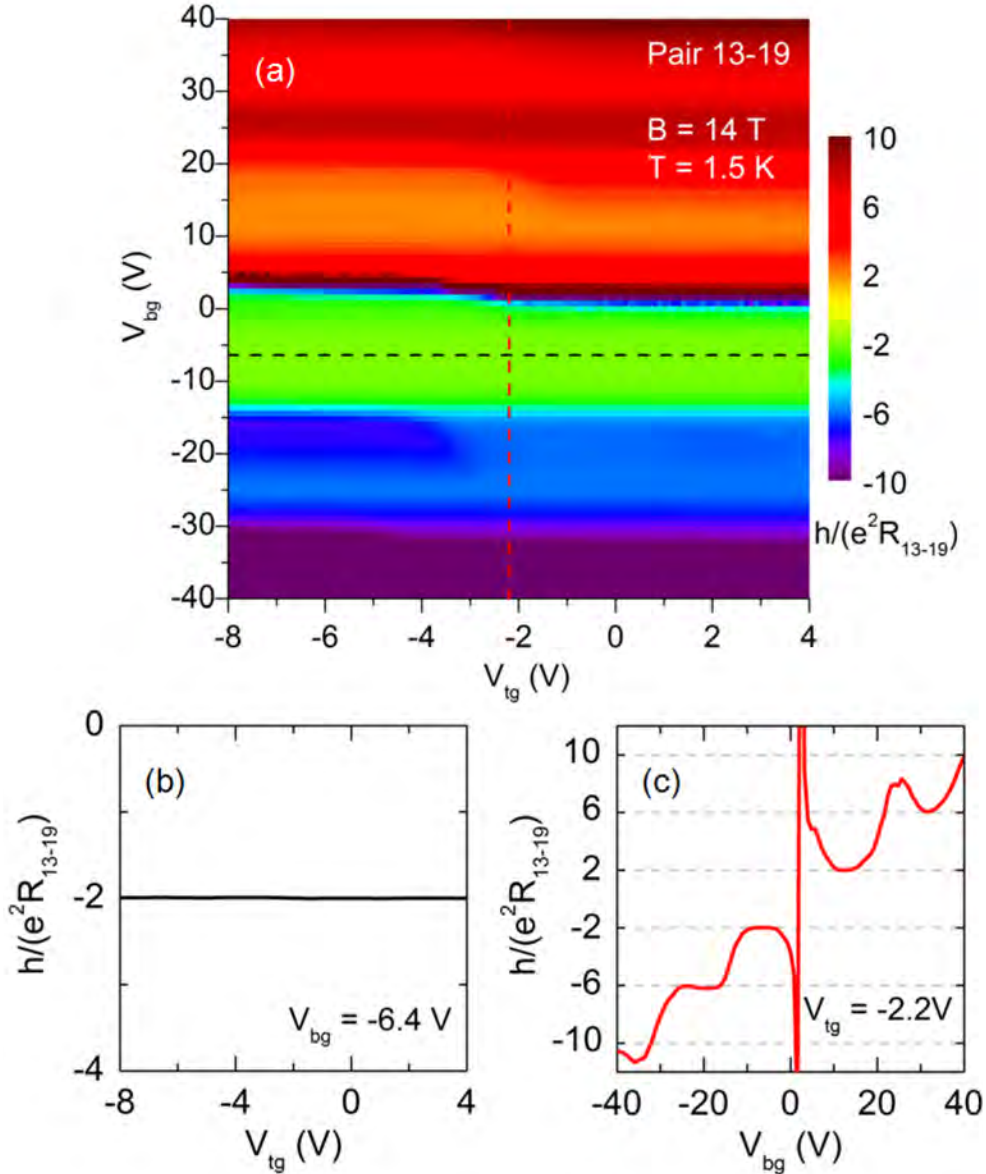


Figure 5.5: (a) 2D color map of the Hall resistance R_{13-19} in the non-top-gated region at $B = 14$ T. A horizontal and a vertical slice are shown in (b) and (c) respectively.

For region 2, the Hall resistance in the (V_{tg}, V_{bg}) space at $B = 14$ T is shown in Fig. 5.6(a). The slope of those skewed bands corresponds to the ratio of the coupling efficiencies of the two gates to the graphene sheet. A horizontal and a vertical slice across the color map are depicted in Fig. 5.6(b) and (c), respectively. Characteristic quantum Hall plateaus (for graphene) are resolved with striking precisions in both the electron and

hole regimes. This clearly demonstrates that our hybrid-gate-dielectric-based top-gating technique is capable of rendering high-quality bipolar graphene devices, where both the probing of local potentials and the changing of carrier type/density are realized in a very convenient way.

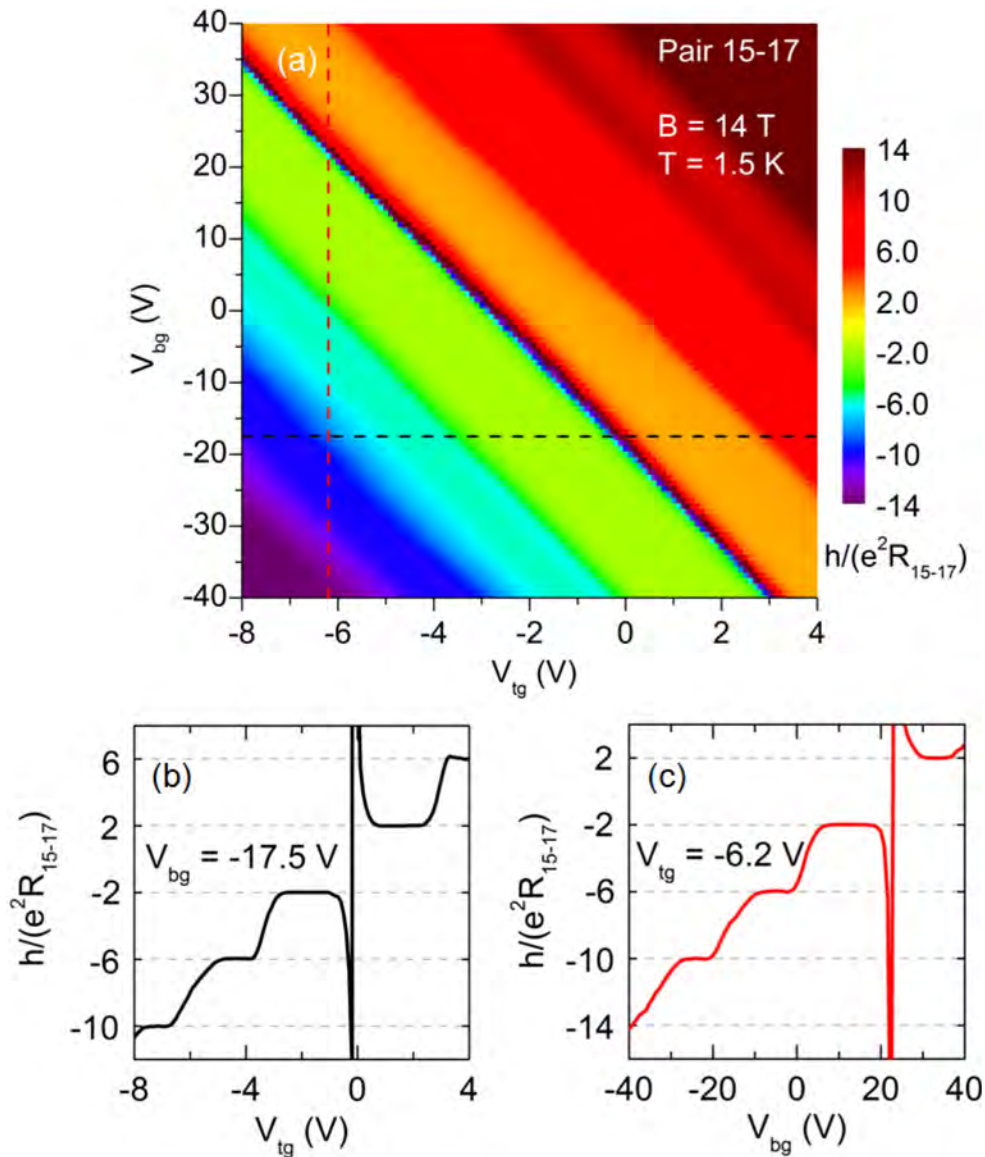


Figure 5.6: (a) 2D color plot of the Hall resistance R_{15-17} in the top-gated region at $B = 14$ T. The slope of the skewed bands gives the ratio of the coupling efficiencies of the two gates (the local top-gate and the global back-gate) to the graphene sheet. The curves in (b) and (c), which show the characteristic quantum Hall plateaus for graphene on both the electron and hole sides, correspond to the horizontal and the vertical cuts in (a), respectively.

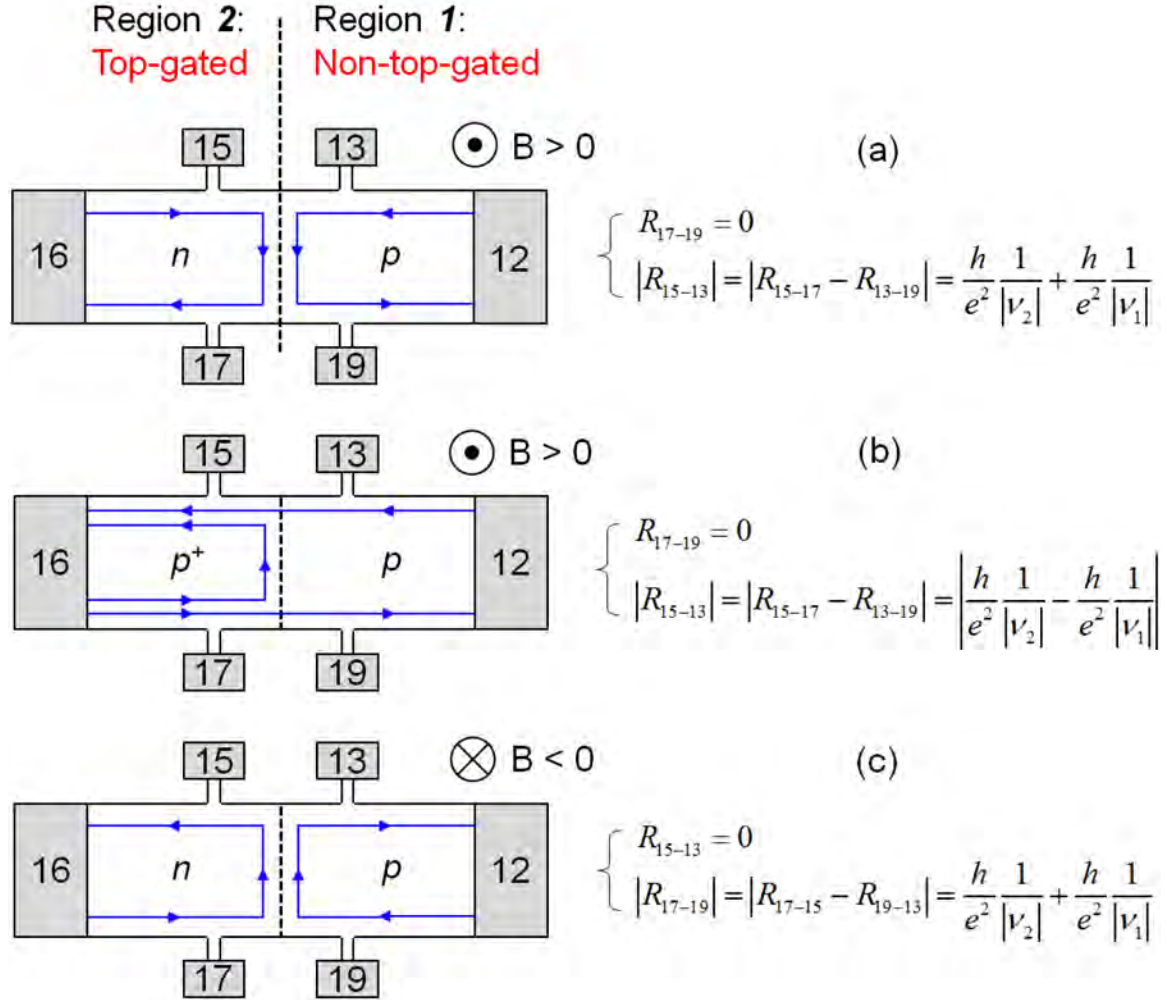


Figure 5.7: Schematic of quantum Hall edge modes in a double-gated graphene junction for three different combinations of carrier type and direction of magnetic field (a-c). Mode mixing at the p - n interface in the bipolar regime (a and c) leads to the equilibration of electrochemical potentials among edge modes. In the unipolar regime (b), however, some modes can transmit through the interface without mixing. For each of the three scenarios, the expected longitudinal resistances (under the assumption of a complete mode mixing) are given on the right hand side.

On the basis of Fig. 5.4, 5.5, 5.6 and the theory about the propagation and mixing of edge modes [1, 2], a prediction of the longitudinal resistances across the “ p - n ” interface can be made for the device in Fig. 5.1(a). Let us start with the quantum Hall states that are represented by the parallelogram $(-2, 2)$ in Fig. 5.4. Fig. 5.7(a) sketches the traveling of the edge modes in this configuration. According to the theory in Ref. [2], counter-

circulating edge states in n and p regions of the graphene layer send electrons and holes from source/drain reservoirs to the p - n interface, where equilibration of electrochemical potentials takes place. Energy dissipation makes this region a “hot-spot”. When the edge modes leave the interface area after a full mode mixing, probes 17 and 19 become equipotential. Hence, the longitudinal resistance between these two voltage probes is:

$$R_{17-19} = \frac{V_{17} - V_{19}}{I} = 0, \quad (5.7)$$

where I is the excitation current and V_{17} and V_{19} are the local potentials at lead 17 and 19, respectively. For the longitudinal resistance along the other edge of the graphene sheet, we have:

$$|R_{15-13}| = \left| \frac{V_{15} - V_{13}}{I} \right| = \left| \frac{V_{15} - V_{17}}{I} - \frac{V_{13} - V_{19}}{I} \right| = |R_{15-17}| + |R_{13-19}| = \frac{h}{e^2} \frac{1}{|v_2|} + \frac{h}{e^2} \frac{1}{|v_1|}. \quad (5.8)$$

Modeling shows that relationships similar to Eq. 5.7 and 5.8 can be applied to the whole bipolar regime.

Let us proceed to examine the unipolar case. The schematic diagram in Fig. 5.7(b) illustrates the modes traveling picture for a point in parallelogram (-2, -6) in Fig. 5.4. Here, the edge modes in region 1 and 2 circulate in the same direction. According to the theory [2], there is no mode mixing at the interface between the two regions; instead, some of the edge modes transmit through the p - p boundary and permeate the whole graphene layer. The modes that propagate along the lower edge of the graphene sheet originate from the same carrier reservoir. Due to the suppression of backscattering in the quantum Hall regime, the voltage probes 17 and 19 are equipotential, yielding

$$R_{17-19} = \frac{V_{17} - V_{19}}{I} = 0. \quad (5.9)$$

The longitudinal resistance between probes 15 and 13 can be expressed as:

$$|R_{15-13}| = \left| \frac{V_{15} - V_{13}}{I} \right| = \left| \frac{V_{15} - V_{17}}{I} - \frac{V_{13} - V_{19}}{I} \right| = \left| |R_{15-17}| - |R_{13-19}| \right| = \left| \frac{h}{e^2} \frac{1}{|v_2|} - \frac{h}{e^2} \frac{1}{|v_1|} \right|. \quad (5.10)$$

Furthermore, expressions similar to Eq. 5.9 and 5.10 are found generally applicable to the whole unipolar regime.

By reversing the magnetic field in Fig. 5.7(a) while keeping the carrier type and density unchanged, we obtain the diagram shown in Fig. 5.7(c). The circulation directions of the edge modes in both the *n* and *p* regions are now inverted compared to their original states in Fig. 5.7(a). This gives

$$R_{15-13} = \frac{V_{15} - V_{13}}{I} = 0 \quad (5.11)$$

and

$$|R_{17-19}| = \left| \frac{V_{17} - V_{19}}{I} \right| = \left| \frac{V_{17} - V_{15}}{I} - \frac{V_{19} - V_{13}}{I} \right| = |R_{17-15}| + |R_{19-13}| = \frac{h}{e^2} \frac{1}{|v_2|} + \frac{h}{e^2} \frac{1}{|v_1|}. \quad (5.12)$$

By comparing Eq. 5.11 and 5.12 to Eq. 5.7 and 5.8, we find that reversing of the magnetic field interchanges the longitudinal resistances between the two opposite edges of the graphene sheet. The same effect is also perceived for the unipolar configuration.

Now we are ready to examine the measured longitudinal resistances for the device in Fig. 5.1(a). A 2D color plot for the resistance between electrodes 15 and 13 (R_{15-13}) in a magnetic field $B = 14$ T is displayed in Fig. 5.8(a). The resistance between leads 17 and 19 (R_{17-19}) measured under the same conditions is shown in Fig. 5.8(b). Fig. 5.8(c) and (d) depict the color maps for R_{15-13} and R_{17-19} at $B = -14$ T. Horizontal slices at $V_{bg} = -9$ V and vertical cuts at $V_{tg} = -3$ V across the color maps are plotted in Fig. 5.8(e) and (f), respectively.

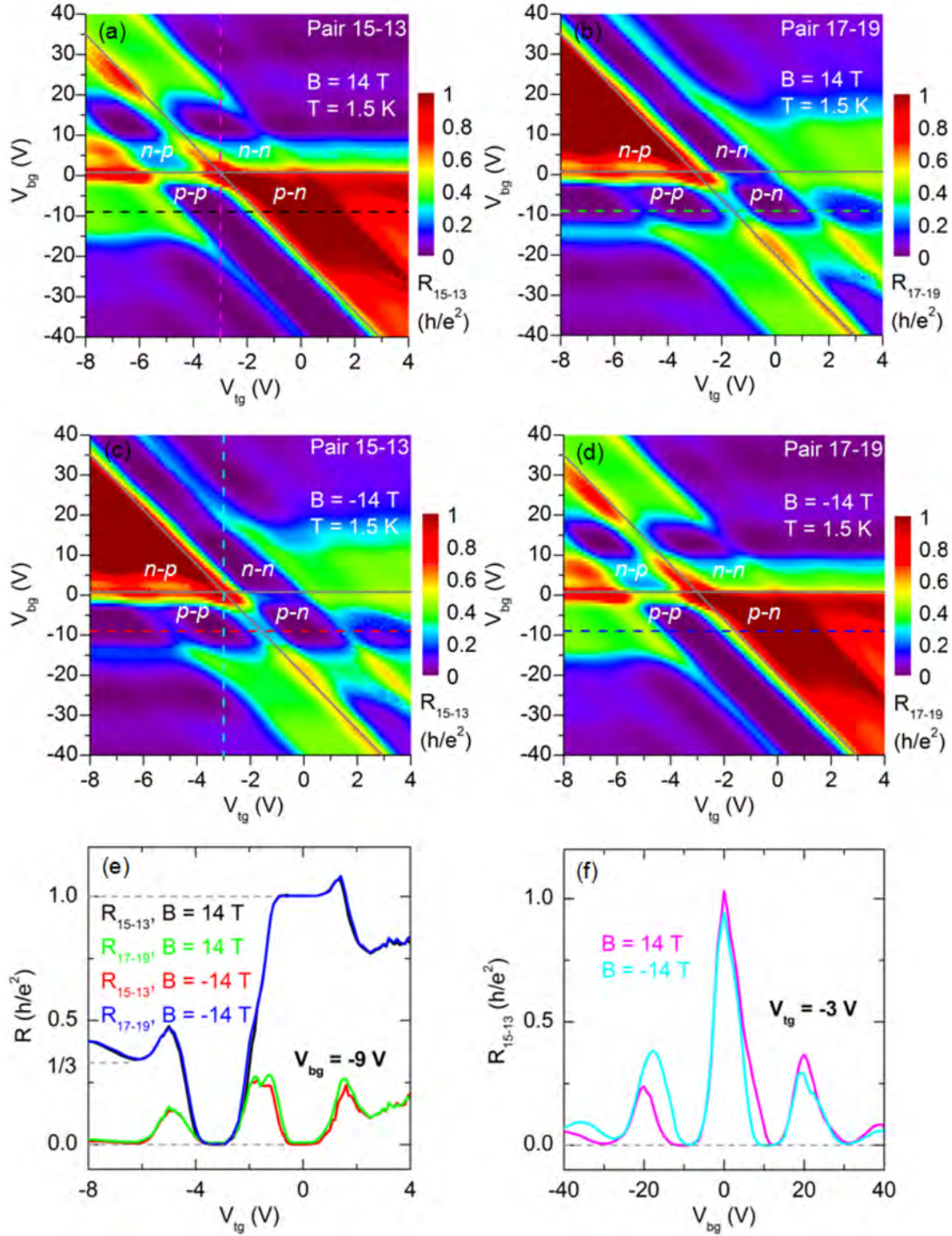


Figure 5.8: 2D color plots of measured longitudinal resistances R_L in (V_{tg}, V_{bg}) space at $B = 14$ T (a and b) and -14 T (c and d). Note that the two pairs of potential probes (pair 15-13 and pair 17-19) involved in voltage measurements are on the two opposite edges of the dual-gated device in Fig. 5.1(a). The horizontal and skewed gray lines highlight the charge neutrality points in the regions without and with top-gating. Four horizontal (indicated by the dashed black lines) and two vertical (indicated by the dashed red lines) cuts across the 2D maps are shown in (e) and (f), respectively. In panel (e), R_L plateaux at $h/3e^2$, 0 and h/e^2 are resolved. In panel (f), R_{15-13} vanishes at various back-gate voltages.

The trace for R_{15-13} at $B = 14$ T in Fig. 5.8(e) penetrates the *p-p* and *p-n* quadrants. Between $V_{tg} = -6.5$ V and $V_{tg} = 1.0$ V, three plateaux are resolved. From left to right, the first plateau corresponds to filling factors $\nu_1 = -2$ and $\nu_2 = -6$ for the non-top-gated and top-gated parts of graphene, respectively (see Fig 5.5(a) and 5.6(a)). Based on Eq. 5.10, we expect $h/3e^2$ for the first R_{15-13} plateau, and our measured resistance number is within 3% deviation of this anticipated value. The plateau in the middle features $(\nu_1, \nu_2) = (-2, -2)$ with a vanishing R_{15-13} as expected. The plateau on the right is associated with filling factors $(\nu_1, \nu_2) = (-2, 2)$. According to Eq. 5.8, the expectation for R_{15-13} here is h/e^2 (or equivalently, 25.8128 k Ω). Our measurement yields 25.86 k Ω , a rather precise match. The plot for R_{17-19} at $B = 14$ T in Fig. 5.8(e) shows three valleys. They occur right at the top-gate voltages that are associated with the plateaux in R_{15-13} (at $B = 14$ T). The vanishing R_{17-19} at these positions results either from a suppression of backscattering in the quantum Hall regime (the first two valleys counted from left to right) or from a full equilibration of the electrochemical potential at the *p-n* interface during mode mixing (the third valley). The zero-resistance states in Fig. 5.8(f) correspond to the situations where both the top-gated and non-top-gated regions have the same carrier type and an equal number of edge channels.

Finally, we stress the fact that the 2D map for R_{15-13} (R_{17-19}) at $B = 14$ T is essentially identical to that of R_{17-19} (R_{15-13}) at $B = -14$ T, as predicted by our modeling.

5.4 Graphene *p-n-p* devices with boron nitride as the top-gate dielectric

5.4.1 Transferred BN films as the top-gate dielectric

An atomically thin insulating film can be crucial to the investigation of such interesting topics in graphene physics as quantum capacitance measurement [9] and Coulomb drag between closely spaced graphene layers [10]. By utilizing the precise transfer technique introduced in section 2.3.5, we are able to place a few-nanometer-thick hexagonal boron nitride (h-BN) sheet on top of graphene.

Fig. 5.9 displays the optical images taken during the fabrication of a double-gated graphene device using a transferred h-BN film as the top-gate dielectric. Note the h-BN chunks on the target substrate after transfer (Fig. 5.9(b)-(d)). Owing to their good visibility, these relatively thick h-BN pieces are especially helpful in locating the thin and faint-colored source h-BN sheet on the PMMA membrane.

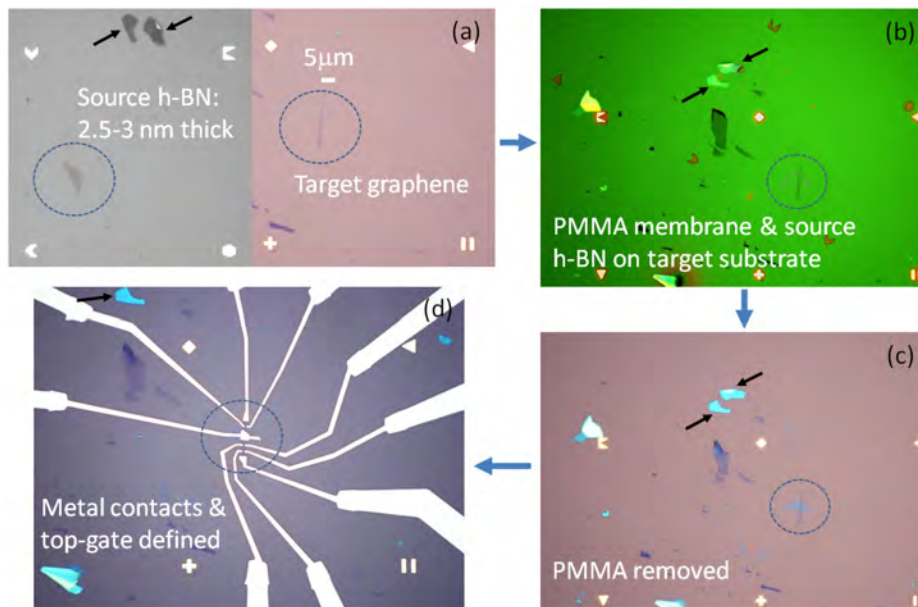


Figure 5.9: Optical micrographs of an h-BN sheet (source) before (a) and after (b and c) being transferred onto a graphene flake (target). The finished dual-gated device with the transferred h-BN film as the top-gate dielectric is shown in (d). The black arrows point to two h-BN chunks with thicknesses larger than 10 nm. Alignment marker dimension = $5 \mu\text{m} \times 5 \mu\text{m}$.

5.4.2 Electrical characterizations

Fig. 5.10(a) shows the zoomed-in optical micrograph of a completed p - n - p device with the assignment of the electrical leads. A cross-section view of the sample is illustrated in Fig. 5.10(b). Four-terminal characterizations depicted in Fig. 5.10(b)-(d) indicate a reasonable electronic quality for the uncovered part of the graphene sheet.

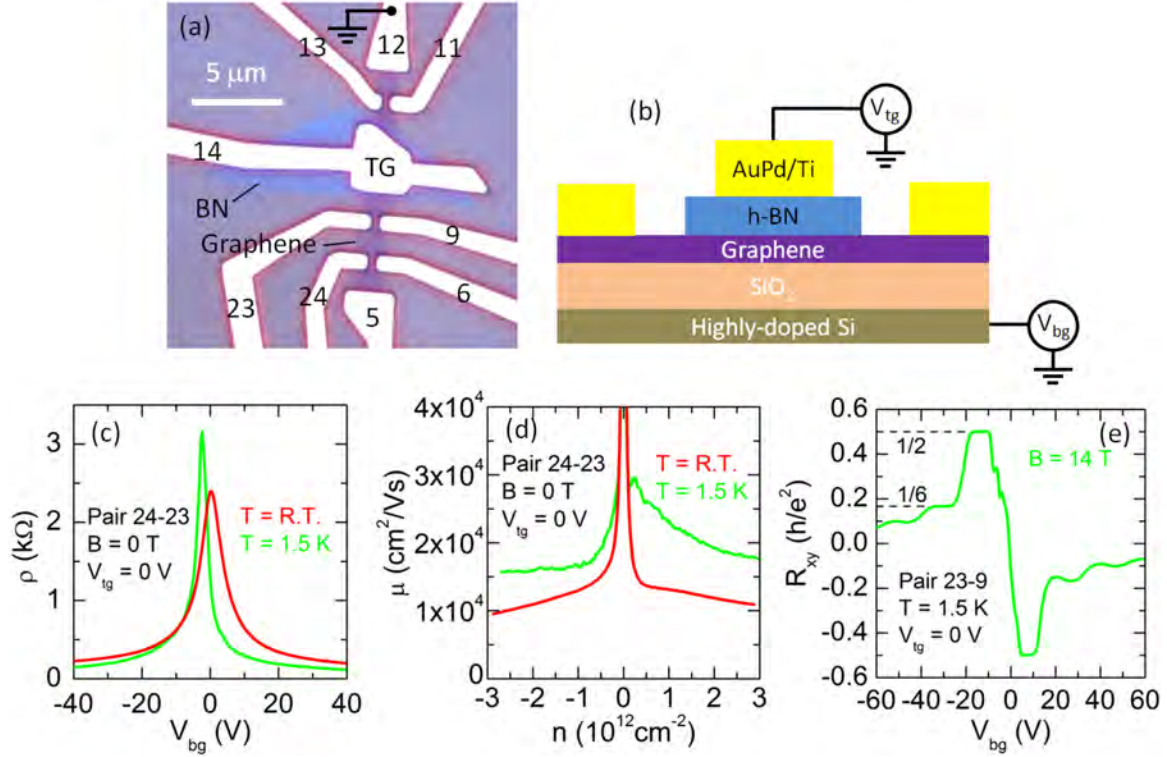


Figure 5.10: (a) Optical image of a graphene p - n - p device with assigned electrodes. The h-BN top-gate dielectric with a measured thickness of 2.5-3.0 nm appears bluish in the micrograph. (b) Cross-section view of the p - n - p device. (c)-(e) Transport measurements performed in a four-terminal configuration on the exposed part of the graphene sheet at room and low temperatures.

A 2D color rendition of the resistance between probes 23 and 13 at $B = 0$ T is shown in Fig. 5.11. The slope η of the diagonal band gives the ratio of the coupling efficiencies of the two gates to the graphene sheet as discussed in the previous section. This yields

$$\eta = C_{tg} / C_{bg} = \frac{\epsilon_{h-BN}}{\epsilon_{bg}} \cdot \frac{d_{bg}}{d_{h-BN}} \approx 97, \quad (5.13)$$

where $\epsilon_{h\text{-BN}}$ is the dielectric constant of h-BN crystal along the *c*-axis and $d_{h\text{-BN}}$ is the thickness of the h-BN film. By assuming $\epsilon_{h\text{-BN}} \sim 3.5$ [11, 12], $\epsilon_{bg} \sim 3.9$ and $d_{bg} \sim 300$ nm, we obtain $d_{h\text{-BN}} \sim 2.8$ nm. This is in good agreement with the measured thickness (2.5-3.0 nm) by tapping-mode AFM topography.

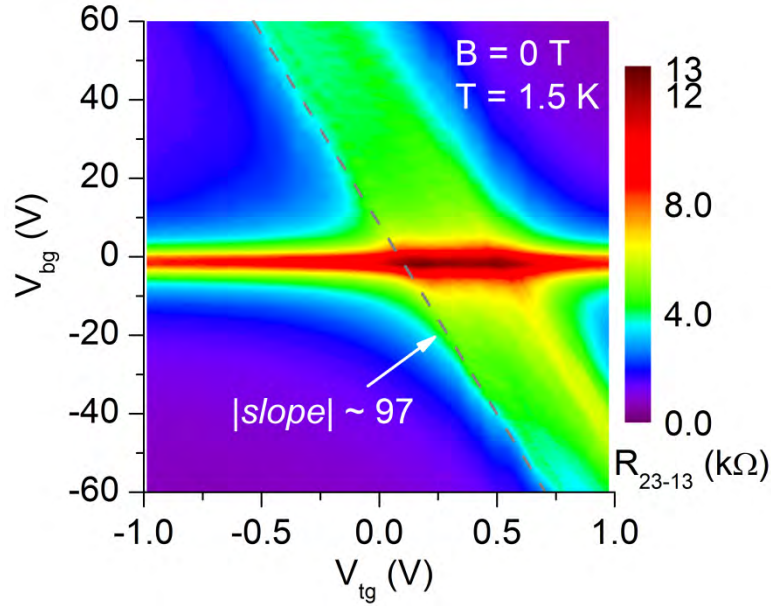


Figure 5.11: 2D color map of resistance across the top-gated region (between contacts 23 and 13 of the sample in Fig. 5.10(a)) as a function of gate voltages at $B = 0$ T and $T = 1.5$ K. The slope of the skewed band (highlighted by the dashed gray line) corresponds to a top-gate coupling efficiency ~ 97 times of the Si back-gate.

In Fig 5.11, we notice that the diagonal band that is associated with the local resistance maxima in the top-gated region is relatively wide. One possible reason for this broadening is the existence of electron and hole puddles in the vicinity of charge neutrality [13-16] in the top-gated part of graphene. Even though the charge inhomogeneity tends to be smoothed out at high carrier densities, the effect of the random network of electron and hole droplets becomes non-negligible when the average carrier density in graphene approaches zero. The broadening of the skewed band may also be related to the ripples [17] and wrinkles in the h-BN and graphene sheets. The presence of

wrinkles is evidenced by AFM topography measurement, as well as the SEM image in Fig. 5.12, where the locations of the wrinkles are indicated by blue arrows. AFM topography shows that the height of these bumps is typically below 5 nm. According to Eq. 5.3, unevenness in spacing between the metal top-gate and the graphene layer will result in a spatial inhomogeneity in gate coupling. This non-uniformity in (top) gate capacitance is no longer negligible when the thickness of the gate dielectric shrinks to a few nanometers. The root cause that accounts for the local deformations in transferred h-BN films is not totally clear yet. Nevertheless, we suspect that the stress applied to the h-BN film during mechanical exfoliation and/or the dissolution of the PMMA membrane (after transfer) in a warm organic solvent might probably play a role.

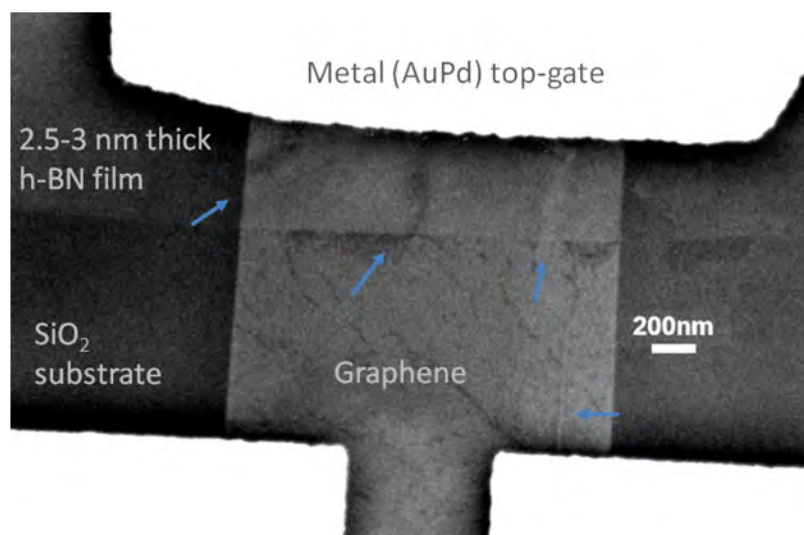


Figure 5.12: (Secondary electron) SEM image of the top-gated area showing the presence of wrinkles (highlighted by the blue arrows) in both the h-BN and graphene sheets. Earlier AFM topography reveals that the local bumps in these thin films have a height below 5 nm.

Now let us examine the insulation properties of the transferred thin h-BN films. Fig. 5.13(a) depicts the DC I - V characteristic measured through a 2.5-3.0 nm thick h-BN sheet at a temperature of 1.5 K. The curve exhibits a tunneling-like behavior. The overlap area

among the metal top-gate, the dielectric film and the graphene sheet is around $5 \mu\text{m}^2$. The leakage current is lower than 1 nA at a top-gate voltage of no higher than 0.5 V. Above 0.5 V, however, the leakage current rapidly increases. To our surprise, up to a 2-volt voltage difference between the top and bottom surfaces the h-BN film still shows no sign of a “hard” breakdown. The DC I - V feature for a slightly thicker h-BN sheet is displayed in Fig. 5.13(b). AFM topography on this film yields a thickness of 4.0-4.5 nm. To make the comparison for leakage current easier, we have carefully patterned the metal gate on top of this h-BN specimen such that the overlap between the top-gate metal and the underneath thin films (i.e. h-BN and graphene) is also about $5 \mu\text{m}^2$. The room-temperature leakage current through the h-BN layer is found to be well below 1 nA for a top-gate voltage as high as 2 V. The highly insulating state in thin h-BN films suggests their potential applications as ultra-thin dielectric layers.

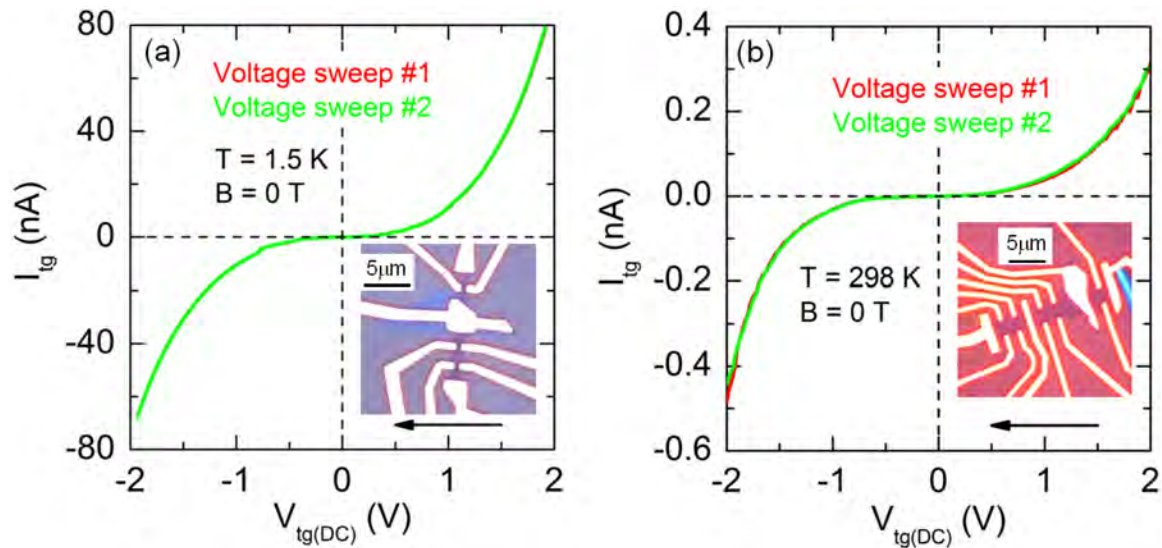


Figure 5.13: DC tunneling-like I - V plots for thin h-BN layers. The insets in (a) and (b) are the optical images of the two top-gated devices (h-BN thickness in (a): 2.5-3 nm; in (b): 4.0-4.5 nm). During measurement, a voltage V_{tg} is applied to the metal top-gate and the graphene sheet is grounded. The leakage current through the h-BN films is recorded. The black arrows indicate the direction of the voltage sweeps. In both devices, the overlap between the metal top-gate and the underneath h-BN and graphene sheets is close to $5 \mu\text{m}^2$.

References

- [1] M. Büttiker, *Absence of backscattering in the quantum Hall effect in multiprobe conductors*, Physical Review B **38**, 9375 (1988).
- [2] D. A. Abanin and L. S. Levitov, *Quantized transport in graphene p-n junctions in a magnetic field*, Science **317**, 641-643 (2007).
- [3] J. H. Chen, C. Jang, S. Adam, M. S. Fuhrer, E. D. Williams, and M. Ishigami, *Charged-impurity scattering in graphene*, Nature Physics **4**, 377 (2008).
- [4] V. V. Cheianov and V. I. Fal'ko, *Selective transmission of Dirac electrons and ballistic magnetoresistance of n-p junctions in graphene*, Physical Review B **74**, 041403 (2006).
- [5] M. I. Katsnelson, K. S. Novoselov, and A. K. Geim, *Chiral tunnelling and the Klein paradox in graphene*, Nature Physics **2**, 620-625 (2006).
- [6] J. R. Williams, L. DiCarlo, and C. M. Marcus, *Quantum Hall effect in a gate-controlled p-n junction of graphene*, Science **317**, 638-641 (2007).
- [7] T. Lohmann, K. Von Klitzing, and J. H. Smet, *Four-terminal magneto-transport in graphene p-n junctions created by spatially selective doping*, Nano Letters **9**, 1973-1979 (2009).
- [8] A. H. Castro Neto, F. Guinea, N. M. R. Peres, K. S. Novoselov, and A. K. Geim, *The electronic properties of graphene*, Reviews of Modern Physics **81**, 109-162 (2009).
- [9] J. Xia, F. Chen, J. Li, and N. Tao, *Measurement of the quantum capacitance of graphene*, Nature Nanotechnology **4**, 505 (2009).
- [10] H. Min, R. Bistritzer, J.-J. Su, and A. H. MacDonald, *Room-temperature superfluidity in graphene bilayers*, Physical Review B **78**, 121401 (2008).

- [11] A. F. Young, C. R. Dean, I. Meric, S. Sorgenfrei, H. Ren, K. Watanabe, T. Taniguchi, J. Hone, K. L. Sheperd, and P. Kim, *Electronic compressibility of gapped bilayer graphene*, <http://arxiv.org/abs/1004.5556v2> (2010).
- [12] C. R. Dean, A. F. Young, I. Meric, C. Lee, L. Wang, S. Sorgenfrei, K. Watanabe, T. Taniguchi, P. Kim, K. L. Shepard, and J. Hone, *Boron nitride substrates for high-quality graphene electronics*, *Nature Nanotechnology* **5**, 722-726 (2010).
- [13] E. H. Hwang, S. Adam, and S. D. Sarma, *Carrier transport in two-dimensional graphene layers*, *Physical Review Letters* **98**, 186806 (2007).
- [14] K. Nomura and A. H. MacDonald, *Quantum transport of massless Dirac fermions*, *Physical Review Letters* **98**, 076602 (2007).
- [15] J. Martin, N. Akerman, G. Ulbricht, T. Lohmann, J. H. Smet, K. von Klitzing, and A. Yacoby, *Observation of electron-hole puddles in graphene using a scanning single-electron transistor*, *Nature Physics* **4**, 144 (2008).
- [16] Y. Zhang, V. W. Brar, C. Girit, A. Zettl, and M. F. Crommie, *Origin of spatial charge inhomogeneity in graphene*, *Nature Physics* **5**, 722-726 (2009).
- [17] J. C. Meyer, A. K. Geim, M. I. Katsnelson, K. S. Novoselov, T. J. Booth, and S. Roth, *The structure of suspended graphene sheets*, *Nature* **446**, 60-63 (2007).

Chapter 6

Detection of Landau emission from graphene: system design and preliminary optimizations

In this chapter, we report on our preliminary attempts in designing and optimizing a compact system for the detection of the inter-Landau-level radiative transitions (i.e. Landau emission) in graphene devices. The emission power is estimated to be extremely low ($<10^{-11}$ W). The mid-infrared photodetector is operated in a highly resistive state due to the lack of background radiation in the surrounding environment. Various efforts in improving the sensibility of the detection system and reducing the noise level in the circuit are discussed. We introduce a non-destructive deposition of radiation-blocking structures on top of the two “hot spots” (energy dissipation corners in the quantum Hall regime) along one diagonal of the graphene Hall-bar, such that the Landau emission from the emitter can be selectively blocked out depending on the direction of the magnetic field. Thus even for the same amount of input electric power into the graphene emitter, the Landau radiation that reaches the photodetector differs. The response of the photodetector in the “radiation-blocked” situation, where a smaller portion of the Landau emission arrives at the detector, is recorded as the reference signal. Subsequently, radiation identification is carried out in a reversed magnetic field.

6.1 Inter-Landau-level transitions in graphene

In conventional semiconductors with parabolic dispersion a magnetic field B will quantize the “free-carrier” energy levels into a series of Landau levels. The level separation is directly proportional to B . As early as 1960, researchers already recognized that radiative transitions between Landau levels (i.e. Landau emission) might give rise to a wavelength-tunable laser [1]. In 1972, Gornik observed Landau emission from n -InSb [2]. Decades later, Komiyama’s group systematically studied the spontaneous cyclotron emission from the finite two-dimensional electron gas (2DEG) layers in GaAs/AlGaAs heterostructures [3-12]. In all these experiments, the radiation was generated by electrical excitations. Nonequilibrium hot electrons that are heated up by applied electric fields lead to population of Landau levels (LLs) with higher energies, rendering inter-Landau-level radiative transitions possible.

The allowed inter-Landau-level transitions in graphene conform to the following selection rule [13-17]:

$$\Delta N = |N_{final}| - |N_{initial}| = \pm 1, \quad (6.1)$$

where N is the Landau level index.

The Landau level energies in graphene are expressed as (see section 4.1):

$$E_N = \pm v_F \sqrt{2e\hbar B |N|}, \quad (6.2)$$

where v_F is the Fermi velocity ($\sim 10^6$ m/s [18, 19]), B is the magnetic field and the positive and negative signs stand for electrons and holes, respectively.

In a 2D electronic system with 2-fold spin degeneracy and 2-fold sublattice degeneracy, the Fermi wave vector k_F is related to the carrier density n by [20]:

$$k_F = \sqrt{\pi|n|}. \quad (6.3)$$

For the relativistic particles (carriers) in graphene, the linear energy-momentum dispersion gives the relation between energy and carrier density [21]:

$$E_F = \pm \hbar k_F v_F = \pm \hbar v_F \sqrt{\pi|n|}, \quad (6.4)$$

where E_F is the Fermi level (to be precise, chemical potential if temperature $T > 0$). In section 3.2, we already showed that carrier density n is proportional to the gate coupling and effective gate voltage ($n \propto (V_g - V_g^0)$, where V_g^0 is the gate voltage at which the sample reaches on average charge neutrality). In the presence of a perpendicular magnetic field, this tunability of E_F (by changing n) implies that E_F can be placed between two specified Landau levels so that a “desirable” inter-Landau-level optical transition might take place. The calculated LL spectra in graphene as a function of the magnetic field B is shown in the left panel of Fig. 6.1, whereas a theoretically allowed inter-Landau-level transition between LL0 and LL1 at a magnetic field of 14 T is schematically illustrated in the right panel.

Fig. 6.2 shows the energies associated with the transitions between neighboring LLs in graphene as a function of the magnetic field B . These calculated values are in good agreement with the observations in magneto-transmission studies [13, 15, 17]. For $B \geq 8$ T, almost all these transition energies fall within the mid-infrared (MIR) regime.

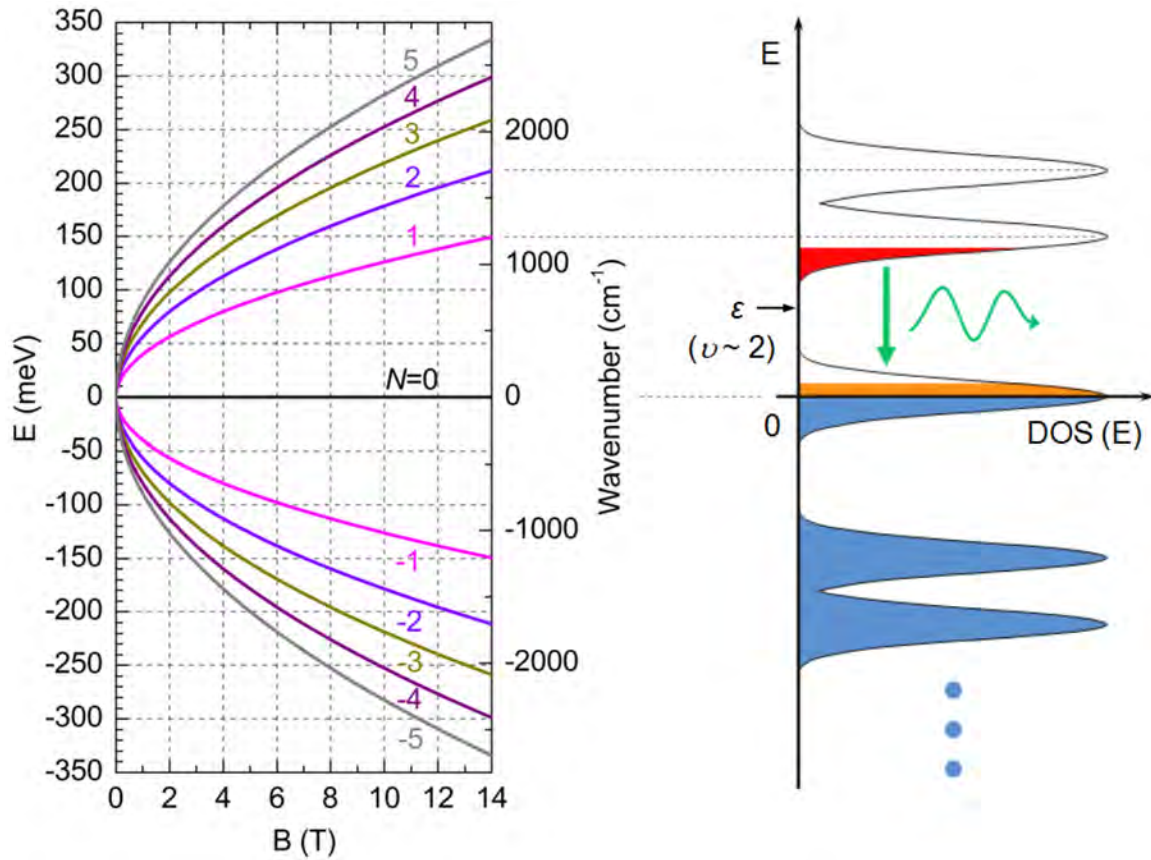


Figure 6.1: Left: Calculated LL spectra of graphene as a function of the magnetic field B using Eq. 6.2. Right: schematic representation of a possible optical transition between the zeroth and the first LL at $B = 14$ T. The density of states and electron populations at various LLs are sketched. The chemical potential ϵ corresponds to a filling factor $\nu \sim 2$. The nonequilibrium hot electrons that have been excited from LL0 onto LL1 by the applied electric field are indicated in red.

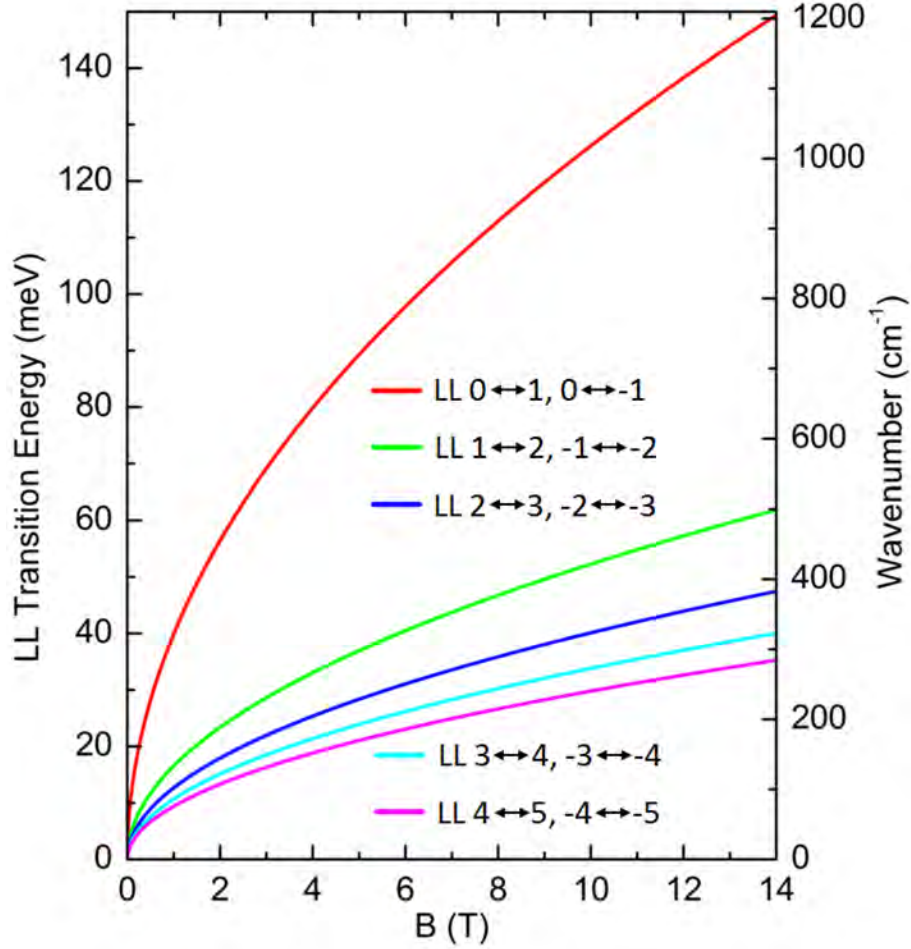


Figure 6.2: Theoretically expected LL transition energies in graphene as a function of the magnetic field. The pair of involved LLs is indicated for each of the transitions.

6.2 System design and experimental methods

The emission efficiency (i.e. the ratio of the Landau emission power over the dissipated electrical power) in the 2D electronic system in GaAs/AlGaAs heterostructures was found to be about 10^{-6} [3]. On the basis of the similarities between our detection setup (which will be addressed in the following text) and the one reported by Henriksen [22] in his magneto-transmission experiments, we (very roughly) estimate that the collection efficiency (the radiation that can be effectively collected by the photodetector

over the total Landau emission power) of our photodetector is on the order of 1%. These two ratios give a first estimation about the intensity of the Landau radiation that may reach our detector: for 1 mW total input power into the graphene emitter, probably only $\sim 10^{-11}$ W (or even less) Landau emission may be directly seen by the detector. Hence, it is necessary to have an extremely sensitive photodetector working at MIR wavelengths.

A Si:B (i.e. Si substrate doped with boron atoms) photoconductive detector from IRLabs Inc. with a square-shaped receiving surface (effective area: $1 \times 1 \text{ mm}^2$, see Fig. 6.3) appears to be a good candidate. The spectral response of the detector spans from $5 \text{ }\mu\text{m}$ to $30 \text{ }\mu\text{m}$, with a current responsivity of 28.6 A/W (calibrated with a standard blackbody emitter) at an incoming wavelength $\lambda = 17.5 \text{ }\mu\text{m}$. During operation, incident radiation ionizes the boron dopants in the Si substrate of the detector, thus creating holes in the valence band of Si and making the material photoconductive. Consequently, only holes contribute to the photocurrent. In principle, this type of photodetector should work at low temperatures where thermal ionization of the dopant atoms has barely set in.

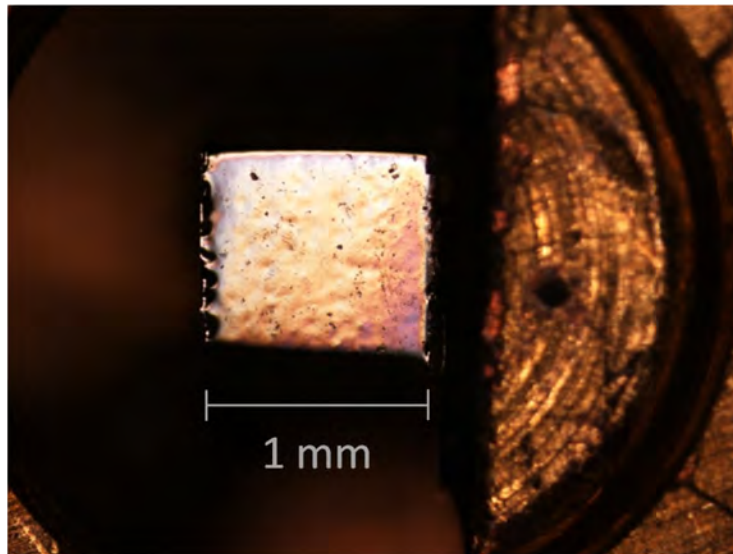


Figure 6.3: Optical image of the broadband Si:B photoconductive detector from IRLabs Inc. The receiving surface (shown in the center of the micrograph) is a $1 \text{ mm} \times 1 \text{ mm}$ square.

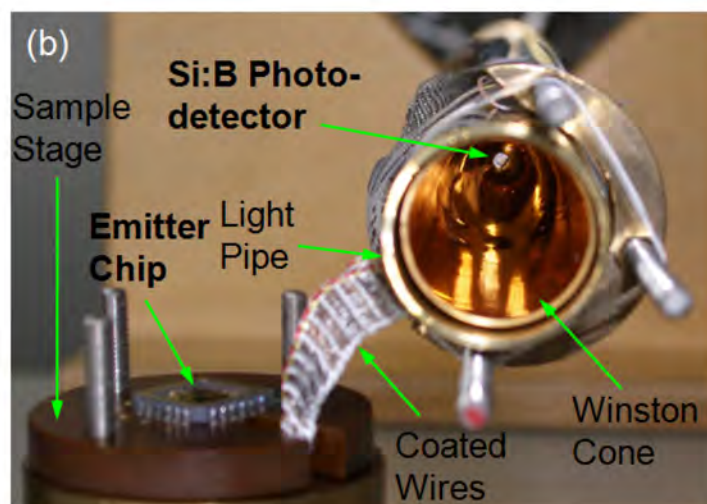
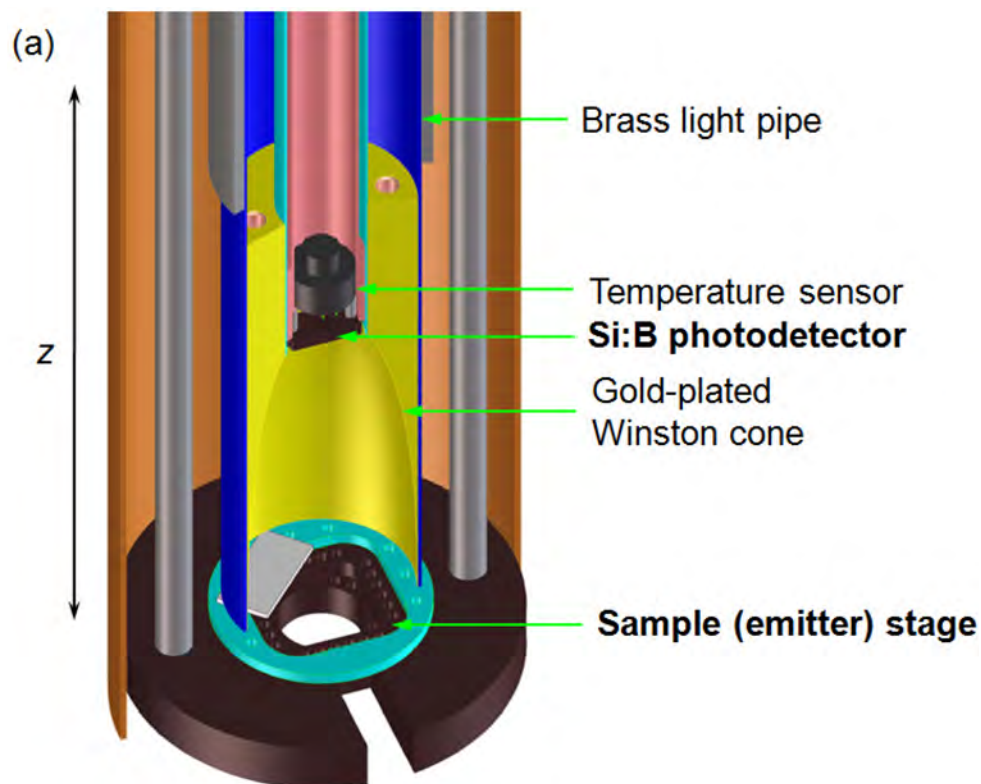


Figure 6.4: (a) Schematic of the sample holder assembly containing both the emitter and the optics for mid-infrared radiation detection. The graphene emitter is mounted on the sample stage. The top surface of the sample stage has a good contact with one end of a light pipe ensuring a large solid angle for radiation collection. A parabolic cone for wave condensation can move inside the light pipe along the z -direction. The Si:B photodetector is installed right at the exit aperture of the cone. This sample holder is operated inside a variable temperature insert of a ^4He cryostat. (b) The real emitter-detector assembly.

Fig. 6.4(a) depicts the schematic of the sample holder housing both the graphene emitter and the Si:B photodetector. During operation, the oxidized Si substrate with a graphene emitter on top is mounted on the sample stage. One flat end (rim) of a light pipe made of polished brass touches the top surface of the sample stage, so that the solid angle for emission collection is about 180° . Inside the light pipe there is a gold-plated Winston cone that is in close contact with the pipe and can move along the z -axis. The entrance aperture of the cone is about 16 mm in diameter; while the exit is 2 mm. This parabolic cone is utilized to concentrate the incoming radiation. Our Si:B photodetector is installed right at the exit aperture of the cone, so that MIR waves passing through the relatively large entrance aperture can always be concentrated onto the radiation-collecting surface ($1 \times 1 \text{ mm}^2$) of the detector. To monitor the local temperatures nearby the emitter and the detector, two high-precision temperature sensors are installed in close proximity of the sample stage and the photodetector, respectively. The sample holder assembly resides in a variable temperature insert (VTI) of a ^4He cryostat. By manipulating the ^4He vapor pressure and the input power to an embedded heater in the VTI, temperatures between 1.4 K and 200 K can be obtained in the insert space. The real probe that contains both the graphene emitter and the Si:B photodetector is shown in Fig. 6.4(b).

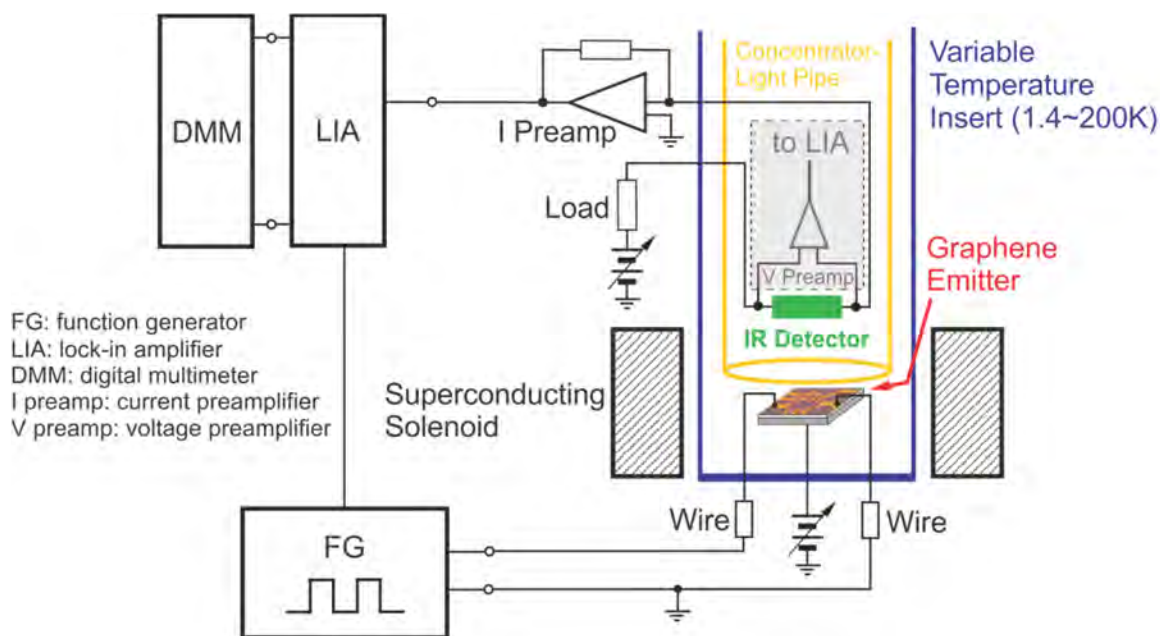


Figure 6.5: Schematic of the radiation detection circuit. The graphene emitter is electrically excited by an AC function generator at a certain frequency (fundamental frequency) between 10 and 130 Hz. Battery packs are utilized to bias the photodetector and to power the preamplifiers. The photocurrent is amplified by either a low-noise current preamplifier or a high-input-impedance voltage preamplifier. Lock-in technique is employed to pick out the photosignal either at the fundamental excitation frequency (when the electrical excitation is a square wave) or at its second harmonic (when the excitation has a sinusoidal waveform).

Fig. 6.5 illustrates the schematic diagram of the radiation detection circuit. Due to the space limitations, there is no mechanical chopper in the sample holder. We use a low-frequency AC (strictly speaking, oscillating) current (or voltage) to excite the graphene emitter, and employ the standard lock-in technique to measure the oscillating photocurrent (note that the photodetector is biased by DC batteries). The frequency of the electrical excitation ranges between 10 and 130 Hz. This frequency band is selected based on the trade-off between the $1/f$ noise level and the RC time constant in the photosignal amplification circuit. Higher excitation frequencies offer lower $1/f$ noise, but also demand a relatively small RC constant in the detection circuit. The waveform for the excitation current or voltage can be either sinusoidal or square. In the case of a sine-wave

excitation, a photosignal at the second harmonic of the fundamental excitation frequency f should be collected. This is because the input excitation power is proportional to the square of the applied current or voltage, and mathematically the square operation on a sinusoidal wave gives its second harmonic. Alternatively, when the excitation current or voltage is a square wave that oscillates between zero and a certain level, a photosignal at the fundamental excitation frequency is to be recorded.

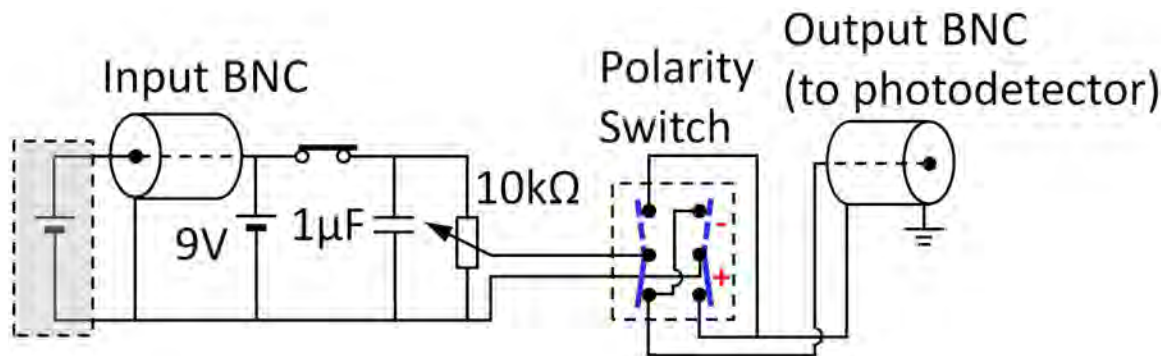


Figure 6.6: Schematic diagram for the circuit inside a home-made detector bias-box. The 1 μF by-pass capacitor filters out high-frequency glitches. The 10-k Ω potentiometer makes the output of the battery tunable between ± 9 V. The closing position of the two blades (indicated by the blue lines) of the polarity switch determines the sign of the output voltage (the lower solid blue lines correspond to a positive output, while the upper dashed ones correspond to a negative voltage).

Since the radiation power reaching the detector is expected to be extremely low, it is necessary to take measures reducing the noise level in the detection circuit. The cross-talk between the emitter and the detector needs to be suppressed and any grounding loop in the circuit must be eliminated. We introduced a home-made bias-box to provide a clean DC bias to the photodetector. The circuit diagram is shown in Fig. 6.6. The 10-k Ω potentiometer in the metallic housing makes the bias voltage continuously tunable between +9 V and -9 V. The polarity switch offers a convenient inversion of the bias polarity. Coax cables are used to wire the photodetector. All the other wires in the sample

holder are protected by a highly insulating coating, and are physically separated from one another. To reduce the noise level and to prevent any possible grounding loop induced by the AC power supplies, we use batteries to power the preamplifiers. With all these means, a noise level as low as ~ 10 fA has been achieved in our detection circuit.

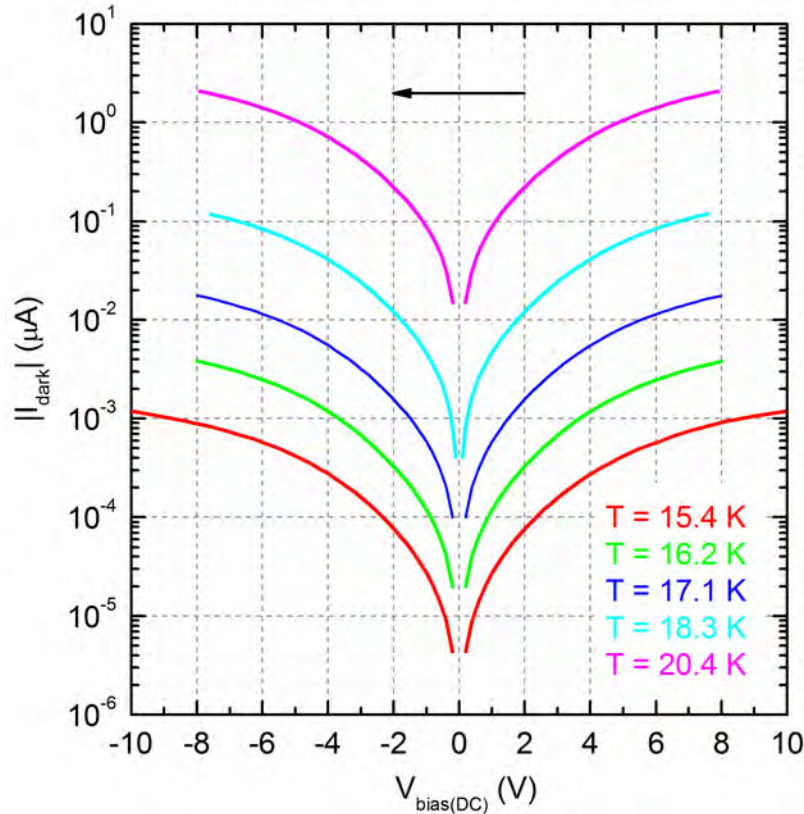


Figure 6.7: Dark (leakage) current characteristic of the Si:B photodetector at various temperatures ($B = 0$ T). Generally, at elevated temperatures the detector becomes less resistive and the RC constant in the detection circuit decreases accordingly. Meanwhile, the noise level increases rapidly with temperature.

Due to the lack of an optical window in our system, essentially no background radiation can propagate into the sample space. Therefore, without the emission from the graphene emitter the Si:B photodetector will work in a fully dark environment. Fig. 6.7 depicts the detector's dark current characteristic as a function of the bias voltage at

various temperatures. To avoid too large an RC constant in the detection circuit, the detector is operated at temperatures (e.g. up to 16 K) higher than most of those reported in the literature [23]. The side effect is, however, that the noise level in the circuit increases considerably with temperature. We optimize the bias voltage to the photodetector so that both a high sensitivity (by the maximization of $|dI/dV|$ in the I - V characteristic) and a moderate resistance value are achieved on the detector.

In principle, either a current preamplifier (I-preamp, a.k.a. transimpedance amplifier or current-to-voltage converter, e.g. Model 1211 of Ithaco) or a voltage preamplifier (V-preamp, e.g. SR560 of Stanford Research Systems) can be employed for photocurrent amplification (see Fig. 6.5). In the latter case, a load resistor with a resistance on the same order of magnitude as that of the photodetector is connected in series with the detector. In the presence of an AC photocurrent, the AC voltage across the detector (or the load resistor) is amplified by the voltage preamplifier. A prerequisite is that the input impedance of the V-preamp is much larger than the resistance of the detector (and the load resistor). In our case, this means that the input impedance (Z_{in}) must be larger than $1\text{ G}\Omega$ at $f = 10\text{-}130\text{ Hz}$. This requirement is difficult to fulfill with commercial V-preamps. To overcome this problem, we introduced a home-made input buffer. The corresponding schematic is illustrated in Fig. 6.8. This device essentially consists of two voltage followers each with a gain of unity. The output of the upper follower not only drives the input of the external V-preamp (e.g. SR560), but also serves as the input to the other follower. The output of the lower follower drives the inner sheath of a triax cable to the same potential level as its core. This renders an effective suppression of the capacitive coupling between the core and inner sheath of the triax cable. And consequently, the

coupling between the core and metallic shield of the buffer's input BNC becomes dramatically attenuated even at relatively high frequencies. The Z_{in} of the input buffer is thus determined by the extremely high input impedance of the upper operational amplifier (e.g. *AD549* of Analog Devices). We found that Z_{in} of our input buffer remains well above $1 \text{ G}\Omega$ at $f = 130 \text{ Hz}$.

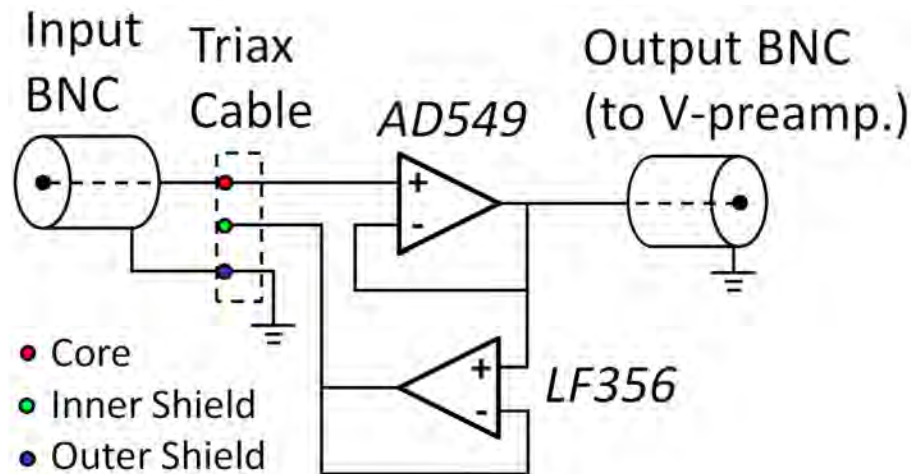


Figure 6.8: Schematic diagram of a home-made high-impedance input buffer. Both operational amplifiers (*AD549* of Analog Devices and *LF356* of National Semiconductor) work as voltage followers with a gain of unity. The equal potential between the core and inner sheath of the triax cable effectively suppresses the capacitive coupling between these two conducting layers. Consequently, the input impedance of this input buffer is determined by the input impedance of *AD549* that is found to be much larger than $1 \text{ G}\Omega$ at a frequency of 130 Hz .

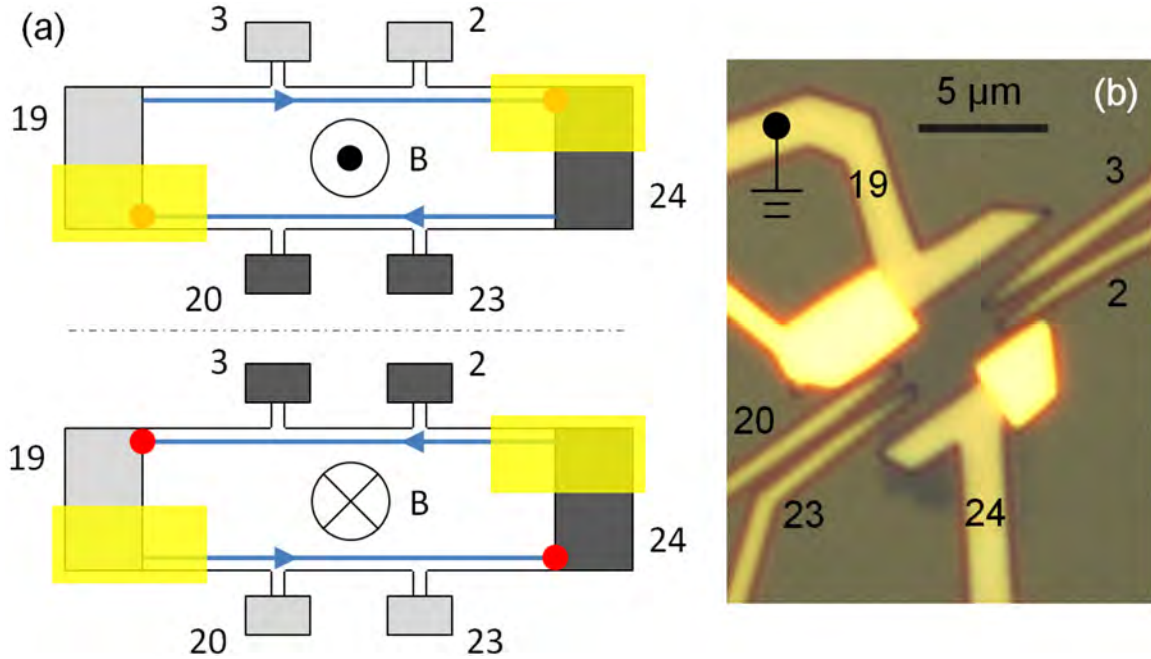


Figure 6.9: (a) Schematic illustration of the edge states and “hot spots” in a graphene Hall-bar in the quantum Hall regime (electrons as the charge carriers). The propagating directions of the edge states are indicated by the blue arrows and the locations of the dissipation corners (“hot spots”) are highlighted by the red dots. Equipotential contacts are grouped into the same color (light grey or dark grey) by assuming ideal source/drain electrodes (electrodes 19 and 24) with a vanishing contact resistance. The yellow rectangles stand for the deposited multilayer radiation-blocking structures. With a positive magnetic field (upper panel) the two hot spots are located underneath these relatively thick blocks, such that less Landau radiation may reach the photodetector compared to the situation where the magnetic field is reversed (lower panel). (b) Optical micrograph of a graphene emitter with assigned electrical leads. The bright-yellow (golden) radiation-blocking structures are comprised of (from bottom to top) 1-2 nm thick oxidized Al, ~20 nm thermally deposited SiO_x ($x \rightarrow 2$) and ~200 nm Ti/Au.

Due to space limitations, there is no additional well-known reference emitter in our sample holder. The working principle of a graphene emitter is schematically illustrated in Fig. 6.9(a). Fig. 6.9(b) shows an optical image with the assignment of the electrical leads. In Fig. 6.9(a), contacts with equipotentials in the quantum Hall regime (with electrons as the charge carriers) are drawn in the same color. The blue arrows indicate the propagation directions of the quantum Hall edge states. The “hot spots”, where energy dissipation takes place under quantum Hall conditions, are shown as red dots at the two diagonally opposing corners for current entry and exit. By changing the carrier type or reversing the

magnetic field the hot spots will occur at the two corners on the other diagonal. It is possible to block (part of) the Landau emission by depositing metals on top of the corners along one of the diagonals. Then for a certain magnetic field direction the Landau emission will be blocked (upper panel of Fig. 6.9(a)), such that a smaller portion of the radiation is collected by the photodetector compared to the situation where graphene radiates for the opposite direction of the magnetic field (lower panel of Fig. 6.9(a)). The response of the photodetector in the “blocked” case is recorded as the reference signal. Afterward, the magnetic field is reversed while its absolute magnitude remains the same. By carefully comparing the detector’s response in this “non-blocked” situation to the reference that is already recorded under the same input electric power, one may hopefully find evidence for inter-Landau-level radiative transitions in graphene.

6.3 Some preliminary measurements

Fig. 6.10 depicts some transport measurements for the graphene emitter in Fig. 6.9(b). These characterizations are carried out in a four-terminal configuration. The very low chemical-doping level (charge neutrality is close to 0 V), relatively high Drude mobility ($>7000 \text{ cm}^2/\text{Vs}$ at a carrier density of $4 \times 10^{12} \text{ cm}^{-2}$) and vanishing longitudinal resistance in the quantum Hall regime attest to the high quality of the sample.

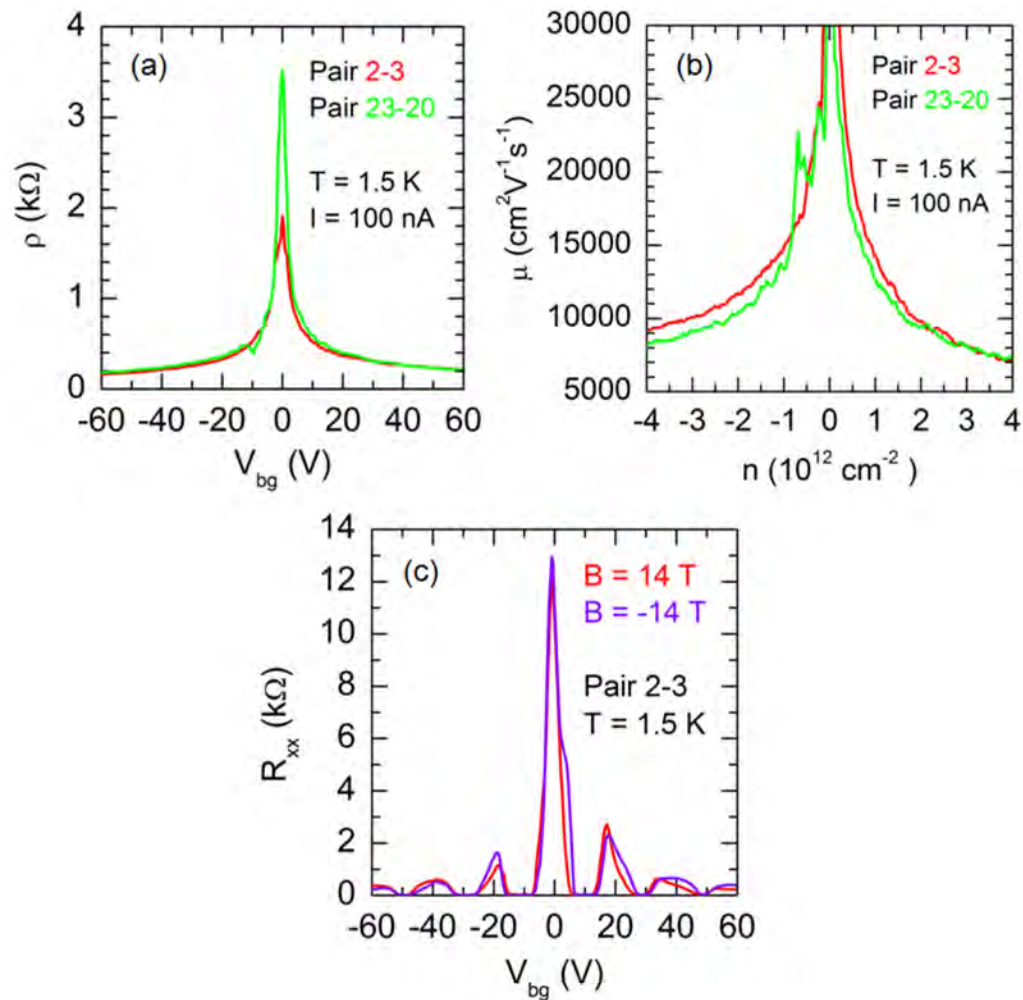


Figure 6.10: Low temperature electrical characterization for the graphene emitter in Fig. 6.9(b). (a) Electric field effect. (b) Drude mobility versus carrier density. (c) Longitudinal resistance as a function of the back gate voltage at $B = \pm 14 \text{ T}$.

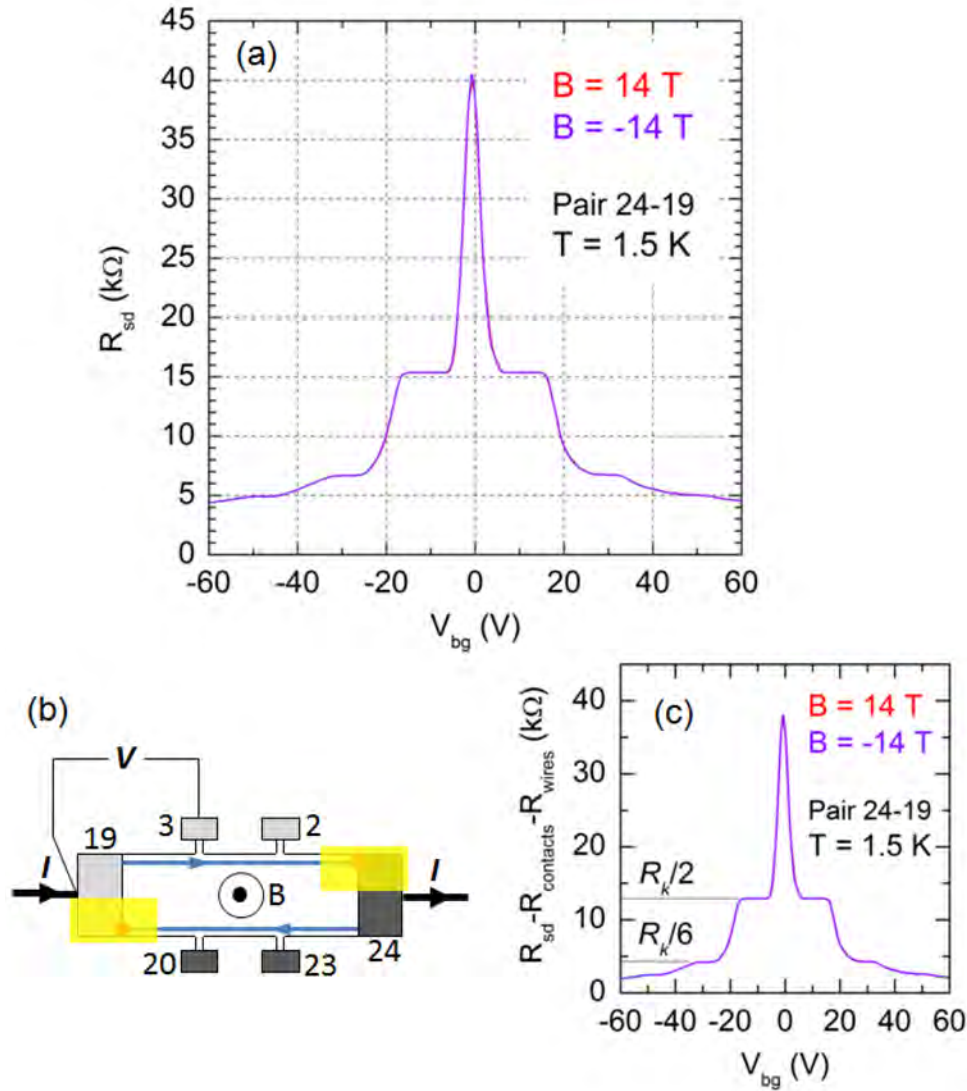


Figure 6.11: (a) Two-terminal source-drain resistance as a function of the back-gate voltage at $B = \pm 14$ T for the graphene emitter in Fig. 6.9(b). The resistance’s insensitiveness to the direction of the magnetic field ensures that the dissipated electric power in the emitter at fixed current bias is independent of the field direction. (b) Three-terminal configuration for the measurement of the source/drain contact resistance in the quantum Hall regime. The voltage difference V between contacts 19 and 3 (or, between 19 and 2) is a result of the contact resistance of current contact 19 with $R_{19} = V/I$, where I is the excitation current. (c) “Net” two-terminal resistance between the source and drain by subtracting the contact resistances ($R_{contacts}$) as well as the wire resistances (R_{wires}) from the original dataset in (a). Well developed resistance plateaux occur at $R_k/2$, $R_k/6$ and $R_k/10$ (not highlighted) with $R_k = h/e^2$.

Fig. 6.11(a) shows the two-terminal magneto-resistance as a function of the back-gate voltage at $B = \pm 14$ T for the same emitter. The plots are symmetric with respect to the

carrier type. The two-terminal resistances also remain essentially unchanged when reversing the magnetic field, suggesting that the dissipated power in the graphene emitter is insensitive to the direction of the magnetic field at a fixed current bias. This property is crucial to our detection scheme, where the graphene emitter itself provides a reference signal. The contact resistances of the source/drain electrodes of the graphene device in Fig. 6.9(b) are determined by using a three-terminal measurement setup as illustrated in Fig. 6.11(b). In the quantum Hall regime, the magneto-resistance measured between the current contact 19 and the potential probe 3 (or equivalently, between 19 and 2) gives the contact resistance of the source/drain electrode 19. Similarly, the contact resistance for the other current contact (contact 24) can be obtained by measuring the magneto-resistance between contacts 24 and 23 (or equivalently, between 24 and 20) under quantum Hall conditions. For the device in Fig. 6.9(b), the source/drain contact resistances are found to be very close to 1 k Ω at $B = \pm 14$ T with a weak dependence on the carrier density. By subtracting the contact and wire resistances from the original two-terminal resistances in Fig. 6.11(a), we obtain the plots for the “net” source-drain magneto-resistances as shown in Fig. 6.11(c). Resistance plateaux occur at $h/2e^2$, $h/6e^2$ and $h/10e^2$.

The work described above gives an introduction to our preliminary attempts in constructing a compact detection system for probing Landau emission from graphene. The extremely low emission power associated with the inter-Landau-level radiative transitions and the very high detector resistance call for additional experimental efforts. In particular, the detector working temperature, detector bias, electrical excitation frequency/amplitude, magnitude of the magnetic field, etc. are parameters that need

further optimization. In addition, a high-quality graphene emitter with a very large quantum Hall breakdown current may also be crucial.

References

- [1] B. Lax, *Quantum electronics* (Columbia University Press, 1960), pp. 428.
- [2] E. Gornik, *Recombination radiation from impact-ionized shallow donors in n-type InSb*, *Physical Review Letters* **29**, 595 (1972).
- [3] Y. Kawano, Y. Hisanaga, and S. Komiyama, *Cyclotron emission from quantized Hall devices: injection of nonequilibrium electrons from contacts*, *Physical Review B* **59**, 12537 (1999).
- [4] S. Komiyama and Y. Kawaguchi, *Heat instability of quantum Hall conductors*, *Physical Review B* **61**, 2014 (2000).
- [5] Y. Kawano and S. Komiyama, *Breakdown of the quantized Hall effect in the vicinity of current contacts*, *Physical Review B* **61**, 2931 (2000).
- [6] K. Hirakawa, K. Yamanaka, Y. Kawaguchi, M. Endo, M. Saeki, and S. Komiyama, *Far-infrared photoresponse of the magnetoresistance of the two-dimensional electron systems in the integer quantized Hall regime*, *Physical Review B* **63**, 085320 (2001).
- [7] Y. Kawano and S. Komiyama, *Spatial distribution of nonequilibrium electrons in quantum Hall devices: imaging via cyclotron emission*, *Physical Review B* **68**, 085328 (2003).
- [8] S. Komiyama, *Playing with quantum Hall effects and single-electron-tunneling effects*, *Superlattices and Microstructures* **33**, 405 (2003).
- [9] K. Ikushima, H. Sakuma, S. Komiyama, and K. Hirakawa, *Imaging of cyclotron emission from edge channels in quantum Hall conductors*, *Physical Review Letters* **93**, 146804 (2004).

- [10] S. Komiyama, H. Sakuma, K. Ikushima, and K. Hirakawa, *Electron temperature of hot spots in quantum Hall conductors*, Physical Review B **73**, 045333 (2006).
- [11] H. Sakuma, K. Ikushima, S. Komiyama, and K. Hirakawa, *Spectral measurement of weak THz waves with quantum Hall detectors*, Infrared Physics & Technology **48**, 235 (2006).
- [12] K. Ikushima, H. Sakuma, S. Komiyama, and K. Hirakawa, *Visualization of quantum Hall edge channels through imaging of terahertz emission*, Physical Review B **76**, 165323 (2007).
- [13] M. L. Sadowski, G. Martinez, M. Potemski, C. Berger, and W. A. de Heer, *Landau level spectroscopy of ultrathin graphite layers*, Physical Review Letters **97**, 266405 (2006).
- [14] V. P. Gusynin, S. G. Sharapov, and J. P. Carbotte, *Anomalous absorption line in the magneto-optical response of graphene*, Physical Review Letters **98**, 157402 (2007).
- [15] Z. Jiang, E. A. Henriksen, L. C. Tung, Y. J. Wang, M. E. Schwartz, M. Y. Han, P. Kim, and H. L. Stormer, *Infrared spectroscopy of Landau levels of graphene*, Physical Review Letters **98**, 197403 (2007).
- [16] T. Morimoto, Y. Hatsugai, and H. Aoki, *Cyclotron radiation and emission in graphene*, Physical Review B **78**, 073406 (2008).
- [17] M. Orlita, C. Faugeras, J. M. Schneider, G. Martinez, D. K. Maude, and M. Potemski, *Graphite from the viewpoint of Landau level spectroscopy: an effective graphene bilayer and monolayer*, Physical Review Letters **102**, 166401 (2009).
- [18] K. S. Novoselov, A. K. Geim, S. V. Morozov, D. Jiang, M. I. Katsnelson, I. V. Grigorieva, S. V. Dubonos, and A. A. Firsov, *Two-dimensional gas of massless Dirac fermions in graphene*, Nature **438**, 197-200 (2005).
- [19] Y. Zhang, Y. W. Tan, H. L. Stormer, and P. Kim, *Experimental observation of the quantum Hall effect and Berry's phase in graphene*, Nature **438**, 201-204 (2005).

- [20] C. W. J. Beenakker and H. van Houten, *Quantum transport in semiconductor nanostructures*, Solid State Physics **44**, 1-228 (1991).
- [21] A. K. Geim and K. S. Novoselov, *The rise of graphene*, Nature Materials **6**, 183-191 (2007).
- [22] E. A. Henriksen, *Cyclotron resonance in graphene*. PhD Thesis, (Columbia University, 2008).
- [23] E. L. Dereniak and G. D. Boreman, *Infrared detectors and systems* (John Wiley & Sons, Inc., 1996).

Summary

In this dissertation, we develop reliably working fabrication techniques for high-electronic-quality single- and dual-gated graphene devices. We investigate various electronic transport phenomena in graphene field-effect-transistors and bipolar junctions by means of multi-terminal measurements, and explore graphene's potential applications in the fields of quantum resistance metrology and Landau emitters.

The SiO₂ layer of an oxidized Si wafer that supports the exfoliated graphene flakes is important to make graphene visible to the human eye. Based on the optical contrast, it is possible to identify mono-, bi- and tri-layer graphitic films. We stress the connection between careful substrate-cleaning/lift-off and a high Drude mobility (e.g. >10000 cm²/Vs at a carrier density of 4×10¹² cm⁻² at room temperature) in a finished graphene field effect device. The carrier density in such a device is estimated by using a simple parallel-plate capacitor model, and the charge neutrality point of the device can be shifted close to 0 V by an *in situ* vacuum annealing. By estimating the carrier mean free path (which is found to be on the order of hundreds of nanometers) using the Einstein relation, we confirm that the electronic transport in our graphene devices is still in the diffusive regime. We find that a self-consistent Boltzmann formalism within the random phase approximation not only gives an adequate description to the zero-field diffusive transport in our high-quality devices at reasonably large carrier densities, but also justifies that the width of the peak corresponding to charge neutrality can be used to estimate the concentration of charged impurities. Our surface morphology investigations and the surface study reported by other research groups [1-6] suggest that organic residues,

ripples and wrinkles on the graphene sheet, dangling bonds on SiO₂ surface and trapped charges on (or near) the surface of SiO₂ may be the major sources of charged impurities.

The quantum Hall effect (QHE) in graphene is probed using a four-terminal configuration. The sequence of the integer QHE states is unconventional. Also, a quantum Hall state at filling factor $\nu = 0$ is observed in high-quality samples under very low excitation currents. The extraction of the back-gate capacitance from the Shubnikov-de Haas (SdH) oscillations is demonstrated. The result justifies the parallel-plate capacitor model. Owing to the large energy spacing (~ 149 meV in a magnetic field $B = 14$ T) between the zeroth and first Landau levels, a critical current as large as ~ 11 A/m associated with the breakdown of the $\nu = 2$ quantum Hall state is measured in our graphene sample at a temperature of 10 K and $B = 14$ T. This value of the breakdown current is several times higher than the typical ones in the conventional 2DES counterparts for the same magnetic field. The observed extraordinarily robust QHE at $\nu = 2$ shows that graphene is an excellent candidate material for the quantum resistance standard.

We devote one chapter to our preliminary attempts in designing and optimizing a compact system for the detection of the inter-Landau-level radiative transitions (i.e. Landau emission) in graphene devices. The emission power is estimated to be extremely low ($< 10^{-11}$ W), and the photodetector has to be operated in a highly resistive state due to the lack of background radiation. Various efforts in improving the sensibility of the detection system and reducing the noise level in the circuit are discussed. We introduce a method for the deposition of radiation-blocking structures on top of the two “hot spots” (i.e. energy dissipation corners in the quantum Hall regime) along one diagonal of the

graphene Hall-bar, such that the Landau radiation can be selectively blocked depending on the direction of the magnetic field. Then even for the same amount of dissipated power in the graphene emitter, the Landau radiation that reaches the photodetector differs. By this means, the graphene emitter itself provides a reference for the extraction of the radiation signal.

We carry out a systematic evaluation for various techniques used to prepare the top-gate dielectric for a dual-gated graphene device. Among them, metallic air bridges offer the option of a contactless top-gate at the cost of low yield. Low-temperature atomic layer deposition of Al_2O_3 provides precise control over the thickness of the dielectric layer, but also leads to difficulty in lift-off owing to the conformal coverage of the electron beam resist by deposited Al_2O_3 . We introduce a thin-film transfer technique, with which we are able to place ultra-thin insulating sheets precisely on top of graphene. Electrical characterizations on a graphene *p-n-p* device featuring an extremely thin (< 5 nm) transferred h-BN (hexagonal boron nitride) top-gate dielectric show that the top-gate possesses a very high coupling efficiency and a rather low leakage current ($\ll 1$ nA at a top-gate voltage of 2 V). This top-gating technique may be useful for the investigation of the quantum capacitance [7] and Coulomb drag between closely spaced graphene layers [8].

A hybrid top-gate dielectric comprised of naturally oxidized Al and thermally evaporated SiO_2 offers high-quality *p-n* junctions with high yield. In such a bipolar graphene device, electric fields applied by a global back-gate and a local top-gate enable independent control over the carrier type and density in two adjacent regions of the graphene sheet. It is possible to form *p-n* (or *n-p*), *p-p* and *n-n* junctions at the interface.

SUMMARY

Under quantum Hall conditions, the Hall and longitudinal resistances measured by multiple voltage contacts on the two sides of the junction show plateaux that agree quantitatively with the Landauer-Büttiker formula [9] and the mode mixing model [10]. Local potentials probed before and after mode mixing provide direct evidence for a complete equilibration of edge states at the p - n interface.

References

- [1] J. H. Chen, C. Jang, S. Xiao, M. Ishigami, and M. S. Fuhrer, *Intrinsic and extrinsic performance limits of graphene devices on SiO₂*, *Nature Nanotechnology* **3**, 206-209 (2008).
- [2] J. Martin, N. Akerman, G. Ulbricht, T. Lohmann, J. H. Smet, K. von Klitzing, and A. Yacoby, *Observation of electron-hole puddles in graphene using a scanning single-electron transistor*, *Nature Physics* **4**, 144 (2008).
- [3] Y. Zhang, V. W. Brar, C. Girit, A. Zettl, and M. F. Crommie, *Origin of spatial charge inhomogeneity in graphene*, *Nature Physics* **5**, 722-726 (2009).
- [4] C. R. Dean, A. F. Young, I. Meric, C. Lee, L. Wang, S. Sorgenfrei, K. Watanabe, T. Taniguchi, P. Kim, K. L. Shepard, and J. Hone, *Boron nitride substrates for high-quality graphene electronics*, *Nature Nanotechnology* **5**, 722-726 (2010).
- [5] J. Xue, J. Sanchez-Yamagishi, D. Bulmash, P. Jacquod, A. Deshpande, K. Watanabe, T. Taniguchi, P. Jarillo-Herrero, and B. J. LeRoy, *Scanning tunnelling microscopy and spectroscopy of ultra-flat graphene on hexagonal boron nitride*, *Nature Materials* **10**, 282-285 (2011).
- [6] R. G. Decker, Y. Wang, V. W. Brar, W. Regan, H.-Z. Tsai, Q. Wu, W. Gannett, A. Zettl, and M. F. Crommie, *Local electronic properties of graphene on a BN substrate via scanning tunneling microscopy*, *Nano Letters* 2291-2295 (2011).
- [7] J. Xia, F. Chen, J. Li, and N. Tao, *Measurement of the quantum capacitance of graphene*, *Nature Nanotechnology* **4**, 505 (2009).
- [8] H. Min, R. Bistritzer, J.-J. Su, and A. H. MacDonald, *Room-temperature superfluidity in graphene bilayers*, *Physical Review B* **78**, 121401 (2008).
- [9] M. Büttiker, *Absence of backscattering in the quantum Hall effect in multiprobe conductors*, *Physical Review B* **38**, 9375 (1988).

- [10] D. A. Abanin and L. S. Levitov, *Quantized transport in graphene p-n junctions in a magnetic field*, *Science* **317**, 641-643 (2007).

Curriculum Vitae

Name: **Shu XU**

Date of Birth: 02.09.1978

Country of Birth: China

Nationality: China

- **PhD Student** **12/2006 – 01/2012**
Max-Planck-Institute for Solid State Research, Stuttgart, Germany
Christian-Albrechts-Universität, Kiel, Germany
Advisors: Prof. Klaus von Klitzing, Prof. Franz Faupel
Dissertation: *Graphene Electronics: Device Fabrication and Electronic Transport*

- **M. Sc. in Materials Science** **10/2004 – 10/2006**
Christian-Albrechts-Universität, Kiel, Germany

- **Product Engineer** **07/2000 – 09/2004**
Intel Corporation, Shanghai, China / Folsom, U.S.A.

- **B. Sc. in Electrical Engineering** **09/1996 – 07/2000**
Fudan University, Shanghai, China